

## **Distribution Agreement**

In presenting this thesis or dissertation as a partial fulfillment of the requirements for an advanced degree from Emory University, I hereby grant to Emory University and its agents the non-exclusive license to archive, make accessible, and display my thesis or dissertation in whole or in part in all forms of media, now or hereafter known, including display on the world wide web. I understand that I may select some access restrictions as part of the online submission of this thesis or dissertation. I retain all ownership rights to the copyright of the thesis or dissertation. I also retain the right to use in future works (such as articles or books) all or part of this thesis or dissertation.

Signature:

---

Samuel Ban-Seok Jeong

---

Date

**The Dynamics and Kinetics of Proton Related Biological Processes**

By

Ban-Seok Jeong  
Doctor of Philosophy

Chemistry

---

R. Brian Dyer, Ph.D.

Advisor

---

James T. Kindt, Ph.D.

Committee Member

---

Khalid Salaita, Ph.D.

Committee Member

Accepted:

---

Lisa A. Tedesco, Ph.D.

Dean of the James T. Laney School of Graduate Studies

---

Date

The Dynamics and Kinetics of Proton Related Biological Processes

By

Samuel Ban-Seok Jeong

B.S., Korea University, 2002

M.S., Korea University, 2009

Advisor: R. Brian Dyer, Ph.D.

An abstract of

A dissertation submitted to the Faculty of the

James T. Laney School of Graduate Studies of Emory University

In partial fulfillment of the requirements for the degree of

Doctor of

Philosophy in

Chemistry

2018

# The Dynamics and Kinetics of Proton Related Biological Processes

By Ban-Seok Jeong

The proton plays special roles in biological systems because of its unique characteristics. Due to its minuscule size and exorbitantly high charge density, the proton is extremely reactive thermodynamically as well as kinetically. Because a proton can be transferred by the Grotthuss mechanism, its diffusion rate is fast. Since water molecules can easily accept or donate a proton, protons are readily available in an aqueous environment. Therefore, nature has employed protons for many biological processes and energy storage as a proton gradient is the central pillar of bioenergetics. The structure of proteins as well as the protein-protein interactions are modulated by protons. Most enzymes show highly pH-sensitive activity profiles. One good example is the viral infection cycle of influenza A virus. After endocytosis, the low pH within the lysosome activates the viral membrane protein, M2 proton channel. M2 conducts protons unidirectionally into the viral lumen with high selectivity and is activated at acidic pH, which has been of great interest for drug development. In this dissertation, using a laser-induced fast pH-jump, the fluorescence change of Trp41 of M2 transmembrane domain (M2TM) was measured. A double exponential decay was observed, where the fast phase was ascribed to protonation kinetics ( $\sim 2 \times 10^{10} \text{ M}^{-1}\text{s}^{-1}$ ), while the slow phase was attributed to the subsequent conformation change ( $\sim 4 \times 10^3 \text{ M}^{-1}\text{s}^{-1}$ ). The conformation change of M2 was further confirmed by FRET studies, demonstrating that M2TM makes a transition toward a more 'open' structure at acidic pH. The second half of this dissertation examined excited state intramolecular proton transfer dyes and their applications as hydrophilic, long-lived reversible photo-acids and local hydration level sensors. A previously reported hydrophobic long-lived reversible photo-acid was derivatized to be more hydrophilic by adding a sulfonate group. Although synthesis was successful, the sulfonation decreased the  $pK_a$  of naphthol, preventing intramolecular proton transfer and not allowing it to be long-lived. We also studied 2,7-DiazaTrp which was known to show distinct 500 nm fluorescence in the presence of water, making it a good local hydration sensor. The 2,7-DiazaTrp mutant of mastoparan X showed how it interacts with a membrane by probing local hydration level change.

# **The Dynamics and Kinetics of Proton Related Biological Processes**

By

Ban-Seok Jeong  
B.S., Korea University, 2002  
M.S., Korea University, 2009

Advisor: R. Brian Dyer, Ph.D.

A dissertation submitted to the Faculty of the  
James T. Laney School of Graduate Studies of Emory University  
In partial fulfillment of the requirements for the degree of  
Doctor of  
Philosophy in  
Chemistry  
2018

## Acknowledgement

I would like to thank Dr. Brian Dyer for his constant support and patience. I am fortunate to have such a great mentor. Whenever I bring him some crazy moonshot idea, he always encouraged me and guided me in the right direction with trust and patience. Without him, this dissertation would not have been possible. And, special thanks to Laura Dyer for her hospitality and her heart-warming food.

I would also like to thank Dr. James Kindt and Dr. Khalid Salaita for their guidance and valuable advice throughout the course of my Ph.D. research.

Special thanks to the members of the Dyer group, especially Brandon Green, Michael Reddish, Erin Schuler, Bryant Chica, and Louis Groff for helping me and sharing their knowledge and techniques.

Thank to Dr. David Lynn and Chen Liang for giving me the opportunity to collaborate.

I owe a large debt of gratitude to Noel Li for his help and friendship.

I would like to thank my mentees, Jonathan Zawadzki and Alexander Grayson, for trusting and assisting me.

I would also like to thank Steve Krebs for his kind help and support.

Many thanks to my wife, Anna Yeo-Jin Moon, for her unconditional love and sacrifice.

Finally, I would like to thank my parents, Manja Ju and Wonjoo Jeong, for their unlimited love and trust.

## Table of Contents

<b>Chapter 1: Introduction</b>	<b>1</b>
1.1 The Unique Characteristics of Proton	1
1.2 The Roles of Proton in Biochemical System	5
1.3 The pH jump technique as a Tool to Study Proton Related Processes	8
1.4 Influenza A M2 Proton Channel as a Model System	11
1.5 Excited-State Intramolecular Proton Transfer (ESIPT)	13
1.6 Dissertation Outline	15
1.7 Reference	17
<b>Chapter 2: Proton Transport Mechanism of M2 Proton Channel Studied by Laser Induced pH-jump</b>	<b>28</b>
2.1 Abstract	28
2.2 Introduction	29
2.3 Experimental Section	33
2.4 Results and Discussion	36
2.5 Conclusions	50
2.6 Appendix	51
2.7 References	61
<b>Chapter 3: pH Dependent Conformational Change of Influenza A M2 Proton Channel Revealed by FRET</b>	<b>67</b>
3.1 Abstract	67
3.2 Introduction	67
3.3 Experimental Section	73
3.4 Results	75
3.5 Discussion	79

3.6 Conclusions	84
3.7 Appendix	86
3.8 References	93
<b>Chapter 4: Synthesis and Characterization of Water-soluble Long-lived Reversible Photoacid and Its Application to pH-jump Experiment</b>	<b>100</b>
4.1 Abstract	100
4.2 Introduction	100
4.3 Experimental Section	104
4.4 Results and Discussions	106
4.5 Conclusions	109
4.6 Appendix	111
4.7 References	114
<b>Chapter 5: Investigation of Interaction between Mastoparan X and Membrane by Using 2,7-DiazaTrp as a Local Hydration Level Sensor</b>	<b>117</b>
5.1 Abstract	117
5.2 Introduction	117
5.3 Experimental Section	121
5.4 Results and Discussions	123
5.5 Conclusions	131
5.6 Appendix	133
5.7 References	135
<b>Chapter 6: Conclusion</b>	<b>140</b>
5.1 Summary	140
5.2 Perspective	141
5.3 References	146



## List of Figures

### Chapter 1

- Figure 1.1 The structure of (a) Eigen cation and (b) Zundel cation. 4

### Chapter 2

- Figure 2.1 pH dependence of the equilibrium structure of the M2TM tetramer 32
- Figure 2.2 M2TM dynamics triggered by a laser induced pH-jump. 41
- Figure 2.3 Electrostatic properties of the N-terminal region of M2TM tetramer (PDB ID 2L0J). 43
- Figure 2.4 Kinetic resolution of multi-step protonation of M2TM 47
- Figure 2.S1 Schematic of the pump-probe laser pH jump setup 51
- Figure 2.S2 The fluorescence titration curve of L-Trp-L-Lys (WK) dipeptide. 53
- Figure 2.S3 pH jump with fluorescence detection of WK dipeptide 54
- Figure 2.S4 Membrane adsorption thermodynamics of NPE-sulfate measured by ITC. 55
- Figure 2.S5 Amantadine titration to the 50  $\mu$ M M2TM in bicelle (DH(7)PC:DPPC=5:1, DPPC:peptide=100:1) at pH 6.5 with CD 56
- Figure 2.S6 Amantadine titration to the 10  $\mu$ M M2TM in bicelle (DH(7)PC:DPPC=5:1, DPPC:peptide=100:1) at pH 6.5 with Trp fluorescence 57
- Figure 2.S7 pH dependence of Trp fluorescence of the 10 $\mu$ M M2TM in bicelle (DH(7)PC:DPPC=5:1, DPPC:peptide=100:1) at various pH with/without 500 $\mu$ M Amantadine 58
- Figure 2.S8 Dependence of the rate constant  $k_2$  of M2TM as a function of  $\Delta[H^+]$  at 25  $^{\circ}$ C. 59

### Chapter 3

- Figure 3.1 Overlapped M2TM structures 68
- Figure 3.2 M2TM structure from PDB ID 3BKD 69
- Figure 3.3 Fluorescence spectra of FRET labeled M2TM (EDANS : DABCYL+ = 1 : 1) in DPPC bicelle in pH 6.5 buffer. 77

Figure 3.4	Fluorescence intensity change of (a) N-terminus labeled M2TM, (b) C-terminus labeled M2TM in DPPC bicelle as a function of pH.	78
Figure 3.5	FRET efficiency of M2TM (D/A=0.125) as a function of pH with/without amantadine	79
Figure 3.6	pH-dependent FRET efficiency of samples in various ratio between donor and acceptor.	83
Figure 3.7	Simulated FRET efficiency, and probability of formation of each tetramer of donor and acceptor combinations.	84
Figure 3.S1	ESI mass spectra of M2TM-EDAN	86
Figure 3.S2	ESI mass spectra of M2TM-DABCYL <sup>+</sup>	87
Figure 3.S3	Fluorescence spectra of EDANS and Absorbance spectra of DABCYL <sup>+</sup> in various pH buffer	88
Figure 3.S4	pH-dependent FRET efficiency in various ratios	91-92

## Chapter 4

Figure 4.1	Photo-cycle of naphthol based long-lived reversible photo-acid	103
Figure 4.2	Synthetic scheme of 6-hydroxy-5-(2-nitroethyl)naphthalene-2-sulfonate	106
Figure 4.3	UV-Vis spectrum of 6-hydroxy-5-(2-nitroethyl)naphthalene-2-sulfonate at pH 7.0.	107
Figure 4.4	UV-Vis spectra of 6-hydroxy-5-(2-nitroethyl)naphthalene-2-sulfonate at pH 7.0.	108
Figure 4.S1	<sup>1</sup> H and <sup>13</sup> C NMR spectra of sodium 6-hydroxy-5-(2-nitrovinyl)naphthalene-2-sulfonate.	111
Figure 4.S2	<sup>1</sup> H and <sup>13</sup> C NMR spectra of sodium 6-hydroxy-5-(2-nitroethyl)naphthalene-2-sulfonate.	112
Figure 4.S3	ESI mass spectrum of sodium 6-hydroxy-5-(2-nitroethyl)naphthalene-2-sulfonate.	113

## Chapter 5

Figure 5.1	ESIPT of 2,7-Diazaindole in the presence of water	120
Figure 5.2	Synthetic Scheme of Fmoc-L-(2,7-diaza)Trp	123
Figure 5.3	Enantioselective separation of 2,7-diazaTrp on the chiral column.	124
Figure 5.4	Absorbance (solid line) and Emission (dotted line) Spectrum of diAzaTrp in MeOH (red) or pH 7 phosphate buffer (black).	125
Figure 5.5	Fluorescence spectrum of DiazaTrp in (a) pH 7 buffer or (b)	126

	MeOH, and deconvoluted fluorescence spectra of N1, N2, and N7 position protonated species.	
Figure 5.6	pH-dependent intensity change of N1, N2, and N7 position protonated states	128
Figure 5.7	Fluorescence spectra of Trp3diazatrp mutant of Mastoparan X in pH 7 buffer (black) or in 1mM DPPC SUV solution with pH 7 buffer (red).	129
Figure 5.8	Fluorescence spectrum of Trp3diazatrp mutant of Mastoparan X in (a) pH 7 buffer or (b) 1mM DPPC SUV solution at pH 7, and deconvoluted fluorescence spectra of N1, N2, and N7 position protonated species.	130
Figure 5.S1	<sup>1</sup> H NMR spectrum of L-(2,7-diaza)Trp in D <sub>2</sub> O.	133
Figure 5.S2	<sup>1</sup> H NMR spectrum of Fmoc-L-(2,7-diaza)Trp in DMSO.	133
Figure 5.S3	MALDI mass spectrum of Trp3Diazatrp mutant of Mastoparan X peptide.	134

## List of Tables

### Chapter 1

Table 1.1	The Radii of Monovalent Cations and their Neutral Atoms.	1
-----------	--	---

### Chapter 3

Table 3.1	Comparison of M2 proton channel structure, experimental technique, condition, peptide length, mutation.	71
Table 3.2	Reported pK <sub>a</sub> values of M2 proton channel.	80
Table 3.S1	Possible FRET geometry among donor acceptor in tetrameric configuration	89
Table 3.S2	Probability of each possible combination and tis FRET efficiency	90

### Chapter 5

Table 5.1	Photophysical properties of deconvoluted fluorescence spectrum	127
-----------	--	-----

## Chapter 1: Introduction

### 1.1 The Unique Characteristics of Proton

The proton,  $H^+$ , has a unique niche in biological systems. The proton is the cation of hydrogen, which is the smallest element in the universe; its radius is 78 pm. Compared to the size of hydrogen, its bare nucleus, the proton has a size of  $0.8751 \text{ fm}^a$ , which is about  $8.9 \times 10^4$  times smaller than that of hydrogen atom. (table 1) Considering the fact that the size differences between other monovalent cations and their neutral atoms are about two times, the proton exhibits an extremely big difference. (table 1) This can be explained by the Rutherford-Bohr model of the atom, although this rudimentary model was later replaced by the quantum mechanical model, where positively charged small nucleus is surrounded by electrons orbiting around the nucleus. As observed from Rutherford's experiment, it is electrons which occupy most of the space of the atom, and the nucleus is tiny and heavy. For an example of hydrogen, the diameter of the nucleus is about 100,000 times smaller than that of the neutral atom. Except for period 1 elements such as hydrogen and helium, cations have at least one shell of electron cloud, which ensure their big size. On the other hand, hydrogen, a period 1 element cation, doesn't have an electron cloud at

Atomic Number	Name	Neutral Atom Radius (pm)	Cation Radius (pm)
1	Hydrogen	78	0.0008751
3	Lithium	152	78
11	Sodium	186	98
19	Potassium	227	133

**Table 1.1** The Radii of Monovalent Cations and their Neutral Atoms. (Data is from the reference 1, except the radius of proton, which is from 2014 CODATA)

<sup>a</sup> The size, or charge radius, of proton is from 2014 CODATA value. The methods employed to measure its size are electron-proton scattering experiment and spectroscopic method, which deduces a size of nucleus from the energy level of orbiting electron, and its accuracy is improved by introducing muonic hydrogen.

all, resulting in very small bare nucleus. Therefore, in biological systems, protons are the only entities in which the bare nuclei of atoms exist without an electron cloud.

Because of the miniscule size of proton, its charge density is exorbitantly high: the charge density<sup>b</sup> of a proton is approximately  $1.4 \times 10^{15}$  times higher than that of a sodium cation,<sup>c</sup> and this solely originates from the size difference since they both have the same single net positive charge. In the case of  $\text{Na}^+$ , positive charges of the nucleus penetrate the shielding effect of electron clouds, but in the proton, the positive charge of the nucleus is not shielded by any electron. Therefore, according to the hard-soft acid-base theory, the proton is classified as a hard acid because it has a high charge density, minimal polarizability, and acts as almost a point charge. High charge density of the proton drives its reaction equilibrium almost completely toward complex formation with other molecules; for example, the free energy of proton hydration reaction was calculated to be  $-1106.2 \text{ kJ}\cdot\text{mol}^{-1}$ .<sup>1,2,d</sup> Free proton is almost only observable in gaseous state in vacuum, and in most cases, proton rapidly reacts with other molecules.

Proton is not only thermodynamically reactive, but also kinetically reactive. The fast reaction of a proton with another molecule is first ensured by its large reaction cross section. Even though a proton has a size of  $8.751 \times 10^{-6} \text{ \AA}$ , it has 6-7  $\text{ \AA}$  of reaction radius.<sup>3</sup> Proton

---

<sup>b</sup> Charge density ( $\text{C}\cdot\text{mm}^{-3}$ ) =  $ne/(4/3)\pi r^3$ , where  $r$  is ionic radii,  $e$  is the electron charge, and  $n$  is the ionic charge number.

<sup>c</sup> The measurement of size of ion is typically calculated from their crystal structure, which is fundamentally different from the methods for proton size measurement. Therefore, direct comparison between the sizes of proton and sodium ion might be irrelevant. However, the tremendous size difference between proton and sodium ion still stays relevant.

<sup>d</sup> There are different values reported by other study. (Vlcek, L.; Chialvo, A. A., Single-ion hydration thermodynamics from clusters to bulk solutions: Recent insights from molecular modeling. *Fluid Phase Equilib.* **2016**, *407*, 58-75)

can be easily attracted to negatively charged residues by coulombic interaction. Second, there is no orientational requirement for reactions because a proton is spherical and small. Third, a proton is small enough to show wave-like behavior for a few Å (de Broglie  $\lambda = 1.49$  Å), where it can penetrate the potential barrier between a reactant and product. This quantum mechanical tunneling effect can expedite reaction kinetics. Third, the diffusion rate of a proton in aqueous solutions is much faster than for other cations; for instance,  $H^+$  diffuses 6-7 times faster than  $Na^+$ . The reaction of protonation is so fast that it is categorized in a diffusion-limited reaction, in which the rate limiting step is the diffusion process.

Such anomalously fast diffusion of protons in water was explained by the Grotthuss mechanism, which describe proton diffusion not by mass transportation, but proton “hopping” through the hydrogen bonding network of water molecules. In the modern view of the Grotthuss mechanism, a hydronium ion ( $H_3O^+$ ) exists either in the form of Eigen ( $H_3O^+(H_2O)_3$ ) or Zundel cation ( $H_5O_2^+$ ). (Figure 1) While Eigen suggested that a proton is localized in a single hydronium ( $H_3O^+$ ) molecule, and further solvated by three water molecules, Zundel proposed that a proton is shared by two water ( $H_2O$ ) molecules. Gutman proposed that a proton is transported by an E-Z-E mechanism, which begins from the initial state of an Eigen cation and transits to the Zundel as an intermediate, which subsequently ends up converting to an Eigen cation centered on a next water molecule.<sup>4</sup> It was shown by time-resolved infrared experiment that Eigen and Zundel complexes interconvert in 50 fs.<sup>5</sup> A 2D-IR study observed spectral signatures of Zundel cation at  $1760\text{ cm}^{-1}$  and  $3200\text{ cm}^{-1}$  which showed cross-peak and persists in the lifetime of 480 fs, implying stable Zundel complex and its importance in the proton transfer process.<sup>6</sup> In the Zundel cation, a proton is considered to be delocalized over two water molecules, penetrating small potential

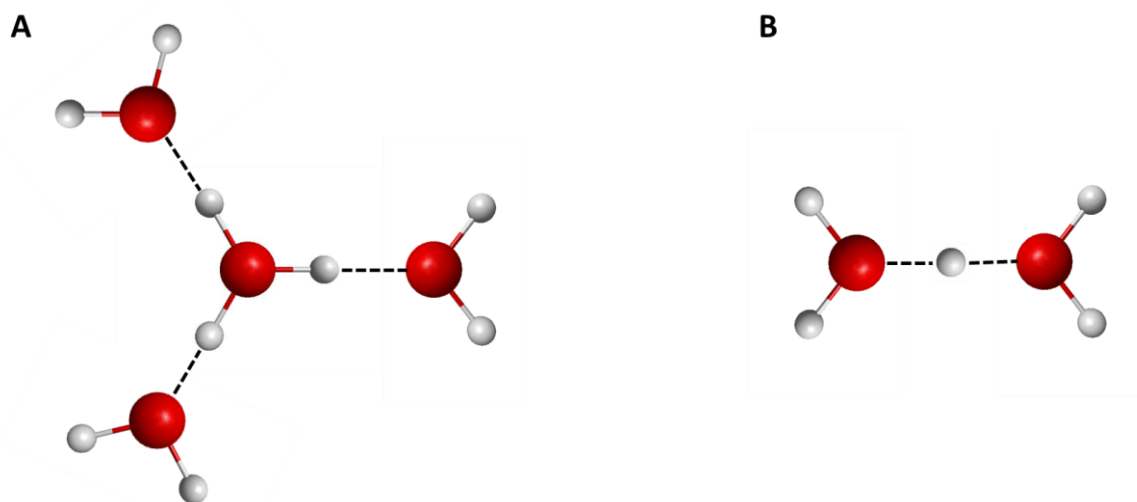


**Figure 1.1** The structure of (a) Eigen cation and (b) Zundel cation.

barrier between two water molecules. This shows the wave-like behavior of proton due to its small size, and it can be alternatively represented as a probability distribution along the axis between two water molecules according to Born's interpretation.

Water, a biological solvent, can be considered as a reservoir of protons. Water molecules ( $\text{H}_2\text{O}$ ) are dynamically interconverted to hydronium ions ( $\text{H}_3\text{O}^+$ ) or to hydroxide ions ( $\text{OH}^-$ ) by accepting or releasing a proton. Although this self-ionization of water is very slow ( $2.5 \times 10^{-5} \text{ s}^{-1}$ ), this reminds us that water can easily donate and accept protons to any basic or acid group, leaving hydroxide or hydronium ions behind. Therefore, for basic proton acceptors, protons are readily available in aqueous environments. Combined with the Grotthuss mechanism of rapid proton transportation, the availability of protons is further enhanced. Because of it, nature has taken full advantage of protons in biological systems.



## 1.2 The Roles of Proton in Biochemical System

Owing to these unique characteristics, protons play special roles in biochemical systems.<sup>3</sup> For energy metabolism, the proton gradient, proposed by Peter Mitchell<sup>7</sup> who won the Nobel Prize for this central concept of bioenergetics, powers cellular respiration to synthesize ATP so that all biochemical processes can proceed. During oxidative phosphorylation or photophosphorylation, the energy released by the oxidation of food or harvested from light is used to pump proton across the membrane by several membrane proteins such as NADH dehydrogenase, cytochrome C oxidase, and cytochrome b<sub>6</sub>f complex. The resulting proton motive force across a mitochondrial or thylakoidal membrane drives a membrane protein, ATP synthase, to produce ATP. While protons move through a proton channel in the F<sub>0</sub> subunit of ATP synthase, the  $\gamma$  subunit of ATP synthase rotates and results in an interaction between the  $\gamma$  and  $\beta$  subunits, catalyzing a bond formation between ADP and P<sub>i</sub> to generate ATP. The bacterial flagellar motor is also powered by a similar mechanism. On the other hand, the proton gradient can be uncoupled to release heat by non-shivering thermogenesis in mammalian and some plant cells. For example, thermogenin (or uncoupling protein 1) in the mitochondria of brown adipose cells increases proton permeability across the mitochondrial membrane, resulting in conversion of proton gradient energy to heat, although its proton conductance mechanism still remains controversial.<sup>8</sup>

Proton can also modulate quaternary structures of proteins. By protonation or deprotonation of ionizable protein residues, protein-protein interactions can become stronger or weaker. For instance, the influenza virus inner capsid is formed by a self-assembled layer of matrix 1 (M1) proteins. During a virus infection cycle, the viral lumen

is acidified, and below pH 6, the self-assembled layer of M1 is dissociated, allowing for viral genetic material to be released to the cytosol.<sup>9</sup> Another example is amyloid  $\beta$  ( $A\beta$ ) aggregation, which is highly implicated in Alzheimer's disease. Acidic pH is one of the factors inducing  $A\beta$  plaque formation in addition to metal ions, temperature, ionic strength, and membrane surfaces.<sup>10</sup>

Not only that, but protons can also influence secondary and tertiary structure of proteins, even dynamics by protonation or deprotonation of ionizable residues, leading to changes in electrostatic interactions, salt bridges, and/or hydrogen bonds.<sup>11-13</sup> For instance, hemoglobin changes its conformation to lower  $O_2$  affinity at acidic pH, caused from the high local concentration of  $CO_2$ , for effective release of  $O_2$ . In hemoglobin, protonation of His146 induces the formation of a salt bridge with Asp94, contributing to the conformation transition from R state to T state under acidic conditions. Poly-L-glutamic acid forms an  $\alpha$ -helix when carboxylic acid side chains are protonated at low pH because repulsion among negatively charged vicinal carboxylic acid residues are reduced by protonation.<sup>14-15</sup> The most dramatic examples of pH-driven protein conformational changes are in viral fusion proteins which exhibit a large conformational rearrangement under acidic conditions to fuse viral membranes with host membranes. This large conformational change could be induced not only by hydrogen bonding and salt bridge, but also by histidine-cation pairs and anion-anion pairs, which repel one another under acidic pH and neutral pH, respectively.<sup>16</sup> Moreover, it is reported that protein dynamics could be largely changed by pH shift even though its structural rearrangement is minimal.<sup>17-19</sup>

For enzymatic reactions, proton transfer steps comprise their essential parts. Acid/base catalysis is very common, and most enzymes have acidic or basic catalytic groups at their

active site. For instance, triosephosphate isomerase (TIM), dihydrofolate reductase (DHFR), and alcohol dehydrogenase (ADH) effectively conduct their protonation/deprotonation process to the specific position of the substrate by optimal positioning of acid/base sidechains at the active site. Moreover, the concentration of protons, or pH, can also have a significant impact on enzyme catalytic activity. Most enzymes are optimized to have the highest catalytic activity at a specific pH, which is usually the pH of their working environment. For example, most lysosomal enzymes exhibit highest catalytic activities at around pH 5 of the lysosome lumen, but have low or no activities at pH 7.2 of the cytosol, which can help to prevent cell damaging during accidental lysozyme leakage. Digestive enzymes have different pH optima depending on their local pH; pepsin in gastric juice at pH ~1.5 and chymotrypsin in the intestines at pH ~8. This pH dependency of enzyme activity could be partially explained by conformational changes of the enzyme in that the substrate or co-factor binding affinity could be altered. More importantly, pH change could have direct impacts on the protonation state of ionizable residues of the active site, H-bond network, substrate, co-factor, or binding site. Since multiple factors are correlated, pH-dependent catalytic activity often exhibits a sharp transition profile over a narrow pH range.

As it has been discussed, the transportation of protons and the interaction of protons with biomolecules have tremendous impacts on many biochemical processes. Therefore, a large body of research has focused on the kinetics and mechanism of these proton related processes in biochemical systems to better understand how protons are transported and how they trigger subsequent processes.

### 1.3 The pH jump technique as a Tool to Study Proton Related Processes

Because of such a fast protonation speed, it is difficult to study the kinetics and mechanism of protonation and the subsequent processes using rapid-mixers that are widely used to study chemical kinetics. The time resolution of a rapid mixer is typically limited to the millisecond regime mainly due to the initial dead time of the mixer.<sup>20-24</sup> While certain designs have helped to improve the time resolution to the sub-millisecond regime; the mixing technique is fundamentally restricted by diffusion. In order to study the mechanism and the kinetics of these fast pH dependent processes, faster triggering is required. In other words, in pH jump experiments, the initial triggering of pH change should be at least one order of magnitude faster than proton related processes which are often considered as diffusion controlled. To achieve this fast triggering, pH-jump experiments have been performed using flash photolysis of photo-acid.

Photo-acids release protons within a few nanoseconds after laser photolysis, making them ideal candidates for initiating pH jump experiments. Therefore, a laser induced pH-jump can be utilized as a sharp trigger to study kinetics faster than the millisecond time scale which rapid mixing cannot achieve. Several irreversible photo acids have been developed and their kinetics were characterized.<sup>25-30</sup> Among them, 2-nitrobenzaldehyde (NBA) and 1-(2-nitrophenyl)ethyl sulfate (NPE-sulfate) show desirable characteristics. NBA has a high deprotonation quantum yield of 0.5, fast deprotonation lifetime of ~10ns, but limited solubility in water.<sup>27, 30</sup> Compared to NBA, NPE-sulfate exhibits comparable quantum yield of 0.5, higher water solubility, lower membrane permeability, lower  $pK_a$  of byproduct, but slower deprotonation lifetime of ~100ns.<sup>28</sup>

By using these photo acids, laser pH-jump experiments have been developed by studying several model systems like proteins or peptides. With laser induced pH jump technique, the kinetics of histidine ligand dissociation from the heme of partially denatured cytochrome c was measured by transient absorption through the change in the Soret band, demonstrating that sub-millisecond time scale resolutions could be achieved.<sup>31</sup> pH dependent fluorescence and absorbance changes of GFP variants were also studied to investigate proton transfer rate to the chromophore.<sup>19,32</sup> Sub-microsecond time scale kinetics of alpha-helix formation of poly-L-glutamate were investigated by time-resolved infrared spectroscopy (TRIR).<sup>14-15</sup> The kinetics of acid-induced unfolding of myoglobin were observed by transient absorbance spectroscopy.<sup>33</sup> TRIR study of leucine zipper folding under acidic conditions have elucidated the folding kinetics and mechanism.<sup>34</sup>

In these studies, three probes were used: UV-Vis, infrared, and fluorescence. Among these probes, UV-Vis shows very high signal-to-noise ratio, and is restricted to samples having a chromophore such as heme or retinal. Therefore, candidates without such ligands cannot be studied under physiologically relevant conditions. On the other hand, infrared can be used as a universal label-free probe for proteins and peptides, although it requires a high concentration of sample, which means the pH jump has to be large enough to overcome the high buffering capacity of the sample. Fluorescence, however, only needs a low concentration of sample due to its high sensitivity. For instance, 1  $\mu\text{M}$  of GFP variants have been a subject of laser induced pH-jump experiment and sub-millisecond time scale kinetic studies.<sup>32</sup> However, it still requires either an intrinsic or non-intrinsic fluorophore in the sample. Only few proteins such as GFP and luciferin-luciferase system are highly fluorescent. Despite having a much lower quantum yield, an intrinsic fluorescence probe

like Trp could be also used. Apart from the fact that Trp is abundant in many proteins, Trp fluorescence is sensitive to its local environment, and it has been used intensively to study protein structure and conformation states.<sup>35</sup> Also, there are several unnatural amino-acids which can be a spectroscopic probe<sup>36-37</sup> and even have special functionality to sense surrounding microenvironment<sup>38-39</sup>. The probing method for pH-jump can be wisely selected based on the specific requirements of the protein of interest.

Despite pH jump being a very useful technique, it requires a user to overcome many technical difficulties. To obtain a high magnitude of pH jump, the pump pulse should be intense and focused, a high concentration of photo acid should be used, and sample concentration should be kept as low as possible. However, high power pump lasers can induce unwanted reactions such as heme deligation, and S-S bond breakage. Also, in many cases, intensely focused laser could damage the sample, and even the cuvette window. Furthermore, because of the poor solubility of NBA, it is hard to obtain photo acid concentrations high enough to induce a big pH jump. Also, at high concentrations, the photo-acid solution absorbs very heavily, aggravating the inner filter effect problem. In some cases, photo acid or byproduct interacts with the sample and may also perturb the structure. Since photolysis of irreversible photo acid require a fresh sample for every measurement, repetition of single shot experiments requires a large amount of sample.

Keeping these issues in mind, in this dissertation, pH-jump technique was developed and utility of the technique was demonstrated with Influenza A matrix 2 (AM2) proton channel.

## 1.4 Influenza A M2 Proton Channel as a Model System

Influenza A matrix 2 (AM2) proton channel is one of the most widely studied membrane channel proteins because it has been a promising target for anti-influenza drug development<sup>40</sup> and it's the smallest ion channel with high selectivity and pH-dependent conductance. Its structure has been thoroughly investigated by X-ray crystallography<sup>41-42</sup>, solution NMR<sup>43-46</sup>, solid-state NMR<sup>47-51</sup>, IR<sup>52-55</sup>, and EPR<sup>56-59</sup> spectroscopy. AM2 proton channel is homotetrameric and composed of three components: a N-terminal ectodomain (residue 1-24), a single transmembrane alpha helix domain (residue 25-46), and a C-terminal cytoplasmic tail (residue 47-97). Among them, the transmembrane domain (TM) is sufficient for most of its functions: channel formation, selective proton transportation, and drug binding (Figure 1).<sup>60-62</sup> In the TM domain, it is known that the H<sub>37</sub>XXXW<sub>41</sub> motif plays a crucial role on its function. Histidine is essential for high proton selectivity of at least 10<sup>6</sup> over other biological monovalent cations such as potassium and sodium ions. H37G and H37E mutants of M2 don't exhibit proton selectivity and pH dependent conductance.<sup>63-64</sup> It has been widely accepted that the Trp, enclosing the N-terminal exit of TM domain, acts as a gate and prevents the backward flow of protons. W41A, W41C, and W41F mutants of M2 lost its unidirectional conductance.<sup>65</sup> The highest resolution of AM2 structure is a 1.65 Å resolution crystal structure of AM2 TM domain in micelle at pH 6.5 (3LBW).<sup>41</sup> At the pore entrance, four Val<sub>27</sub> residues form the entry gate which is 2 Å wide, restricting the entry of water molecules into the pore. Since pore size is smaller than a water molecule, it is believed that water molecules would enter pore through backbone breathing.<sup>41, 47, 66-67</sup> Without the valine neck, proton conductance rate of V27A is 2-fold faster than that of WT.<sup>66</sup> Below the valine neck, water molecules are highly ordered and

form ice-like state because most of pore lining residues are hydrophobic. At His37 and Trp 41, the water network is blocked, not allowing proton conductance through the Grotthuss mechanism. At the cytoplasmic exit, Asp44 and Arg45 forms the exit cluster which facilitates proton transfer and stabilizes the indole side chain.<sup>68</sup>

During the influenza viral infection cycle, influenza virus particles are bound to the mucous membrane by interactions among hemagglutinin and sialic acid on the cell surface. In turn, the viral particles enter the cell by endocytosis. While the endosome matures to a lysosome, pH becomes acidic by V-type ATPase. Acidic pH triggers two membrane proteins of influenza; a) hemagglutinin fuses the viral membrane with the host lysosomal membrane to release cargo from the virus lumen. b) M2 proton channel is activated by acidic pH and subsequently conducts protons into the viral lumen to disassemble the M1 protein inner capsid. Finally, ribonucleoprotein (RNP) complex is liberated into host cytosol.

The mechanism of proton transport and pH dependent gating of M2 proton channel has been investigated. From three structures at pH 5, 6.5, and 7.5-8 (figure 2), it was suggested that pH dependent conformational change occurs due to protonation of histidine.<sup>41</sup> From an NMR study, the  $pK_a$  values for histidine tetrad of M2 proton channel were estimated to be 8.0, 8.0, 6.3, <5.0<sup>69</sup>, although there is a significant amount of debate surrounding the numbers: Hong and co-workers recently reported different set of  $pK_a$  values of 7.6, 6.8, 4.9, and 4.2<sup>70</sup>, and Chou and colleagues obtained doubly degenerated  $pK_a$  values of 4.52, and 7.63<sup>70</sup>. In general, it is believed that at physiological condition, two histidines are protonated and two positively charged residues in low dielectric environment are stabilized by hydrogen bonding with water molecules. As the pH is lowered, the 3rd histidine of M2 proton channel is protonated, resulting in repulsion among positive charges, which



subsequently induces dilatation of C-terminal ends (Figure 2).<sup>42, 48, 57, 71</sup> In this activated form, the indole side chains of Trp tetramer near C-terminal ends, which was initially tightly packed at high pH, is now loosened and made more accessible to water molecules.<sup>72-73</sup> Moreover, in NMR studies, peak broadening was observed at low pH indicating more dynamic structure of the activated form.<sup>46</sup> Now, it is generally accepted that His<sub>37</sub> is repeatedly protonated and deprotonated altering between 2+ and 3+ states during proton transportation. This proton shuttle mechanism can be supported by slow proton conduction rate of M2 (100~1000 H<sup>+</sup>/s), and high deuterium isotope effect.<sup>71, 74-76</sup> Also, the shuttle mechanism can explain leveling off of conductance rate at below pH 6.<sup>66, 77</sup> Furthermore, computational simulation studies are in agreement with this mechanism.<sup>78-80</sup>

However, these mechanisms are inferred from steady state measurements with very limited kinetic evidence under a physiologically relevant proton gradient. Therefore, many details of proposed mechanisms are unclear, and with controversies looming large about the role of histidine, Val neck, and protein backbone.<sup>80</sup> In this dissertation, a rapid laser induced pH jump technique was used to observe Trp fluorescence decay after a rapid pH drop in order to elucidate the kinetics and the mechanism of M2 proton channel activation. Moreover, the conformational rearrangement of M2 proton channel is further verified by Förster resonance energy transfer (FRET) experiment.

### **1.5 Excited-State Intramolecular Proton Transfer (ESIPT)**

Proton transfer can be triggered by electronic excitation, called excited-state proton transfer (ESPT). Typically, an aromatic compound with ionizable residue such as hydroxyl group

can undergo ESPT. In most cases, intramolecular charge transfer (ICT) drives  $pK_a$  shift of the ionizable residue; excited state electron density nearby the ionizable residue is smaller than ground state electron density, thus, a proton is released, and the resulting anion state can be stabilized. In the case of pyranine (8-hydroxypyrene-1,3,6-trisulfonic acid, HPTS), the  $pK_a$  decreases from 7.4 in the ground state to 0.4 in the excited state.<sup>81</sup> This large  $pK_a$  shift induces rapid proton transportation in picoseconds time scale. This rapid ESPT process has been utilized for several experimental tools. When its proton is transported to another ionizable residue in the same molecule, it is called excited-state intramolecular proton transfer (ESIPT).

First, reversible photo-acids have taken advantage of fast proton release from ESPT. After excitation, the photo-acid, such as naphthol derivatives or pyranine, releases a proton to nearby water molecule in hydrogen bond with its hydroxyl group, triggering proton transfer process. After relaxation of excited state back to the ground state, the released proton is recombined. This reversible photo-acid was used to measure the kinetics of proton transfer process under various conditions and environments.<sup>3</sup>

Second, ESIPT dye has been used to probe microenvironment around the dye. While photo-acid transfer its proton to a water molecule, ESIPT dye transports its proton not only to a water, but also to another ionizable residue in the same molecule. When ESIPT dye is excited, there are two species; normal excited state ( $N^*$ ) and ESIPT phototautomer ( $T^*$ ) product, resulting in dual emission. Such dual emission is highly sensitive to its microenvironment because a decrease of polarity and hydrogen bond donor ability of microenvironment can preferentially inhibit ESIPT process, which suppresses  $T^*$  species generation. From ratio between  $N^*$  and  $T^*$  species, one can probe a polarity and hydration

level of the microenvironment. Owing to these unique characteristics of ESIPT dye, protein-protein, protein-DNA, and protein-membrane interactions were studied with ESIPT dyes as a sensor.

Both approaches were used in the research presented in this dissertation: a) water-soluble long-lived reversible photo-acid was designed and synthesized to improve the pH-jump technique, and b) 2,7-DiazaTryptophan was introduced to peptides as local environment sensor.

## **1.6 Dissertation outline**

**Specific Aim 1: to study proton transportation and channel activation mechanism of m2 proton channel by laser pH-jump.**

Hypothesis: The influenza A M2 proton channel is activated by its conformational change, C-terminal dilation, after His37 tetrad protonation.

Laser-induced pH-jump technique was adapted to study activation and proton transportation mechanism of M2TM. pH-dependence Trp41 fluorescence change of M2TM is attributed to both His37 protonation and channel hydration. After rapid acidification in 10 ns, double exponential decay of Trp fluorescence was observed: fast phase was ascribed to His37 protonation, and slow phase was attributed to subsequent conformation change increasing channel hydration level. (Chapter 2) In order to directly observe channel conformation change, FRET pair was labeled either N- or C-terminus end of M2TM. FRET experiments indeed demonstrated channel opening at acidic pH. (Chapter

3)

**Specific Aim 2: to improve laser pH-jump technique by synthesizing new generation photo-acid.**

Hypothesis: By adding sulfonate functional group to the long-lived reversible photoacid, 1-(2-Nitro-ethyl)-naphthalen-2-ol, solubility can be improved while all other properties are conserved.

In order to improve laser pH-jump experiment, the long-lived reversible photo-acids have been synthesized. Among them, 1-(2-Nitro-ethyl)-naphthalen-2-ol showed desirable characteristics for excellent candidate for kinetics measurement but extremely low water solubility impeded its application. To overcome this disadvantage, hydrophilic long-lived reversible photo-acid was designed to add a sulfonate group to 6-position of 2-naphthol ring. While synthesis was successful,  $\Delta pK_a$  between naphthol and  $\alpha$ -carbon of nitro-group became negligible, thus, no driving force for intramolecular proton transfer which stabilizes its anion state. (Chapter 4)

**Specific Aim 3: to investigate local hydration level change of mastoparan X during membrane insertion.**

Hypothesis: 2,7-diazaTrp substitution of Trp3 of mastoparan X may be sensitive to its folding, interaction with membrane, and eventually pore formation processes.

Mastoparan X (MX) is one of antimicrobial peptides (AMP), which binds to the negatively

charged surface of bacterial membrane and disrupts it. There have been many studies, but the mechanism of membrane disruption by AMPs is not yet clearly elucidated. 2,7-DiazaTryptophan is an unnatural amino acid, which undergoes ESIPT from N1 proton to N7 position only when aprotic solvent catalyzes it. N7 protonated species shows unique emission centered at 500 nm. By incorporating 2,7-diazaTrp to protein, local hydration level can be probed. 2,7-diazaTrp mutant of MX is used to study its interaction with membrane and specific membrane disruption mechanism. (Chapter 5)

## 1.7 Reference

1. Emsley, J., *The elements*. 3rd ed.; Clarendon Press, Oxford University Press: Oxford New York, 1998.
2. Pollard, T. P.; Beck, T. L., The thermodynamics of proton hydration and the electrochemical surface potential of water. *J. Chem. Phys.* **2014**, *141* (18).
3. Gutman, M.; Nachliel, E., The Dynamic Aspects of Proton-Transfer Processes. *Biochim. Biophys. Acta* **1990**, *1015* (3), 391-414.
4. Agmon, N.; Bakker, H. J.; Campen, R. K.; Henchman, R. H.; Pohl, P.; Roke, S.; Thamer, M.; Hassanali, A., Protons and Hydroxide Ions in Aqueous Systems. *Chem. Rev.* **2016**, *116* (13), 7642-72.
5. Woutersen, S.; Bakker, H. J., Ultrafast vibrational and structural dynamics of the proton in liquid water. *Phys. Rev. Lett.* **2006**, *96* (13), 138305.
6. Thamer, M.; De Marco, L.; Ramasesha, K.; Mandal, A.; Tokmakoff, A., Ultrafast 2D IR spectroscopy of the excess proton in liquid water. *Science* **2015**, *350* (6256), 78-82.

7. Mitchell, P., Coupling of Phosphorylation to Electron and Hydrogen Transfer by a Chemi-Osmotic Type of Mechanism. *Nature* **1961**, *191* (478), 144-&.
8. Crichton, P. G.; Lee, Y.; Kunji, E. R. S., The molecular features of uncoupling protein 1 support a conventional mitochondrial carrier-like mechanism. *Biochimie* **2017**, *134*, 35-50.
9. Shtykova, E. V.; Dadinova, L. A.; Fedorova, N. V.; Golanikov, A. E.; Bogacheva, E. N.; Ksenofontov, A. L.; Baratova, L. A.; Shilova, L. A.; Tashkin, V. Y.; Galimzyanov, T. R.; Jeffries, C. M.; Svergun, D. I.; Batishchev, O. V., Influenza virus Matrix Protein M1 preserves its conformation with pH, changing multimerization state at the priming stage due to electrostatics. *Sci Rep* **2017**, *7* (1), 16793.
10. Snyder, S. W.; Ladrer, U. S.; Wade, W. S.; Wang, G. T.; Barrett, L. W.; Matayoshi, E. D.; Huffaker, H. J.; Krafft, G. A.; Holzman, T. F., Amyloid-beta aggregation: selective inhibition of aggregation in mixtures of amyloid with different chain lengths. *Biophys. J.* **1994**, *67* (3), 1216-28.
11. Chimenti, M. S.; Khangulov, V. S.; Robinson, A. C.; Heroux, A.; Majumdar, A.; Schlessman, J. L.; Garcia-Moreno, B., Structural Reorganization Triggered by Charging of Lys Residues in the Hydrophobic Interior of a Protein. *Structure* **2012**, *20* (6), 1071-1085.
12. Anderson, D. E.; Becktel, W. J.; Dahlquist, F. W., Ph-Induced Denaturation of Proteins - a Single Salt Bridge Contributes 3-5 Kcal Mol to the Free-Energy of Folding of T4-Lysozyme. *Biochemistry* **1990**, *29* (9), 2403-2408.
13. Yang, A. S.; Honig, B., On the Ph-Dependence of Protein Stability. *J. Mol. Biol.* **1993**, *231* (2), 459-474.
14. Causgrove, T. P.; Dyer, R. B., Nonequilibrium protein folding dynamics: laser-

induced pH-jump studies of the-helix-coil transition. *Chem. Phys.* **2006**, *323* (1), 2-10.

15. Donten, M. L.; Hamm, P., pH-jump induced alpha-helix folding of poly-L-glutamic acid. *Chem. Phys.* **2013**, *422*, 124-130.

16. Harrison, J. S.; Higgins, C. D.; O'Meara, M. J.; Koellhoffer, J. F.; Kuhlman, B. A.; Lai, J. R., Role of Electrostatic Repulsion in Controlling pH-Dependent Conformational Changes of Viral Fusion Proteins. *Structure* **2013**, *21* (7), 1085-1096.

17. Haupts, U.; Maiti, S.; Schwille, P.; Webb, W. W., Dynamics of fluorescence fluctuations in green fluorescent protein observed by fluorescence correlation spectroscopy. *Proc. Natl. Acad. Sci. USA* **1998**, *95* (23), 13573-13578.

18. Kim, H. W.; Rhee, Y. M., On the pH Dependent Behavior of the Firefly Bioluminescence: Protein Dynamics and Water Content in the Active Pocket. *J. Phys. Chem. B* **2013**, *117* (24), 7260-7269.

19. Saxena, A. M.; Udgaonkar, J. B.; Krishnamoorthy, G., Protein dynamics control proton transfer from bulk solvent to protein interior: A case study with a green fluorescent protein. *Protein Sci.* **2005**, *14* (7), 1787-1799.

20. Hiromi, K.; Ohnishi, M.; Kanaya, K. I.; Matsumoto, T., Ph Jump Study of Enzyme Proteins .1. Liquefying Alpha-Amylase from Bacillus-Subtilis. *J. Biochem.* **1975**, *77* (5), 957-963.

21. Kitagishi, K.; Hiromi, K., Ph-Jump of Pepsin Studied by Tyrosine Ionization. *Agricultural and Biological Chemistry* **1986**, *50* (5), 1113-1116.

22. Kuwajima, K.; Matsushima, T.; Nitta, K.; Sugai, S., Ph-Jump Titration of the Tyrosyl Groups of Bovine Plasma-Albumin. *Biopolymers* **1984**, *23* (7), 1347-1365.

23. Oleary, M. H.; Brummund, W., Ph Jump Studies of Glutamate Decarboxylase -

Evidence for a Ph-Dependent Conformation Change. *J. Biol. Chem.* **1974**, *249* (12), 3737-3745.

24. Sato, S.; Luisi, D. L.; Raleigh, D. P., pH jump studies of the folding of the multidomain ribosomal protein L9: The structural organization of the N-terminal domain does not affect the anomalously slow folding of the C-terminal domain. *Biochemistry* **2000**, *39* (16), 4955-4962.

25. Geissler, D.; Antonenko, Y. N.; Schmidt, R.; Keller, S.; Krylova, O. O.; Wiesner, B.; Bendig, J.; Pohl, P.; Hagen, V., (Coumarin-4-yl)methyl esters as highly efficient, ultrafast phototriggers for protons and their application to acidifying membrane surfaces. *Angew Chem Int Edit* **2005**, *44* (8), 1195-1198.

26. Janko, K.; Reichert, J., Proton Concentration Jumps and Generation of Transmembrane Ph-Gradients by Photolysis of 4-Formyl-6-Methoxy-3-Nitrophenoxyacetic Acid. *Biochim. Biophys. Acta* **1987**, *905* (2), 409-416.

27. Abbruzzetti, S.; Carcelli, M.; Rogolino, D.; Viappiani, C., Deprotonation yields, pK(a), and aci-nitro decay rates in some substituted o-nitrobenzaldehydes. *Photochem. Photobiol. Sci.* **2003**, *2* (7), 796-800.

28. Abbruzzetti, S.; Sottini, S.; Viappiani, C.; Corrie, J. E. T., Kinetics of proton release after flash photolysis of 1-(2-nitrophenyl)ethyl sulfate (caged sulfate) in aqueous solution. *J. Am. Chem. Soc.* **2005**, *127* (27), 9865-9874.

29. Barth, A.; Corrie, J. E. T., Characterization of a new caged proton capable of inducing large pH jumps. *Biophys. J.* **2002**, *83* (5), 2864-2871.

30. Donten, M. L.; Hamm, P., pH-Jump Overshooting. *J. Phys. Chem. Lett.* **2011**, *2* (13), 1607-1611.



31. Abbruzzetti, S.; Viappiani, C.; Small, J. R.; Libertini, L. J.; Small, E. W., Kinetics of histidine deligation from the heme in GuHCl-unfolded Fe(III) cytochrome c studied by a laser-induced pH-jump technique. *J. Am. Chem. Soc.* **2001**, *123* (27), 6649-6653.
32. Abbruzzetti, S.; Grandi, E.; Viappiani, C.; Bologna, S.; Campanini, B.; Raboni, S.; Bettati, S.; Mozzarelli, A., Kinetics of acid-induced spectral changes in the GFPmut2 chromophore. *J. Am. Chem. Soc.* **2005**, *127* (2), 626-635.
33. Abbruzzetti, S.; Sottini, S.; Viappiani, C.; Corrie, J. E. T., Acid-induced unfolding of myoglobin triggered by a laser pH jump method. *Photochem. Photobiol. Sci.* **2006**, *5* (6), 621-628.
34. Hamm, P., pH-Jump Induced Leucine Zipper Folding Beyond the Diffusion Limit. *J. Phys. Chem. B* **2014**.
35. Chen, Y.; Barkley, M. D., Toward understanding tryptophan fluorescence in proteins. *Biochemistry* **1998**, *37* (28), 9976-82.
36. Sinkeldam, R. W.; Greco, N. J.; Tor, Y., Fluorescent Analogs of Biomolecular Building Blocks: Design, Properties, and Applications. *Chem. Rev.* **2010**, *110* (5), 2579-2619.
37. Wang, L.; Xie, J.; Schultz, P. G., Expanding the genetic code. *Annu. Rev. Biophys. Biomol. Struct.* **2006**, *35*, 225-249.
38. Shen, J. Y.; Chao, W. C.; Liu, C.; Pan, H. A.; Yang, H. C.; Chen, C. L.; Lan, Y. K.; Lin, L. J.; Wang, J. S.; Lu, J. F.; Chou, S. C. W.; Tang, K. C.; Chou, P. T., Probing water micro-solvation in proteins by water catalysed proton-transfer tautomerism. *Nat Commun* **2013**, *4*.
39. Niu, W.; Guo, J. T., Expanding the chemistry of fluorescent protein biosensors

through genetic incorporation of unnatural amino acids. *Mol Biosyst* **2013**, *9* (12), 2961-2970.

40. Moorthy, N. S. H. N.; Poongavanam, V.; Pratheepa, V., Viral M2 Ion Channel Protein: A Promising Target for Anti-influenza Drug Discovery. *Mini-Reviews in Medicinal Chemistry* **2014**, *14* (10), 819-830.

41. Acharya, R.; Carnevale, V.; Fiorin, G.; Levine, B. G.; Polishchuk, A. L.; Balannik, V.; Samish, I.; Lamb, R. A.; Pinto, L. H.; DeGrado, W. F.; Klein, M. L., Structure and mechanism of proton transport through the transmembrane tetrameric M2 protein bundle of the influenza A virus. *Proc. Natl. Acad. Sci. USA* **2010**, *107* (34), 15075-15080.

42. Stouffer, A. L.; Acharya, R.; Salom, D.; Levine, A. S.; Di Costanzo, L.; Soto, C. S.; Tereshko, V.; Nanda, V.; Stayrook, S.; DeGrado, W. F., Structural basis for the function and inhibition of an influenza virus proton channel. *Nature* **2008**, *451* (7178), 596-U13.

43. Wang, J.; Wu, Y. B.; Ma, C. L.; Fiorin, G.; Wang, J. Z.; Pinto, L. H.; Lamb, R. A.; Klein, M. L.; DeGrado, W. F., Structure and inhibition of the drug-resistant S31N mutant of the M2 ion channel of influenza A virus. *Proc. Natl. Acad. Sci. USA* **2013**, *110* (4), 1315-1320.

44. Pielak, R. M.; Chou, J. J., Solution NMR structure of the V27A drug resistant mutant of influenza A M2 channel. *Biochem. Biophys. Res. Commun.* **2010**, *401* (1), 58-63.

45. Pielak, R. M.; Schnell, J. R.; Chou, J. J., Mechanism of drug inhibition and drug resistance of influenza A M2 channel. *Proc. Natl. Acad. Sci. USA* **2009**, *106* (18), 7379-7384.

46. Schnell, J. R.; Chou, J. J., Structure and mechanism of the M2 proton channel of influenza A virus. *Nature* **2008**, *451* (7178), 591-U12.

47. Sharma, M.; Yi, M. G.; Dong, H.; Qin, H. J.; Peterson, E.; Busath, D. D.; Zhou, H. X.; Cross, T. A., Insight into the Mechanism of the Influenza A Proton Channel from a Structure in a Lipid Bilayer. *Science* **2010**, *330* (6003), 509-512.
48. Cady, S. D.; Schmidt-Rohr, K.; Wang, J.; Soto, C. S.; DeGrado, W. F.; Hong, M., Structure of the amantadine binding site of influenza M2 proton channels in lipid bilayers. *Nature* **2010**, *463* (7281), 689-U127.
49. Cady, S. D.; Mishanina, T. V.; Hong, M., Structure of Amantadine-Bound M2 Transmembrane Peptide of Influenza A in Lipid Bilayers from Magic-Angle-Spinning Solid-State NMR: The Role of Ser31 in Amantadine Binding. *J. Mol. Biol.* **2009**, *385* (4), 1127-1141.
50. Hu, J.; Asbury, T.; Achuthan, S.; Li, C. G.; Bertram, R.; Quine, J. R.; Fu, R. Q.; Cross, T. A., Backbone structure of the amantadine-blocked trans-membrane domain M2 proton channel from influenza A virus. *Biophys. J.* **2007**, *92* (12), 4335-4343.
51. Nishimura, K.; Kim, S. G.; Zhang, L.; Cross, T. A., The closed state of a H<sup>+</sup> channel helical bundle combining precise orientational and distance restraints from solid state NMR-1. *Biochemistry* **2002**, *41* (44), 13170-13177.
52. Ghosh, A.; Wang, J.; Moroz, Y. S.; Korendovych, I. V.; Zanni, M.; DeGrado, W. F.; Gai, F.; Hochstrasser, R. M., 2D IR spectroscopy reveals the role of water in the binding of channel-blocking drugs to the influenza M2 channel. *J. Chem. Phys.* **2014**, *140* (23).
53. Ghosh, A.; Qiu, J.; DeGrado, W. F.; Hochstrasser, R. M., Tidal surge in the M2 proton channel, sensed by 2D IR spectroscopy. *Proc. Natl. Acad. Sci. USA* **2011**, *108* (15), 6115-6120.
54. Manor, J.; Mukherjee, P.; Lin, Y. S.; Leonov, H.; Skinner, J. L.; Zanni, M. T.; Arkin,

- I. T., Gating Mechanism of the Influenza A M2 Channel Revealed by 1D and 2D IR Spectroscopies. *Structure* **2009**, *17* (2), 247-254.
55. Kukol, A.; Adams, P. D.; Rice, L. M.; Brunger, A. T.; Arkin, I. T., Experimentally based orientational refinement of membrane protein models: A structure for the Influenza A M2 H<sup>+</sup> channel. *J. Mol. Biol.* **1999**, *286* (3), 951-962.
56. Huang, S.; Green, B.; Thompson, M.; Chen, R.; Thomaston, J.; DeGrado, W. F.; Howard, K. P., C-terminal juxtamembrane region of full-length M2 protein forms a membrane surface associated amphipathic helix. *Protein Sci.* **2014**.
57. Thomaston, J. L.; Nguyen, P. A.; Brown, E. C.; Upshur, M. A.; Wang, J.; DeGrado, W. F.; Howard, K. P., Detection of drug-induced conformational change of a transmembrane protein in lipid bilayers using site-directed spin labeling. *Protein Sci.* **2013**, *22* (1), 65-73.
58. Nguyen, P. A.; Soto, C. S.; Polishchuk, A.; Caputo, G. A.; Tatko, C. D.; Ma, C. L.; Ohigashi, Y.; Pinto, L. H.; DeGrado, W. F.; Howard, K. P., pH-induced conformational change of the influenza M2 protein C-terminal domain. *Biochemistry* **2008**, *47* (38), 9934-9936.
59. Duong-Ly, K. C.; Nanda, V.; Degrad, W. F.; Howard, K. P., The conformation of the pore region of the M2 proton channel depends on lipid bilayer environment. *Protein Sci.* **2005**, *14* (4), 856-861.
60. Kochendoerfer, G. G.; Salom, D.; Lear, J. D.; Wilk-Orescan, R.; Kent, S. B. H.; DeGrado, W. F., Total chemical synthesis of the integral membrane protein influenza A virus M2: Role of its C-terminal domain in tetramer assembly. *Biochemistry* **1999**, *38* (37), 11905-11913.

61. Ma, C. L.; Polishchuk, A. L.; Ohigashi, Y.; Stouffer, A. L.; Schon, A.; Magavern, E.; Jing, X. H.; Lear, J. D.; Freire, E.; Lamb, R. A.; DeGrado, W. F.; Pinto, L. H., Identification of the functional core of the influenza A virus A/M2 proton-selective ion channel. *Proc. Natl. Acad. Sci. USA* **2009**, *106* (30), 12283-12288.
62. Salom, D.; Hill, B. R.; Lear, J. D.; DeGrado, W. F., pH-dependent tetramerization and amantadine binding of the transmembrane helix of M2 from the influenza A virus. *Biochemistry* **2000**, *39* (46), 14160-14170.
63. Mould, J. A.; Drury, J. E.; Frings, S. M.; Kaupp, U. B.; Pekosz, A.; Lamb, R. A.; Pinto, L. H., Permeation and activation of the M2 ion channel of influenza A virus. *J. Biol. Chem.* **2000**, *275* (40), 31038-31050.
64. Mould, J. A.; Paterson, R. G.; Takeda, M.; Ohigashi, Y.; Venkataraman, P.; Lamb, R. A.; Pinto, L. H., Influenza B virus BM2 protein has ion channel activity that conducts protons across membranes. *Developmental Cell* **2003**, *5* (1), 175-184.
65. Tang, Y. J.; Zaitseva, F.; Lamb, R. A.; Pinto, L. H., The gate of the influenza virus M2 proton channel is formed by a single tryptophan residue. *J. Biol. Chem.* **2002**, *277* (42), 39880-39886.
66. Pielak, R. M.; Chou, J. J., Kinetic Analysis of the M2 Proton Conduction of the Influenza Virus. *J. Am. Chem. Soc.* **2010**, *132* (50), 17695-17697.
67. Yi, M.; Cross, T. A.; Zhou, H. X., A secondary gate as a mechanism for inhibition of the M2 proton channel by amantadine. *J. Phys. Chem. B* **2008**, *112* (27), 7977-7979.
68. Ma, C. L.; Fiorin, G.; Carnevale, V.; Wang, J.; Lamb, R. A.; Klein, M. L.; Wu, Y. B.; Pinto, L. H.; DeGrado, W. F., Asp44 Stabilizes the Trp41 Gate of the M2 Proton Channel of Influenza A Virus. *Structure* **2013**, *21* (11), 2033-2041.

69. Hu, J.; Fu, R.; Nishimura, K.; Zhang, L.; Zhou, H. X.; Busath, D. D.; Vijayvergiya, V.; Cross, T. A., Histidines, heart of the hydrogen ion channel from influenza A virus: Toward an understanding of conductance and proton selectivity. *Proc. Natl. Acad. Sci. USA* **2006**, *103* (18), 6865-6870.
70. Hu, F. H.; Schmidt-Rohr, K.; Hong, M., NMR Detection of pH-Dependent Histidine-Water Proton Exchange Reveals the Conduction Mechanism of a Transmembrane Proton Channel. *J. Am. Chem. Soc.* **2012**, *134* (8), 3703-3713.
71. Wang, J.; Qiu, J. X. Y.; Soto, C.; DeGrado, W. F., Structural and dynamic mechanisms for the function and inhibition of the M2 proton channel from influenza A virus. *Curr. Opin. Struct. Biol.* **2011**, *21* (1), 68-80.
72. Williams, J. K.; Zhang, Y.; Schmidt-Rohr, K.; Hong, M., pH-Dependent Conformation, Dynamics, and Aromatic Interaction of the Gating Tryptophan Residue of the Influenza M2 Proton Channel from Solid-State NMR. *Biophys. J.* **2013**, *104* (8), 1698-1708.
73. Pielak, R. M.; Chou, J. J., Influenza M2 proton channels. *Biochim. Biophys. Acta, Biomembr.* **2011**, *1808* (2), 522-529.
74. Hong, M.; DeGrado, W. F., Structural basis for proton conduction and inhibition by the influenza M2 protein. *Protein Sci.* **2012**, *21* (11), 1620-1633.
75. Zhou, H. X., Mechanistic Insight into the H<sub>2</sub>O/D<sub>2</sub>O Isotope Effect in the Proton Transport of the Influenza Virus M2 Protein. *J. Membr. Biol.* **2011**, *244* (2), 93-96.
76. Zhou, H. X., A Theory for the Proton Transport of the Influenza Virus M2 Protein: Extensive Test against Conductance Data. *Biophys. J.* **2011**, *100* (4), 912-921.
77. Leiding, T.; Wang, J.; Martinsson, J.; DeGrado, W. F.; Arskold, S. P., Proton and

cation transport activity of the M2 proton channel from influenza A virus. *Proc. Natl. Acad. Sci. USA* **2010**, *107* (35), 15409-15414.

78. Schweighofer, K. J.; Pohorille, A., Computer simulation of ion channel gating: The M-2 channel of influenza A virus in a lipid bilayer. *Biophys. J.* **2000**, *78* (1), 150-163.

79. Liang, R. B.; Li, H.; Swanson, J. M. J.; Voth, G. A., Multiscale simulation reveals a multifaceted mechanism of proton permeation through the influenza A M2 proton channel. *Proc. Natl. Acad. Sci. USA* **2014**, *111* (26), 9396-9401.

80. Wei, C. Y.; Pohorille, A., Activation and Proton Transport Mechanism in Influenza A M2 Channel. *Biophys. J.* **2013**, *105* (9), 2036-2045.

81. Smith, K. K.; Kaufmann, K. J.; Huppert, D.; Gutman, M., Picosecond proton ejection: an ultrafast pH jump. *Chem. Phys. Lett.* **1979**, *64* (3), 522-527.

## Chapter 2: Proton Transport Mechanism of M2 Proton Channel Studied by Laser Induced pH-jump

[Reproduced with permission from Jeong, B.-S., Dyer R. B. (2017) Proton Transport Mechanism of M2 Proton Channel Studied by Laser Induced pH-jump, J Am Chem Soc 139 (19) 6621-6628. <http://doi.org/10.1021/jacs.7b00617> Copyright 2017 American Chemical Society]

### 2.1 Abstract

The M2 proton transport channel of the influenza virus A is an important model system because it conducts protons with high selectivity and uni-directionally when activated at low pH, despite the relative simplicity of its structure. Although it has been studied extensively, the molecular details of the pH-dependent gating and proton conductance mechanisms are incompletely understood. We report direct observation of the M2 proton channel activation process using a laser induced pH-jump coupled with tryptophan fluorescence as a probe. Biphasic kinetics is observed, with the fast phase corresponding to the His37 protonation, and the slow phase associated with the subsequent conformation change. Unusually fast His37 protonation was observed ( $2.0 \times 10^{10} \text{ M}^{-1} \text{ s}^{-1}$ ), implying the existence of proton collecting antennae for expedited proton transport. The conformation change ( $4 \times 10^3 \text{ s}^{-1}$ ) was about two orders of magnitude slower than protonation at endosomal pH, suggesting that a transporter model is likely not feasible.



## 2.2 Introduction

Protein mediated proton transport through active pumps or passive channels plays a crucial role in many biological processes, including oxidative phosphorylation, photophosphorylation, viral replication, and enzyme catalysis. The structure and function of proton pumps and channels have been the subjects of intensive studies aimed at a better understanding of proton transfer mechanisms.<sup>1,2</sup> The M2 proton channel of the influenza virus has been one of the most widely studied proton channels because of its relative simplicity and promise as a target for anti-influenza drug development. M2 is an ideal model system because it forms a minimalistic ion channel with interesting characteristics such as pH-dependent gating, high selectivity,<sup>3</sup> and unidirectional conductance<sup>4</sup>.

After endocytosis of a viral particle, the homotetrameric M2 proton channel is activated under lysosomal acidic pH, switching on proton conductance and acidifying the viral lumen to release viral ribonucleoproteins into the host cell cytosol.<sup>5</sup> The gating and proton conductance mechanisms that control these processes have been investigated extensively.<sup>6-8</sup> It is generally accepted that the His37 tetrad in the transmembrane domain is repeatedly protonated and deprotonated, likely alternating between the 2<sup>+</sup> and 3<sup>+</sup> states during the proton translocation cycle. This so-called proton shuttle mechanism of M2 proton channel is supported by the slow proton conduction rate (10~1000 H<sup>+</sup>/s), rectification, and the large deuterium isotope effect.<sup>6,8,9</sup> The shuttle mechanism also explains the leveling off of the conductance rate below pH 6.<sup>10,11</sup>

The conformational switch model postulates that protonation of His37 plays a central role in the gating of M2 proton channel.<sup>6</sup> In this model, the M2 proton channel forms a tightly

packed tetramer structure under basic to neutral pH conditions with the His37 tetrad postulated to be in protonation states between 0 and +2. Positively charged residues may be stabilized in the relatively low dielectric environment of the channel interior by hydrogen bonding with water molecules and cation- $\pi$  interactions (Figure 1a). As the pH is lowered to its endosomal value, the remaining histidines of the His37 tetrad are protonated, increasing the repulsion among the positively charged imidazolium cations, which subsequently induces dilation of the C-terminal ends of the M2 structure (Figure 1b).<sup>6,8,12-18</sup> In this activated form at acidic pH, the indole side chains of the Trp41 tetramer located near the C-termini, which were initially packed tightly at high pH, are loosened and more dynamic, and the channel becomes more accessible to water molecules.<sup>7,19-21</sup> A pH-dependent channel conformation change is supported by high-resolution structures at various pH values that exhibit a more dilated C-terminus at lower pH<sup>6</sup>, which is in agreement with molecular dynamics (MD) simulations.<sup>22</sup> Moreover, NMR studies have observed peak broadening at low pH, indicating increased conformational fluctuations of the activated form.<sup>15,18,23</sup> A detailed model of the channel opening and acid activation mechanism has been proposed based on multiscale reactive molecular dynamics and QM/MM calculations of the explicit proton transport behavior, including proton shuttling and charge delocalization on the His37 tetrad and pore water molecules.<sup>24,25</sup> This model accurately fits the available experimental data for the conductance and deprotonation rates.

While this model is supported by equilibrium data from various techniques, the interconversion between opened (activated, Figure 1b) and closed (inactivated, Figure 1a) conformations of the C-terminus has not been observed directly. Furthermore, there are still many gaps to be filled to complete the proton conductance mechanism of M2 proton channel. In

particular, it is still unclear whether proton conductance is transporter-like, in which the M2 proton channel alternates between closed and opened conformers during each proton transport cycle.<sup>26</sup> The rate of His37 protonation and conformational interconversion between the activated and inactivated forms need to be measured to resolve this question. However, most studies of M2 function have been conducted under equilibrium conditions at constant pH, and pre-steady-state kinetics experiments have not been possible, primarily because the kinetics of the pH dependent processes are too fast. Specifically, protonation of the His37 tetrad along with the M2 proton channel activation occurs in the sub-millisecond time regime, which is inaccessible by conventional rapid mixers.

We have developed a new approach to study pH induced protein conformational dynamics that employs a rapid laser-induced pH-jump to trigger M2 activation, coupled with time-resolved tryptophan (Trp) fluorescence spectroscopy to probe the protein response. The pH jump is accomplished by photolysis of a photo-acid, which releases free H<sup>+</sup> in a few tens of nanoseconds.<sup>27-29</sup> Similar approaches have been used to measure sub-millisecond time scale kinetics of protonation and subsequent processes, such as proton transfer processes in GFP variants<sup>30,31</sup>,  $\alpha$ -helix formation in poly-L-glutamate<sup>32,33</sup>, histidine ligand dissociation from the heme of partially denatured cytochrome c<sup>34</sup>, acid-induced unfolding of myoglobin<sup>35</sup>, and leucine zipper folding<sup>36</sup>. In the present study, native Trp fluorescence was utilized as a probe to reveal the proton transfer and channel activation mechanism without perturbing the structure or dynamics of the system. This approach is technically challenging and represents the first instance of using Trp fluorescence as a nonperturbing probe for laser pH-jump experiments.

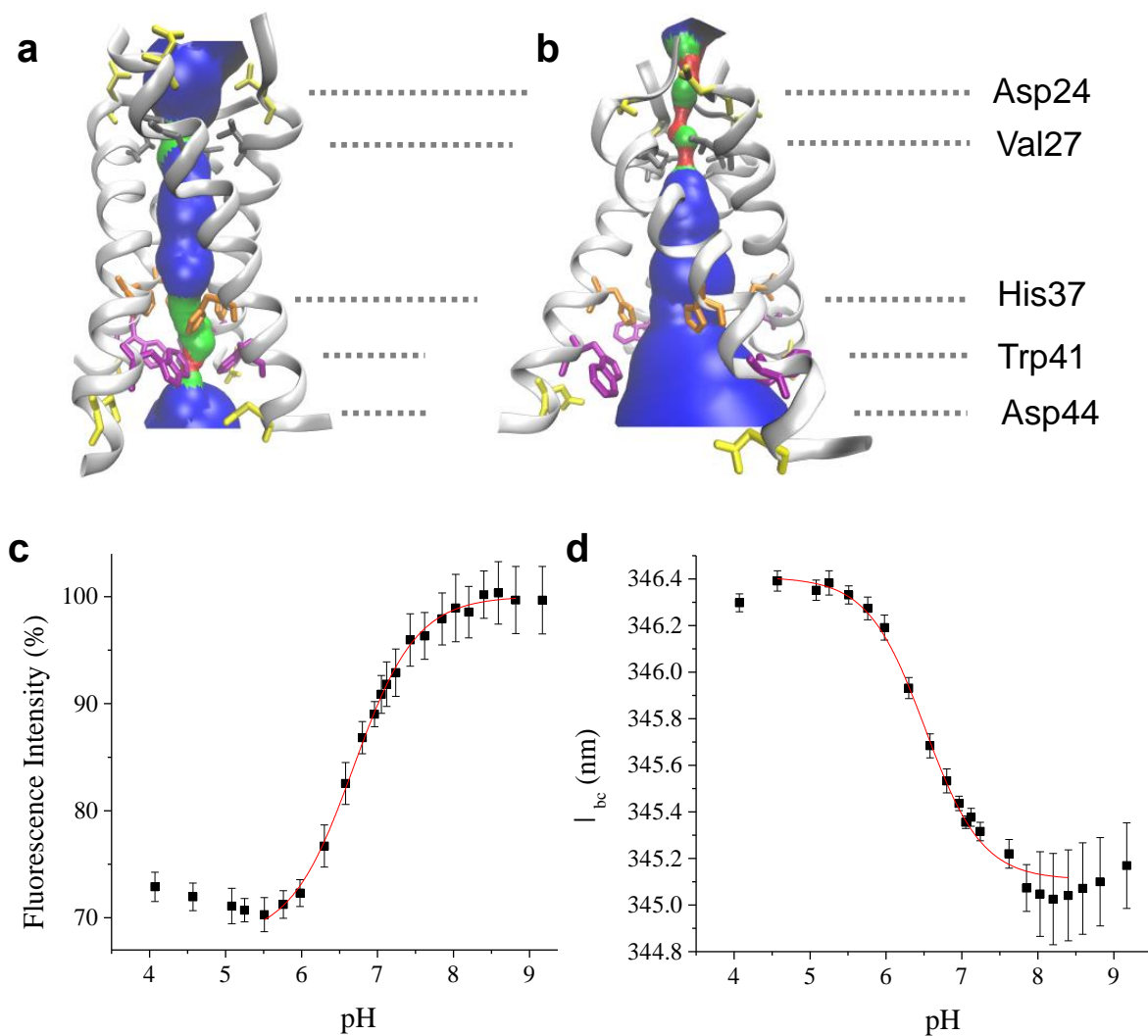


**Figure 2.1** pH dependence of the equilibrium structure of the M2TM tetramer. (a) M2TM structure from ssNMR spectroscopy at pH 6.5 (PDB ID 2L0J). (b) 3.5 Å X-ray structure of M2TM at pH 5.3 (PDB ID 3C9J). Pore lining residues and aspartic acid side chains are shown as sticks. The pore radius profile indicated with blue shading was calculated using the HOLE program.<sup>37</sup> (c) pH dependence of Trp fluorescence intensity and (d) of Trp fluorescence barycenter for the M2TM tetramer reconstituted in a DPPC bicelle. Solid red lines are fits to the Hill equation.

Using this approach, we detect the His37 protonation and the subsequent response of M2 proton channel on the sub-millisecond time scale. The Trp fluorescence decays in response to the rapid pH-jump, in two well separated kinetics phases. The fast phase is attributed to the protonation of His37 based on its pH dependence, and the slow phase is assigned to the subsequent conformation change, specifically C-terminus dilation, confirming previous postulations from equilibrium studies. The His37 protonation kinetics is comparable to that of a surface exposed ionizable residue, implying the presence of proton-collecting antenna residues near the channel orifice. The rate of conformational change of M2 proton channel after protonation of the His37 tetrad is about two orders of magnitude slower than the protonation rate at lysosomal pH, which is difficult to reconcile with a transporter-like mechanism. Instead, we propose that each proton transport cycle does not necessarily require a conformational change once M2 is activated.

## 2.3 Experimental Section

**Peptide synthesis.** Influenza A Udorn strain M2 proton channel transmembrane domain (M2TM) (Ser22 to Leu46: SSDPLVVAASIIIGILHLILWILDRL) was synthesized via standard 9-fluorenylmethoxycarbonyl (Fmoc)-based solid-phase chemistry in a microwave peptide synthesizer (CEM). Fmoc-PAL-PS resin (Applied Biosystems, Foster City, CA) was used to form a peptide amide. Peptide cleavage was performed using a cocktail of 90% trifluoroacetic acid (TFA), 5% thioanisole, 3% ethanedithiol, and 2% anisole for 180 min. The resulting mixture was filtered and precipitated in ice-cold ether. The peptide was purified by reverse phase-HPLC on a C-3 preparative column with a linear gradient of buffer A (0.1%

TFA in H<sub>2</sub>O) and buffer B (60% isopropyl alcohol, 30% acetonitrile, 10% H<sub>2</sub>O, 0.1% TFA).<sup>38</sup> The peptide eluted at 65% of buffer B. The purified peptide was verified by MALDI mass spectroscopy and then lyophilized.

**Sample preparation.** All detergents and lipids were purchased from Avanti Polar Lipids. The concentration of M2TM in ethanol was calculated from its UV-Vis absorption spectrum using  $\epsilon_{280} = 5,850 \text{ M}^{-1}\cdot\text{cm}^{-1}$ .<sup>39</sup> M2TM tetramers were reconstituted in bicelles by co-dissolving 273  $\mu\text{g}$  of M2TM peptide (0.1  $\mu\text{mol}$ ) in ethanol with 24.1 mg of 1,2-diheptanoyl-sn-glycero-3-phosphocholine (DHPC) (50  $\mu\text{mol}$ ) and 7.3 mg of 1,2-dipalmitoyl-sn-glycero-3-phosphocholine (DPPC) (10  $\mu\text{mol}$ ) in chloroform. The peptide to lipid ratio (M2TM:DPPC) was 1:100 (mol:mol) to ensure that M2TM tetramer was sufficiently formed in the lipid bilayer.<sup>40,41</sup> After thorough mixing, the lipid cake was prepared by drying under a N<sub>2</sub> stream and then under high vacuum for 2 hours. The lipid cake was hydrated by adding 1 ml of buffer solution and then repeating multiple freeze/thaw cycles. In every freeze and thaw cycle, the solution was thoroughly sonicated, and the cycle was repeated at least 10 times until the solution became clear. Drug binding is a well-established indicator of the formation of the functional tetramer; for our conditions amantadine binding to the M2 tetramer was verified by circular dichroism (CD) and fluorescence titrations (Figs. S5, S6, S7).

1-(2-nitrophenyl)ethyl sulfate (NPE-sulfate) was synthesized as previously described.<sup>42</sup> The concentration of NPE-sulfate was calculated from its UV-Vis absorption spectrum using  $\epsilon_{355} = 500 \text{ M}^{-1}\cdot\text{cm}^{-1}$ . To prepare CO<sub>2</sub> free water, deionized water was boiled for 10 min and cooled down under an Ar atmosphere. For the pH jump experiment, a bicelle sample containing 0.8 mM NPE-sulfate, 10  $\mu\text{M}$  M2TM, 1 mM DPPC, 5 mM DHPC and 100 mM NaCl

was prepared and its pH was adjusted by NaOH under a N<sub>2</sub> stream. For steady state measurements, samples in the pH range 3.0-7.5 were prepared in 100 mM citrate-phosphate buffer, and samples in the pH range 7.5-9.0 were prepared in 100 mM Tris buffer.

**Laser induced pH jump probed with time-resolved Trp fluorescence.** A schematic of the pH jump experiment is shown in Figure S1. A 3<sup>rd</sup> harmonic pulse (355 nm, 10 ns, maximum power: ~ 50 mJ) from a Q-switched Nd:YAG laser (Quanta-ray GCR IV, Spectra Physics) was passed through a quartz cuvette (2 mm × 10 mm) along the 2 mm path to photolyze the photoacid. The probe beam (283 nm) was obtained by frequency tripling the 849 nm output of a mode-locked femtosecond Ti:Sapphire laser (Mira 900, Coherent). Pump and probe beams were made colinear using a dielectric mirror (CVI Melles Griot) to reflect the 355 nm pump and transmit the 283 nm probe to ensure they are completely overlapped in the sample. The pump beam diameter was about 3 mm and the probe beam illuminated the center of the activated volume. The fluorescence signal was measured orthogonal to the pump beam. The fluorescence emission was filtered by long-pass filters to reject light at wavelengths below 300 nm, and then detected by a gated PMT (Hamamatsu, H11526). In order to minimize stray light, two polarizers were installed in a cross-oriented configuration. A delay generator (DG535, Stanford Research System) controlled the timing of the gating signal. A photodiode detected the pump laser pulse as a timing signal for triggering data acquisition by a digitizing oscilloscope (Lecroy wavesurfer 62MXS-B, 600 MHz, 10 Gs/s). Under ideal conditions with minimal scattering, the time resolution is limited by the laser pulse width (10 ns) and the detector response (similar timescale), but with a large scattering peak and the necessity to gate the detector off/on, the actual time resolution

is limited to  $\sim 2.5 \mu\text{s}$ . During the pH jump experiment, the sample is illuminated by the probe beam only during data acquisition by using a shutter (Uniblitz), and the sample cuvette was flushed with nitrogen to prevent  $\text{CO}_2$  uptake. A temperature-controlled cuvette holder regulated the sample temperature. The concentration of NPE-sulfate was limited to 0.8 mM because it absorbs the 280 nm probe beam intensively. Because Trp fluorescence is weak and single-shot experiments produce a low signal to noise ratio (SNR), a probe beam power of  $\sim 3 \text{ mW}$  was used to increase the SNR. Baseline correction was accomplished by subtracting spectra measured without the pump beam. The initial pH was kept below pH 8.0 to avoid a high concentration of  $\text{OH}^-$ , which rapidly scavenges  $\text{H}^+$  released from the photo-acid. The time constant of protonation of WK dipeptide measured with this setup agrees with that of diffusion-limited protonation of pH indicator molecules.

**Steady state fluorescence measurements.** All fluorescence spectra were measured by exciting Trp at 280 nm using a Fluoromax (Jovin Yvon Horiba) dual fluorometer. The spectral barycenter ( $\lambda_{bc}$ ) was calculated according to the equation:

$$\lambda_{bc} = \frac{\sum_n (I_n \cdot \lambda_n)}{\sum_n I_n}$$

## 2.4 Results and Discussion

**Tryptophan fluorescence detects protonation of His37 tetrad of M2TM in DPPC bilayers.** The transmembrane domain of M2 proton channel (residues 25-46, M2TM) was used in this study because it represents a minimal but sufficient model that exhibits most of the functions of full length M2, including homotetrameric channel formation, selective proton transport, gating, vectorial conductance, and drug binding.<sup>38,39,43</sup> M2TM proton channel ex-



hibits a high proton selectivity of at least  $10^6$  over other biological monovalent cations such as potassium or sodium ions.<sup>3</sup> His37 is essential for this high selectivity as well as acid activation of M2TM proton channel. M2TM proton conductance is also unidirectional, from N-terminus to C-terminus. This rectification likely originates from Trp41 enclosing the N-terminal exit of the TM domain, which acts as a gate that prevents backward flow of protons.<sup>4,25</sup> M2TM was reconstituted as the homotetramer in DPPC:DHPC bicelles with  $q$  (DPPC:DHPC) = 0.2 and a diameter of about 4 nm<sup>44,45</sup>, to minimize light scattering from the membrane. Previous work has demonstrated that M2 proton channel can be reconstituted in bicelles with its native conformation and activity.<sup>46</sup>

The Trp fluorescence of M2TM in DPPC bicelles exhibits a pH dependence as shown in Figure 1, in agreement with previous studies.<sup>47,48</sup> As the pH is made acidic, the fluorescence intensity decreases (Fig. 1c) and its barycenter ( $\lambda_{bc}$ ) is red-shifted (Fig. 1d) due to protonation of the His37 tetrad and the associated conformational rearrangement. The fluorescence intensity is a sensitive probe of the protonation state of His37 because protonated imidazole is an efficient quencher of Trp fluorescence, therefore its interaction with Trp41 causes a decrease in the fluorescence quantum yield.<sup>49</sup> Trp41 and His37 are located one helical turn away from one another and form a stabilizing cation- $\pi$  intra-monomer interaction when His37 is protonated.<sup>50</sup> This effect is additive as the His37 is progressively protonated to form multiple cation- $\pi$  interactions. The fluorescence barycenter is sensitive to the degree of hydration of Trp, with increasing hydration causing it to red shift. At pH 8, the  $\lambda_{bc}$  of M2TM was 345.1 nm whereas at pH 5 it was 346.4 nm, indicating the Trps of M2TM in the lipid bilayer are more hydrated at acidic pH. This observation is consistent with the postulated C-

terminal dilation of M2TM (Fig. 1b), which alters the accessibility of Trp to water molecules as indicated by Stern-Volmer fluorescence titration<sup>48,51</sup> and ssNMR experiments.<sup>19</sup>

Since the Trp fluorescence reports on both the progressive protonation of the His37 tetrad and on the channel opening once the more fully protonated states are populated, we expected to observe multiple steps in the titration from pH 8 to 5. However, both the intensity and barycenter profiles were adequately fit to a single transition as shown in Figure 1. Each titration curve was fit with the Hill equation in an attempt to account for multiple proton binding steps and to assess possible cooperativity, yielding a  $pK_a$  value of  $6.68 \pm 0.03$  and a Hill coefficient of  $1.1 \pm 0.1$  for fluorescence intensity (Fig. 1c), and a  $pK_a$  value of  $6.51 \pm 0.03$  and Hill coefficient of  $1.2 \pm 0.1$  for the barycenter (Fig. 1d). The inability to resolve multiple steps may be due to significant overlap of the transitions, combined with the lack of specificity of the fluorescence changes. Above pH 8 and below pH 5.5 the pH profile does not reach a stable baseline, most likely due to the decreased stability of the tetramer above and below the physiological pH range,<sup>39,43</sup> making it difficult to fit the data to a multi-state model. Nevertheless, the different apparent  $pK_a$  values observed for the fluorescence intensity and barycenter suggests the transition is not a simple 2-state process. Furthermore the protonation and channel opening processes are cleanly separated in time as shown below, making it possible to distinguish the protonation steps and their  $pK_a$  values in the pH jump kinetics experiments.

**M2TM proton channel dynamics triggered by a laser pH-jump.** Pulsed laser excitation of NPE-sulfate results in photochemical release of a proton and thus a jump to lower pH in  $\sim 100$  ns; the transient fluorescence response is measured by continuous excitation of Trp at 280 nm and integrating the fluorescence signal as a function of time using a fast PMT detec-

tor. No change in Trp fluorescence was observed for control experiments with M2TM sample containing no NPE-sulfate, confirming that the transient fluorescence decrease is due to the pH jump and not a bleach of the Trp absorption by the intense pump pulse. Figure 2a shows the transient Trp fluorescence signal in response to the laser pH jump from pH 8.0 to 6.0 for M2TM reconstituted in DPPC bicelles. The fluorescence transient was fit to a double exponential function in this case, although jumps to higher final pH values were well fit by a single exponential.

The fast phase ( $k_1$ ) showed a  $\Delta[\text{H}^+]$  dependence (Fig. 2b), indicating this process is the bimolecular protonation of His37. In contrast, the slow phase ( $k_2$ ) did not exhibit any  $\Delta[\text{H}^+]$  dependence within the noise of the measurement (Fig. S8) and the rate was about two orders of magnitude slower than the fast phase. Hence,  $k_2$  is ascribed to a conformational change subsequent to His37 protonation that increases the accessibility of the tryptophans to water, further quenching the fluorescence. A schematic representation of these processes is shown in Figure 2c. The protonation rate constant,  $k_p = (2.0 \pm 0.4) \times 10^{10} \text{ M}^{-1} \text{ s}^{-1}$  and deprotonation rate constant  $k_d = (1 \pm 2) \times 10^4 \text{ s}^{-1}$  were obtained by fitting the  $[\text{H}^+]$  dependent transients to a pseudo first order kinetics model (Figure 2b). Considering the previously measured rate of protonation of a solvent exposed His is  $5 \times 10^9 \text{ M}^{-1} \text{ s}^{-1}$ , in agreement with the prediction of the Debye-Smoluchowski equation for the protonation of an uncharged residue on a protein surface,<sup>1</sup> a protonation kinetic constant of His37 that is comparable to that of a surface exposed carboxylate residue might seem unreasonable. The problem is exacerbated by the location of His37, buried in a pore with a constricted diameter, since histidine in this less accessible environment might be expected to exhibit slower protonation kinetics compared to an exposed histidine residue.

Unusually rapid proton transfer from bulk solution to a protonatable residue inside a protein has been observed previously for other proton channels and enzymes.<sup>52</sup> For example, the rate of proton transfer from bulk solution to the catalytic center of cytochrome c oxidase from *Rhodobacter sphaeroides* (CcO) was estimated to be  $10^{10} \text{ M}^{-1}\cdot\text{s}^{-1}$  at pH 6.5 based on the steady state  $\text{O}_2$  reduction rate, and increased to  $\sim 7 \times 10^{11} \text{ M}^{-1}\cdot\text{s}^{-1}$  at pH 9, assuming that protonation is the rate limiting step.<sup>53,54</sup> Protonation kinetics of E286 near the catalytic center was measured by a flow-flash experiment at pH 9.8, from which a rate of greater than  $2 \times 10^{13} \text{ M}^{-1}\cdot\text{s}^{-1}$  was determined for proton transfer through the D-pathway.<sup>55</sup> Kinetics of proton-coupled electron transfer in CcO triggered by CO photolysis at pH 9.5 showed a proton transport rate of  $\sim 2 \times 10^{13} \text{ M}^{-1}\cdot\text{s}^{-1}$  through the K-pathway.<sup>56</sup> For bacterial reaction centers at pH 8, a proton transport rate of  $\sim 1.5 \times 10^{11} \text{ M}^{-1}\cdot\text{s}^{-1}$  was calculated from the steady state turnover rate.<sup>53</sup> A fast protonation rate of  $4 \times 10^{11} \text{ M}^{-1}\cdot\text{s}^{-1}$  was measured for a protonatable residue in a  $\text{Ca}^{2+}$  channel.<sup>57</sup> The proton conductance rate of the  $\text{CF}_0$ , proton channel of  $\text{H}^+$ -ATPase, was  $2 \times 10^5 \text{ s}^{-1}$  in the range of pH 5.6 to 8.0, which corresponds to a proton transfer rate in the range of  $8 \times 10^{10}$  to  $2 \times 10^{13} \text{ M}^{-1}\cdot\text{s}^{-1}$ .<sup>58</sup> Finally, the high catalytic activity ( $7000 \text{ s}^{-1}$ ) of [FeFe]-hydrogenase from *Desulfovibrio desulfurican* at pH 8 requires a rapid proton uptake rate of  $\sim 1.5 \times 10^{12} \text{ M}^{-1}\cdot\text{s}^{-1}$ .<sup>59</sup>

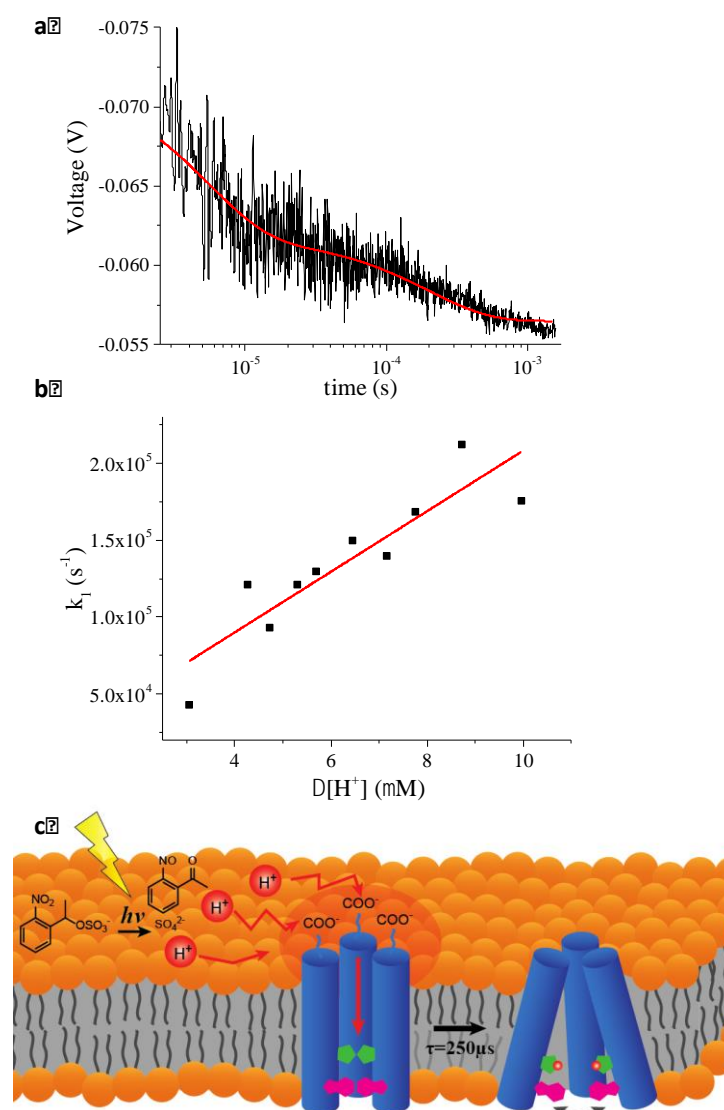


**Figure 2.2 M2TM dynamics triggered by a laser induced pH-jump.** (a) Time-dependent Trp fluorescence emission signal of a solution containing NPE-sulfate (0.8 mM) and M2TM reconstituted in a DPPC bicelle following a pH jump from pH 8.0 to 6.0, initiated with a 355 nm laser pulse. The data represent an average of 10 laser shots and were fit to a double exponential decay (red curve). (b) Dependence of the rate constant  $k_1$  of M2TM as a function of  $\Delta[H^+]$  at 25 °C. The red line is a linear fit to the data. (c) Schematic representation of the proton transfer pathway and proton channel activation process.

All of these examples exhibit protonation rates exceeding the diffusion-limited rate constant of proton transfer in aqueous solution ( $2\sim 6 \times 10^{10} \text{ M}^{-1} \cdot \text{s}^{-1}$ ). Protonated groups acting as a proton reservoir might facilitate the enhanced proton transport rates in some of these systems. For example, in CcO protonated E286 acts as a primary proton donor for both the pumping and chemical steps in  $\text{O}_2$  reduction. Proton antennas on the protein surface have been suggested as another explanation for enhanced proton transport rates. Ionizable residues near the entrance of the proton transfer pathway can effectively capture protons from bulk solution and then rapidly funnel them toward the channel orifice.<sup>60</sup> This idea has been tested for CcO by replacing ionizable residues near the entrance of proton transfer pathway with non-ionizable residues, which slows down the proton relay.<sup>56,61-63</sup>

We speculate that the higher than diffusion limited protonation rate of the His37 tetrad in M2TM is due in part to such a proton collecting antenna. Both influenza A and B M2 proton channels have negatively charged residues near the channel entrance which are highly conserved among different strains, specifically Asp21 and Asp24 for influenza A, and Glu3 for influenza B M2 proton channel. Because M2TM tetramer has only Asp24, a total of four aspartic acid carboxylate side chains in the ectodomain form a possible proton-collecting antenna as shown in Figure 3a. Each negatively charged carboxylate has a coulomb cage, in which electrostatic interaction between positively charged proton and negatively charged residue is stronger than the thermal energy ( $k_B T$ ). Due to their close proximity, their coulomb cages can merge and widen the proton capturing surface network, enhancing proton harvesting from bulk aqueous phase (Fig. 3b). Because the four aspartic acids work collectively, the apparent kinetic constant of protonation can exceed that of diffusion limited pro-

tonation rate of a single aspartic acid. We emphasize that this model is testable by mutation of Asp24 to a nonionizable residue.

There is growing evidence that protons can diffuse through the membrane-water interface with a faster diffusion rate than in bulk aqueous solution. A more rapid protonation rate of the pH indicator fluorescein on membrane surfaces has been observed experimentally compared to that in bulk solution, although the mechanism is not clearly understood.<sup>64-68</sup> Also, the NPE-sulfate photo-acid used in the present work can interact with lipid headgroups, and it is adsorbed on a phosphatidylcholine (PC) membrane surface with an adsorption constant of  $\sim 100 \text{ M}^{-1}$  (Figure S2). Interaction with the membrane increases the concentration of photo-acid as well as released protons near the membrane surface compared to the bulk. Coupled to enhanced interfacial proton diffusion, this may expedite proton transport to M2TM.

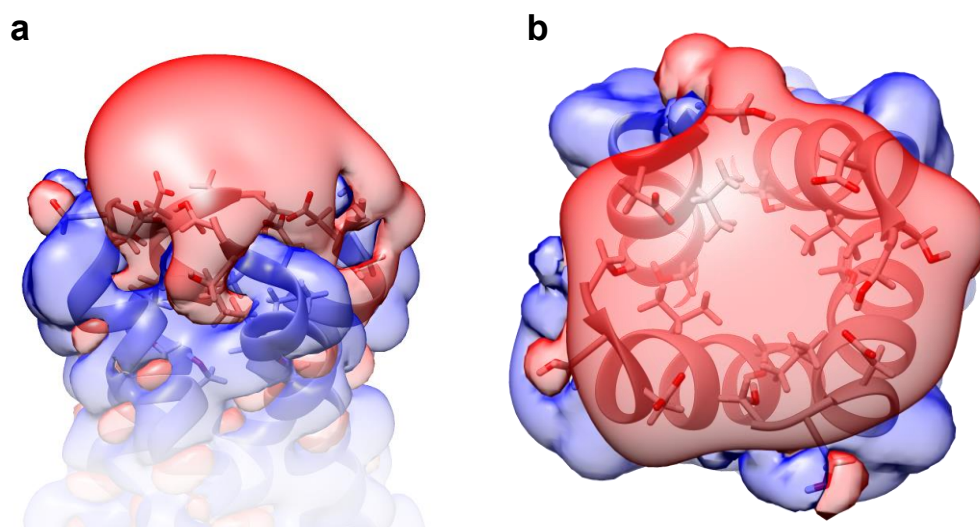


**Figure 2.3 Electrostatic properties of the N-terminal region of M2TM tetramer (PDB ID 2L0J).** (a) Side view and (b) top view of potential isocontour surfaces, shown at +1 kT/e (blue) and -1 kT/e (red). Electrostatic potential was computed using the Adaptive Poisson Boltzmann Solver (APBS) software package<sup>69</sup> for an ionic strength of 100 mM and fixing the charge of the N-terminus at zero.

After rapid initial protonation of the aspartic acid groups at the channel entry, the protons must dissociate to enter the channel. Considering the Asp pK<sub>a</sub> of ~4, the deprotonation rate would be about  $10^6 \text{ s}^{-1}$ , meaning proton dissociation occurs within 1  $\mu\text{s}$ . Following dissociation, protons are likely transported to the His37 tetrad within the pore through water wires that are formed by fluidic water molecules hydrating the pore.<sup>70</sup> Before protons enter the channel they pass through the Val27 neck, which is narrow enough to break the water wire and therefore might slow down proton entry into the pore to some extent. However, MD simulations suggest that the impact of the Val27 neck may not be significant because it dynamically interconverts between open and closed states with lifetimes in the nanosecond regime. The fast interconversion may allow water molecules to form transient hydrogen bonding network to facilitate proton transport through the Val27 neck.<sup>26,71,72</sup> The proton free energy profile (PMF) calculated by multiscale reactive molecular dynamics combined with QM/MM shows a relatively low 4.7 kcal/mol barrier from the viral exterior to the Val27 in the unprotonated state, which could be partially compensated by the proton gradient.<sup>25</sup> The PMF also shows a barrier from Val27 to His37 that might be due to electrostatic repulsion between the positively charged His37 and the incoming proton, hindering proton transfer. Hence, the overall protonation rate of His37 is faster than those of ionizable residues inside a pore without proton-collecting antenna residues, but in the range of the diffusion-limited rate due to the Val27 neck. This protonation rate is also in agreement with the rapid NH $\cdots$ N exchange rate of His37 ( $10^5 \text{ s}^{-1}$ ) measured by ssNMR at pH 5.2.<sup>73</sup>

We assign the slow kinetics phase to a conformation change of the channel, specifically C-terminus dilation subsequent to His37 protonation. Opening of the channel produces a more hydrated environment that further quenches the Trp fluorescence. The rate of channel open-



ing was calculated as  $k_2 = (4 \pm 2) \times 10^3 \text{ s}^{-1}$  from  $k_2^{app}$ . Compared to  $k_1$ , it is about two orders of magnitude slower, suggesting that the interconversion between activated and inactivated conformers might not occur during proton conductance. The proton conductance rate of M2 proton channel has been reported in the range of  $10 - 1000 \text{ s}^{-1}$ . Because the conformation change can be completed within a single conductance cycle at the upper limit of this range, the transporter model cannot be completely ruled out. The reverse transition from the open to closed conformation is likely faster compared to the forward one, because membrane exerts lateral pressure in the direction of the closed state. Since the protonation rate is much faster than any conformational rearrangement of channel backbones, however, it is more likely that deprotonated His37 would be re-protonated before the conformation change proceeds. This may explain why a large-amplitude motion between activated and inactivated conformations has not been observed by NMR under equilibrium conditions. However, the transporter model might still be feasible under certain conditions for which the proton entry rate is significantly slowed. It was proposed that the Val27 valve is blocked in the activated form, which might provide enough time for the channel to return to its closed form.<sup>26</sup> In counterpoint, MD simulations<sup>72</sup> and more rigorous multiscale reactive molecular dynamics combined with QM/MM calculations<sup>24</sup> suggested that Val27 is not completely closed even when three or four His37 are protonated. The simulations are consistent with NMR experiments that reveal a highly dynamic structure of the activated channel that allows the Val27 valve to fluctuate between open and closed configurations.

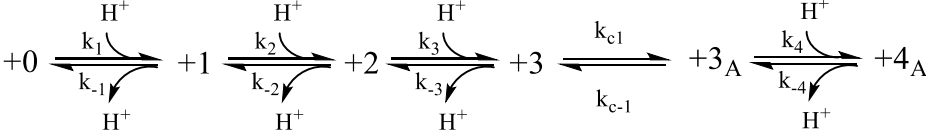
The rate-limiting step for proton conductance is thought to be proton dissociation from His37. Considering the protonation rate of  $(4 \pm 2) \times 10^{10} \text{ M}^{-1}\cdot\text{s}^{-1}$  and the  $\text{pK}_a \sim 6.5$  of His37, it follows that the deprotonation rate is  $\sim 10^4 \text{ s}^{-1}$ , which is one to three orders of magnitude

faster than the reported conductance rate. This disparity can be rationalized by futile cycles, in which protons are dissociated back in the direction of the channel entrance instead of out the channel exit. It could also be explained by the role of the Trp41 gate, since the calculated free energy barrier is highly asymmetric with a significantly higher barrier for His37 deprotonation.<sup>24,25</sup> The conductance is increased when Trp41 is mutated to Cys, Gly, Ala, or Phe, indicating that Trp41 slows down proton transport from His37 to the viral lumen.<sup>4</sup>

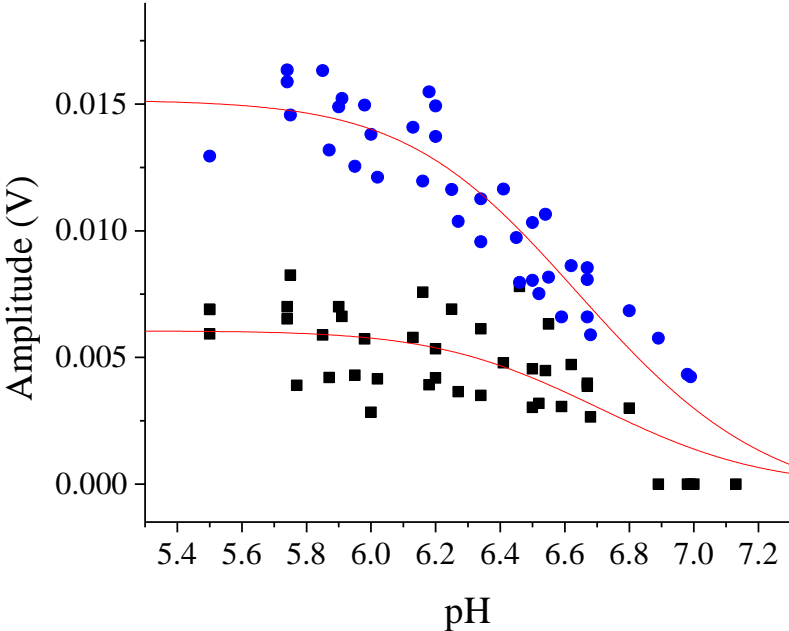
**Resolution of multiple His37 tetrad protonation steps.** In contrast with steady-state experiments, the pH jump measurements resolve the individual contributions of the protonation and conformation change steps to the fluorescence intensity change, since they are well separated in time. The fast phase originates from protonation of the His37 tetrad, and only a single lifetime was observed for this process, although multiple protonation steps occur. Since the protonation rates are all similar to one another, different deprotonation rates would be necessary to produce different  $pK_a$  values for the various His37 of the tetrad. The slow phase corresponds to the conformation change, and thus it occurs only after protonation of the third His37, but not before.

**Figure 2.4 Kinetic resolution of multi-step protonation of M2TM.** (a) Reaction scheme for progressive protonation and conformational change of M2TM. (b) Fluorescence amplitude change of  $k_1^{app}$  (circles) and  $k_2^{app}$  (squares) for M2TM in DPPC bicelles measured by pH jumps from an initial pH 7.5, as a function of final pH at 25 °C. (c) Steady-state pH dependent M2TM fluorescence intensity change (squares) along with the fit (red line) based on the polyprotic model shown in (a), with fluorescence intensities of 100% for 0 state, 95% for +1 state, 90% for +2 state, 75% for +3 state, and 70% for +4 state. The fraction of each protonation state of M2TM (dashed lines) was also calculated from the  $pK_a$  values obtained from this model.

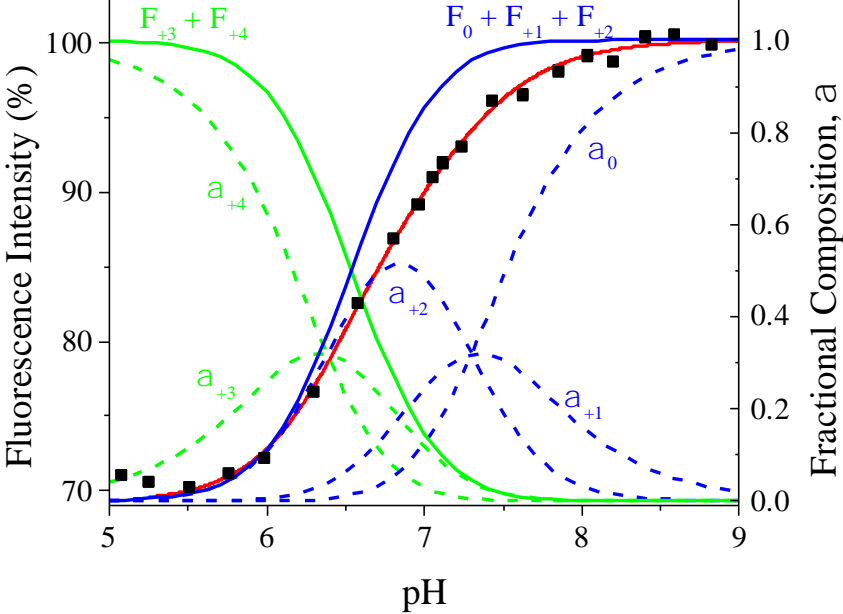
a?



b?



c?



We built a polyprotic model (Fig. 4a) to describe the equilibrium pH dependence of the Trp fluorescence, based on the kinetic resolution of the protonation and conformational change steps and a few reasonable assumptions. The amplitude change of both fast and slow phases as a function of final pH represents the population change of each protonation state. The M2TM tetramer can adopt multiple protonation states of the His37 tetrad, from 0 to 4<sup>+</sup> (Fig. 4a). After a pH jump, the population distribution of these protonation states is shifted to more highly protonated states. The amplitudes of the fast and slow kinetic phases as a function of final pH are plotted in Figure 4b. A rough estimate of the maximum signal change as a percent of the total fluorescence intensity for each kinetics phase was obtained from the fits, giving 20±3% for the fast phase and 10±3% for the slow phase. Because the fast phase corresponds to a convolution of all four protonation steps of the His37 tetrad, if we assume the protonation of each His37 contributes equally to the Trp fluorescence quenching, then each step reduces the total fluorescence intensity by 5%. If we also assume that the conformation change occurs only for the transition from the 2<sup>+</sup> to 3<sup>+</sup> state (consistent with simulations), the additional 10% decrement of the fluorescence intensity in the slow phase can be attributed to this transition. As a result, the relative fluorescence intensity was modeled as 100% for the 0 state, 95% for the 1<sup>+</sup> state, 90% for the 2<sup>+</sup> state, 75% for the 3<sup>+</sup> state, and 70% for the 4<sup>+</sup> state. Finally, we assumed that protonation steps 1 and 2 (pK<sub>a1</sub>), and steps 3 and 4 (pK<sub>a2</sub>) are cooperative, because the change in fluorescence intensity occurred in such a narrow range (pH 7.5~6), and cooperativity was observed in other studies of M2.<sup>25,74</sup>

We tested whether this polyprotic model fits the equilibrium pH-dependent fluorescence data (Fig. 4c). The model has two adjustable parameters, pK<sub>a1</sub> and pK<sub>a2</sub>. The fitting procedure calculates the population of each state, from which its weighted contribution to the total flu-

orescence intensity is determined based on the model described above (see Supporting Information for fit equations). The procedure is iterated to produce the best fit to the observed fluorescence intensities (red curve in Fig. 4c), yielding  $pK_{a1} = 6.38 \pm 0.03$  and  $pK_{a2} = 7.30 \pm 0.03$ . This model fits that data well and is more physically realistic than the overly simplified monoprotic model we used at first (Fig. 1c). The  $pK_a$  values are relatively high compared to previously reported values, but this is likely due to different membrane environments. A wide range of  $pK_a$  values has been reported for the His37 tetrad of M2TM, which has been rationalized in terms of the various conditions employed in these studies.<sup>23</sup> It is possible that our experiments in DPPC bicelles shift the  $pK_a$  values up due to the lack of cholesterol in the membrane preparations.

The  $pK_{a1}$  values obtained by fitting the amplitudes of the slow and fast kinetics phases (Fig 4b) were  $6.56 \pm 0.09$  and  $6.48 \pm 0.04$ , respectively;  $pK_{a2}$  was fixed at 7.3 for this calculation, based on its value derived from the steady state pH-dependent fluorescence data. The  $pK_{a1}$  values determined from equilibrium (6.38) and kinetics (6.48) experiments are close and likely the same within error considering the noise level of the single shot kinetics experiments. However, we note that the  $pK_a$  values determined from the kinetics experiment are not necessarily the same as those measured at equilibrium. During the pH jump experiment, protonation occurs before the conformation change, whereas, during a steady-state experiment, one can only measure properties of M2 channels that have already completed the conformation change. Therefore, it is possible that the kinetics experiment observes the  $pK_a$  of M2TM before activation, which could be different from that of the activated form populated in steady-state measurements.

## 2.5 Conclusions

A laser induced pH-jump coupled with time-resolved Trp fluorescence spectroscopy was used to measure the rapid protonation of His37 of M2TM and a subsequent conformational change that perturbs the micro-environment around Trp41. An unusually fast protonation rate for His37 ( $k_p = 1.6 \pm 0.4 \times 10^{10} \text{ M}^{-1} \text{ s}^{-1}$ ) in the pore of M2 proton channel was observed, implying a role of the Asp24 residues in the N-terminal domain of M2TM (and Asp 21 for full-length M2 proton channel) as proton-collecting antenna residues. Protonation of the His37 tetrad induces opening of the C-terminal end of the channel and exposure of Trp41 to water, with a rate of  $(4 \pm 2) \times 10^3 \text{ s}^{-1}$ . This temporal decoupling of the protonation step from the conformational change suggests that the transporter-like mechanism is probably not feasible. Instead, we propose that each proton transport cycle does not require a further conformational change after the activation of M2 by the channel opening, in agreement with QM/MM simulations.<sup>25</sup> Because M2 proton channel is sensitive to the environment, future experiments with different membrane compositions would be required to elucidate the specific impacts of the membrane structure and dynamics. Also, the addition of the C-terminal amphipathic helices to M2TM could affect its conformational dynamics. Finally, many other protein systems are amenable to this approach, such as ATP synthase, uncoupling protein, and hemagglutinin, all of which undergo functional conformational transitions induced by a change in pH. The laser pH-jump technique coupled with time resolved Trp fluorescence spectroscopy provides a powerful new methodology to study proton transport processes in general without perturbing their structure and function.

## 2.6 Appendix

1. Laser pH-jump Setup. The M2 Trp fluorescence decay kinetics triggered by a rapid laser pH-jump were measured with the instrument shown schematically in Figure S1. The pump-probe experiment uses a 7 ns pulse at 355 nm from a Q-switched Nd:YAG laser to produce the pH jump and a 290 nm quasi-continuous (76 MHz) probe beam generated by frequency tripling a fs mode-locked Ti:Sapphire laser.

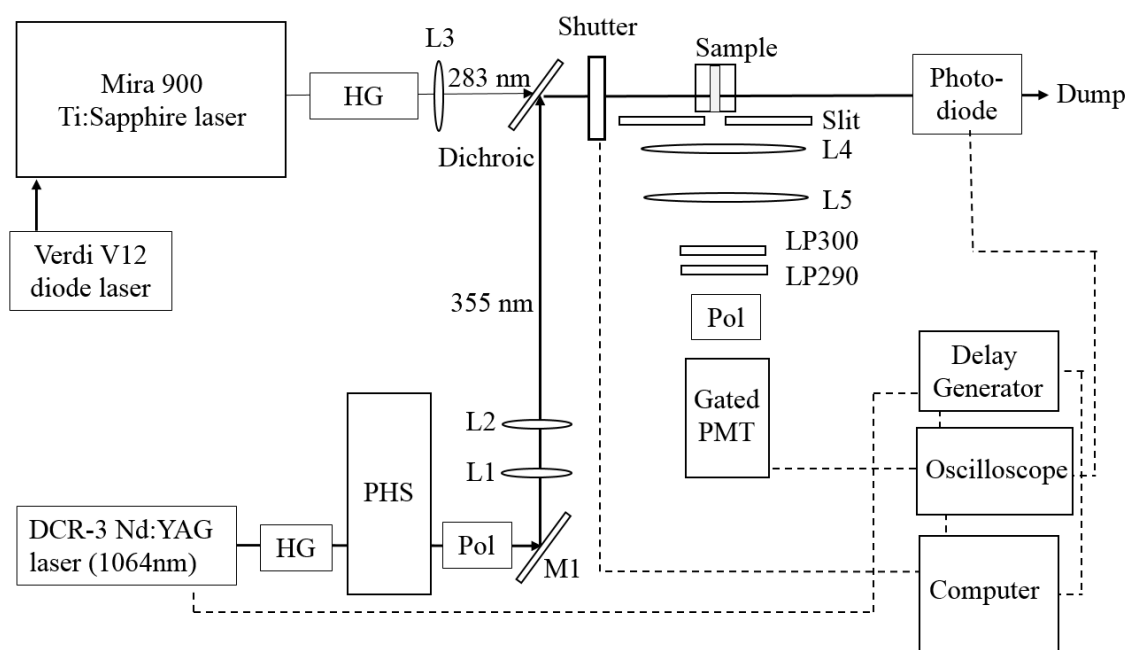


**Figure 2.S1.** Schematic of the pump-probe laser pH jump setup. (HG: harmonic generator. PHS: Prism Harmonic Separator, Pol: Polarizer, PMT: photomultiplier)

Trp fluorescence is a highly useful probe of protein dynamics in general, but many technical difficulties must be overcome in order to couple it to a pH jump experiment. The first problem is the overlap of the Trp fluorescence (centered near 350 nm) with the laser wavelength required to excite the photo acid (355 nm Nd:YAG third harmonic). Rejecting stray light

from scattering of the 355 nm pump beam is a tricky problem because of its spectral overlap with the Trp fluorescence. The usual approach of using a filter to block the 355 nm pump laser is not suitable in this case because it significantly reduces the Trp fluorescence signal as well. Instead, we reduced stray pump light by collecting the fluorescence light orthogonal to the pump axis, and installing two UV polarizers in a cross-polarized configuration before the detector. The crossed polarizers preferentially reject the scattered 355 nm pump pulse compared to the fluorescence, because its polarization is essentially unchanged whereas the fluorescence is depolarized. In addition, using a gated PMT the detector was gated off during pump illumination and then gated on at some later time for detection of the fluorescence. Finally, most photo acids, including NBA and its photochemical byproduct, absorb intensely at the 280 nm Trp excitation wavelength. This high absorbance causes a very severe inner-filter effect. Therefore, the NBA concentration must be limited such that it does not block the 280 nm probe beam, thereby restricting the maximum possible change of pH that is feasible with this approach to about 2 pH units.



## 2. pH-jump with Trp fluorescence pH indicator

The pH-jump setup was calibrated by generating a pH jump in the presence of a Trp fluorescence pH indicator, whose Trp fluorescence is pH dependent. Dipeptide L-Trp-L-Lys was selected as a Trp fluorescence pH indicator, because of its high quantum yield and pH sensitivity around pH 6~9. (Figure 2.S2).<sup>1</sup>

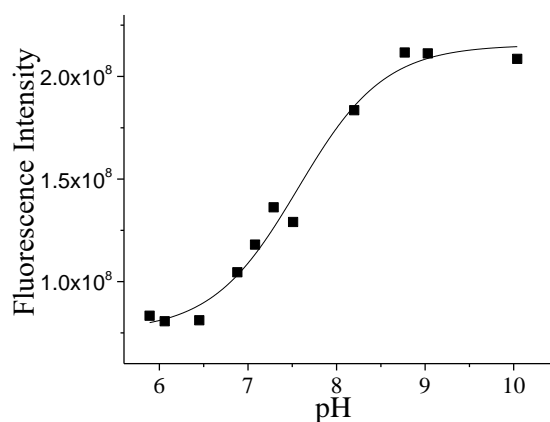


**Figure 2.S2.** The fluorescence titration curve of L-Trp-L-Lys (WK) dipeptide.<sup>1</sup>

A pH jump was conducted with 10  $\mu\text{M}$  of WK dipeptide in 1 mM NPE-sulfate photoacid solution at pH 8.5 (Figure S3). Protonation of the His was finished within a few  $\mu\text{s}$ , thus the complete process was resolved by the pH-jump instrument. This result demonstrated that it is possible to measure fast protonation kinetics triggered by laser pH jump and detected with Trp fluorescence as a probe. The apparent kinetics constants were plotted against  $\Delta[\text{H}^+]$  and the protonation rate of  $(3.8 \pm 0.3) \times 10^{10} \text{ M}^{-1}\text{s}^{-1}$  was calculated by linear fitting (Fig. 2.S3).

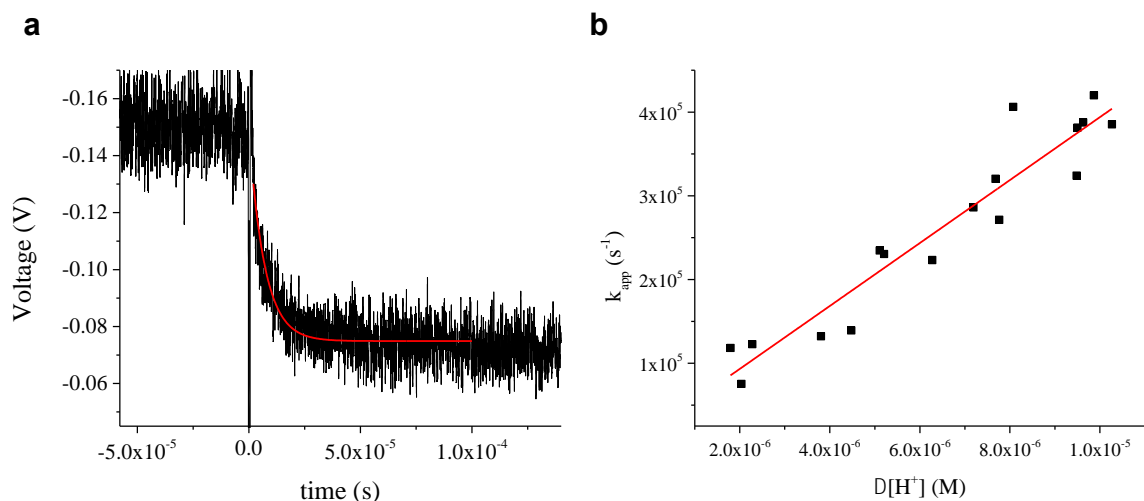


**Figure 2.S3.** pH jump with fluorescence detection of WK dipeptide. (a) Changes in the fluorescence emission (black line) of solution containing NPE-sulfate (1 mM) and WK (10  $\mu$ M) after pH jump. The fitting with a single exponential curve (red curve). (b) The apparent kinetics constants as a function of  $\Delta[H^+]$  at 25  $^{\circ}$ C.

### 3. Isothermal titration calorimetry (ITC)

Depending on the property of the photo acid, it can either partition into the membrane or adsorb on the surface of the membrane, altering the local concentration of photo acid at the membrane interface.<sup>2</sup> In order to measure the binding affinity of the NPE-sulfate photo acid to the membrane, isothermal titration calorimetry (ITC) was performed using a MicroCal VP-ITC (MicroCal LLC, Northampton, MA). 20  $\mu$ l aliquots of a 20 mM POPC SUV solution was titrated into 0.25 mM NPE-sulfate solution in the calorimeter cell. The heat of vesicle dilution was also measured as a control and subtracted from the photo acid data. The result was fit by equation (1).<sup>3</sup>

$$Q = K \cdot \frac{C_s^{ini}}{(1 + K \cdot C_l)^2} \cdot \Delta H + Q_{add}$$

(The symbols  $C_l$ ,  $C_s^{ini}$  denote lipid concentration and initial solute concentration, respectively. For more details, see reference 3.)

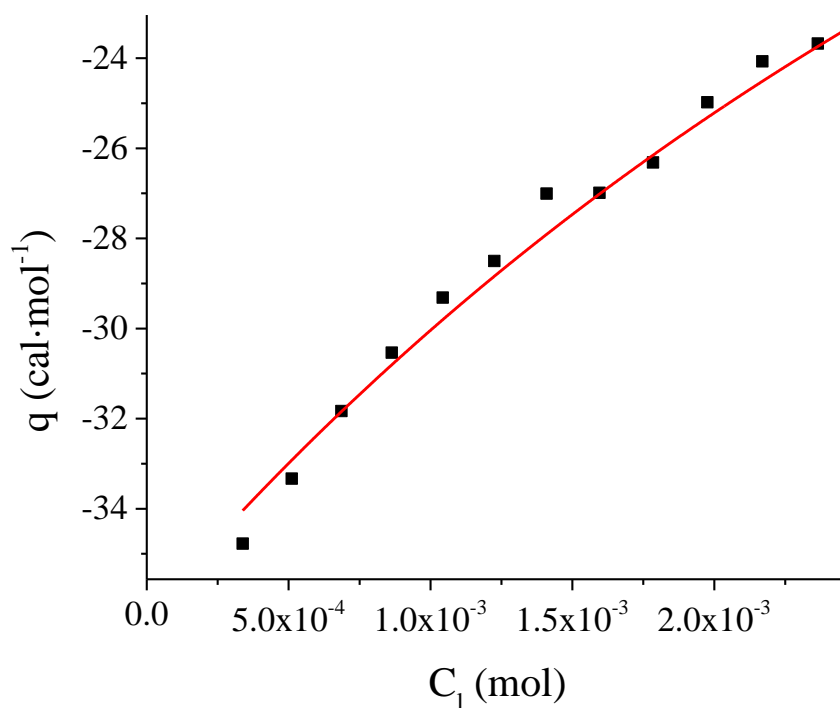


**Figure 2.S4.** Membrane adsorption thermodynamics of NPE-sulfate measured by ITC.

The best fit yielded  $K \approx 100 \text{ M}^{-1}$ ,  $\Delta H \approx 1.4 \text{ kcal}\cdot\text{mol}^{-1}$ ,  $\Delta G \approx -5 \text{ kcal}\cdot\text{mol}^{-1}$ ,  $\Delta S \approx 12 \text{ cal}\cdot\text{mol}^{-1}\cdot\text{K}^{-1}$ . The value of  $K$  ( $100 \text{ M}^{-1}$ ) indicates roughly one NPE-sulfate is bound to every 11.5 lipids.

## 4. Amantadine Drug Titration of M2TM in bicelles at pH 6.5

## a. CD spectra

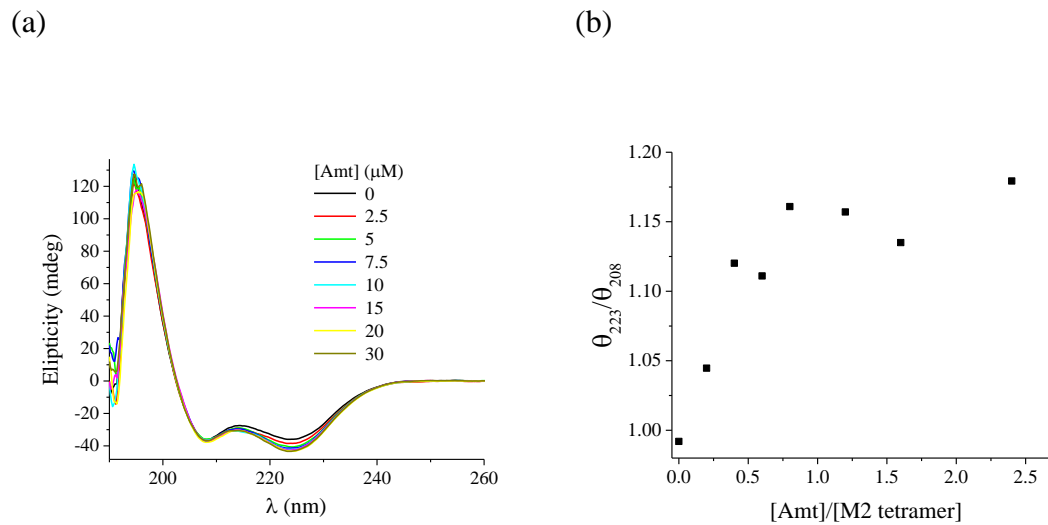


**Figure 2.S5** Amantadine titration to the 50  $\mu$ M M2TM in bicelle (DH(7)PC:DPPC=5:1, DPPC:peptide=100:1) at pH 6.5 (a) CD spectra of M2 proton channel with various concentration of Amt (b) The ratio between ellipticity at 223 nm and 208 nm as a function of the ratio of [Amt] to [M2 tetramer].

## b. Trp fluorescence spectra

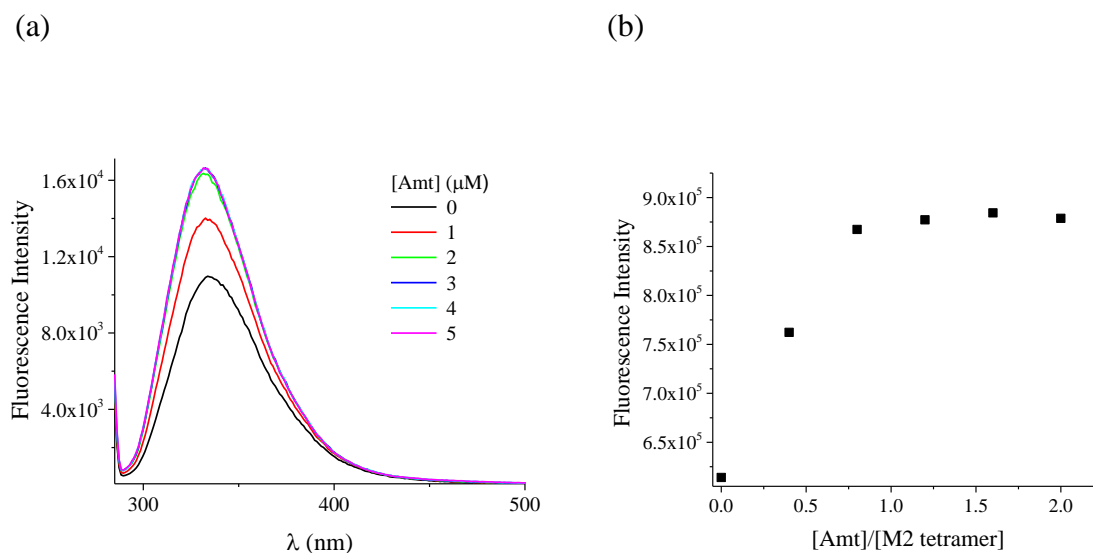


**Figure 2.S6** Amantadine titration to the 10  $\mu\text{M}$  M2TM in bicelle (DH(7)PC:DPPC=5:1, DPPC:peptide=100:1) at pH 6.5 (a) Trp fluorescence spectra of M2 proton channel with various concentration of Amt (b) The fluorescence intensity as a function of the ratio of [Amt] to [M2 tetramer].

In order to confirm that amantadine binds to M2TM with high affinity under our experimental conditions, the sample was titrated with amantadine. The results showed that the ratio between ellipticity at 223 nm and 208 nm<sup>4</sup> and Trp fluorescence<sup>5</sup> increase, consistent with previous work, indicating that the drug binds to M2TM tetramer with a stoichiometry of 1:1.

## 5. pH dependence of Trp fluorescence intensity with and without Amantadine in bicelles

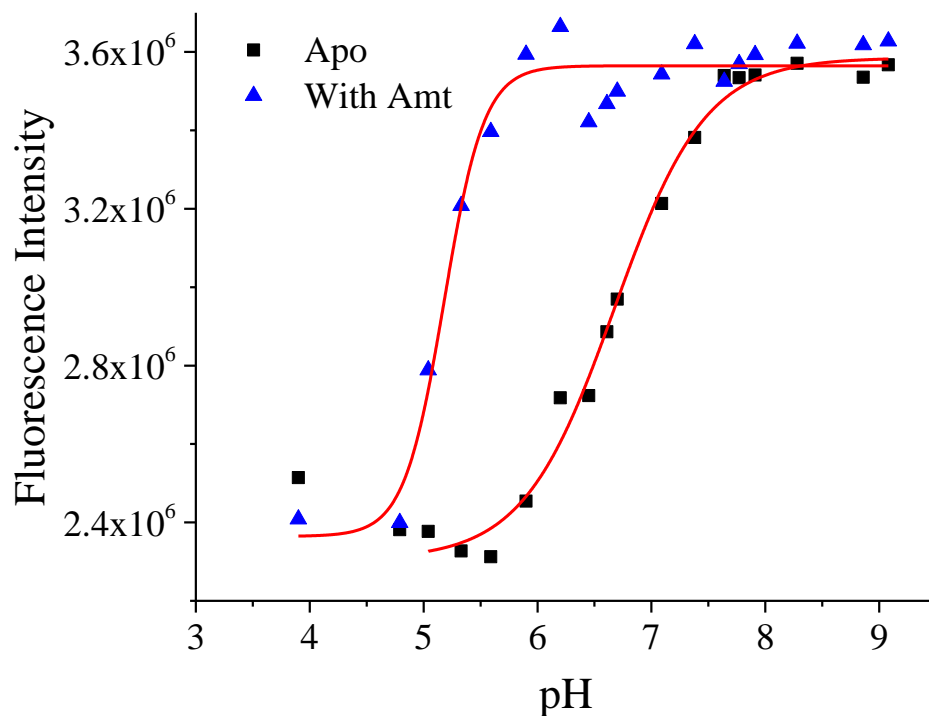


**Figure 2.S7** pH dependence of Trp fluorescence of the 10 $\mu$ M M2TM in bicelle (DH(7)PC:DPPC=5:1, DPPC:peptide=100:1) at various pH with/without 500 $\mu$ M Amantadine (Amt). After adding Amt, sample was incubated for 5 min. Solid red lines are fits to the Hill equation.

**Table 2.S1** Fitting parameters.

	pK <sub>a</sub>	n
Apo M2TM	6.67 $\pm$ 0.05	1.1 $\pm$ 0.1
With 500 $\mu$ M Amt	5.18 $\pm$ 0.05	2.5 $\pm$ 0.5

M2TM exhibited about one order lower  $pK_a$  value when amantadine is bound, which is in agreement with previous NMR study<sup>6</sup>.

#### 6. pH dependence of slow phase $k_2$ .

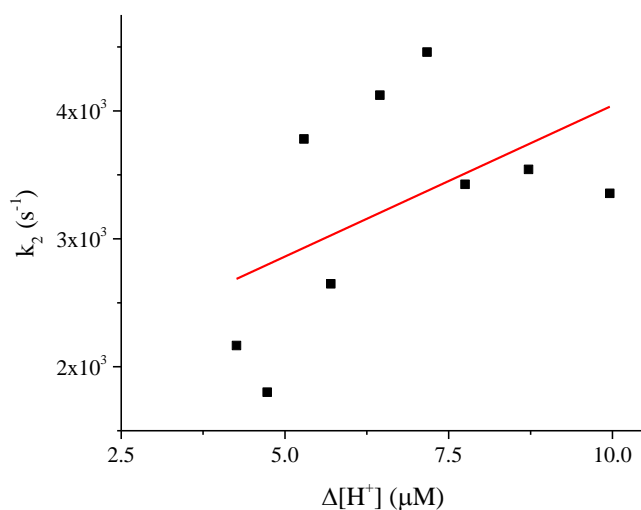


**Figure 2.S8** Dependence of the rate constant  $k_2$  of M2TM as a function of  $\Delta[H^+]$  at 25 °C.

The red line is a linear fit to the data.

In Figure S8, the data points are highly scattered, implying a low correlation between  $k_2$  and  $\Delta[H^+]$ . A linear fit had a high error range and the adjusted  $R^2$  value was 0.15. While the possibility of pH dependence of  $k_2$  can not be ruled out completely given the large uncertainty, the correlation is weak.

7. Procedure for fitting pH-dependent fluorescence data to the polyprotic model (Fig. 4c). The model has two adjustable parameters,  $pK_{a1}$  and  $pK_{a2}$ . The fitting procedure calculates the population of each state, from which its weighted contribution to the total fluorescence intensity is determined based on the following equation:

$$F_T = F \cdot \frac{0.7 \cdot 10^{-4pH} + 0.75 \cdot 10^{-pK_{a1}} \cdot 10^{-3pH} + 0.9 \cdot 10^{-2pK_{a1}} \cdot 10^{-2pH} + 0.95 \cdot 10^{-2pK_{a1}} \cdot 10^{-pK_{a2}} \cdot 10^{-pH} + 1 \cdot 10^{-2pK_{a1}} \cdot 10^{-2pK_{a2}}}{10^{-4pH} + 10^{-3pH} \cdot 10^{-pK_{a1}} + 10^{-2pH} \cdot 10^{-2pK_{a1}} + 10^{-pH} \cdot 10^{-2pK_{a1}} \cdot 10^{-pK_{a2}} + 10^{-2pK_{a1}} \cdot 10^{-2pK_{a2}}} - F_0$$

where  $F_T$  is the total fluorescence and  $F_0$  is a baseline offset.

## 8. Reference

- (1) Shinitzk.M; Goldman, R. *Eur. J. Biochem.* **1967**, 3, 139-144.
- (2) Geissler, D.; Antonenko, Y. N.; Schmidt, R.; Keller, S.; Krylova, O. O.; Wiesner, B.; Bendig, J.; Pohl, P.; Hagen, V. *Angew. Chem.-Int. Ed.* **2005**, 44, 1195-1198.
- (3) Heerklotz, H. *J. Phys.-Cond. Matt.* **2004**, 16, R441-R467.
- (4) Salom, D.; Hill, B. R.; Lear, J. D.; DeGrado, W. F. *Biochem.* **2000**, 39, 14160-14170.
- (5) Czabotar, P. E.; Martin, S. R.; Hay, A. J. *Virus Res.* **2004**, 99, 57-61.
- (6) Hu, J.; Fu, R.; Cross, T. A. *Biophys. J.* **2007**, 93, 276-83.



## 2.7 References

- (1) Gutman, M.; Nachliel, E. *Biochim. Biophys. Acta* **1990**, *1015*, 391-414.
- (2) Decoursey, T. E. *Physiol. Rev.* **2003**, *83*, 475-579.
- (3) Mould, J. A.; Drury, J. E.; Frings, S. M.; Kaupp, U. B.; Pekosz, A.; Lamb, R. A.; Pinto, L. H. *J Biol Chem* **2000**, *275*, 31038-31050.
- (4) Tang, Y. J.; Zaitseva, F.; Lamb, R. A.; Pinto, L. H. *J Biol Chem* **2002**, *277*, 39880-39886.
- (5) Helenius, A. *Cell* **1992**, *69*, 577-8.
- (6) Hong, M.; DeGrado, W. F. *Prot. Sci.* **2012**, *21*, 1620-1633.
- (7) Pielak, R. M.; Chou, J. J. *BBA - Biomembranes* **2011**, *1808*, 522-529.
- (8) Wang, J.; Qiu, J. X. Y.; Soto, C.; DeGrado, W. F. *Curr. Opin. Struct. Biol.* **2011**, *21*, 68-80.
- (9) Zhou, H. X. *J Membrane Biol* **2011**, *244*, 93-96.
- (10) Leiding, T.; Wang, J.; Martinsson, J.; DeGrado, W. F.; Arskold, S. P. *Proc. Natl. Acad. Sci. USA* **2010**, *107*, 15409-15414.
- (11) Pielak, R. M.; Chou, J. J. *J. Am. Chem. Soc.* **2010**, *132*, 17695-17697.
- (12) Stouffer, A. L.; Acharya, R.; Salom, D.; Levine, A. S.; Di Costanzo, L.; Soto, C. S.; Tereshko, V.; Nanda, V.; Stayrook, S.; DeGrado, W. F. *Nature* **2008**, *451*, 596-9.
- (13) Thomaston, J. L.; Nguyen, P. A.; Brown, E. C.; Upshur, M. A.; Wang, J.; DeGrado, W. F.; Howard, K. P. *Prot. Sci.* **2013**, *22*, 65-73.
- (14) Cady, S. D.; Schmidt-Rohr, K.; Wang, J.; Soto, C. S.; DeGrado, W. F.; Hong, M. *Nature* **2010**, *463*, 689-U127.
- (15) Schnell, J. R.; Chou, J. J. *Nature* **2008**, *451*, 591-U12.

- (16) Hu, F.; Luo, W.; Hong, M. *Science* **2010**, *330*, 505-508.
- (17) Hu, F. H.; Luo, W. B.; Cady, S. D.; Hong, M. *BBA - Biomembranes* **2011**, *1808*, 415-423.
- (18) Li, C.; Qin, H.; Gao, F. P.; Cross, T. A. *BBA - Biomembranes* **2007**, *1768*, 3162-3170.
- (19) Luo, W.; Hong, M. *J. Am. Chem. Soc.* **2010**, *132*, 2378-2384.
- (20) Williams, J. K.; Zhang, Y.; Schmidt-Rohr, K.; Hong, M. *Biophys. J.* **2013**, *104*, 1698-1708.
- (21) Ghosh, A.; Qiu, J.; DeGrado, W. F.; Hochstrasser, R. M. *Proc. Natl. Acad. Sci. USA* **2011**, *108*, 6115-6120.
- (22) Chen, W.; Huang, Y.; Shen, J. *J Phys Chem Lett* **2016**, *7*, 3961-3966.
- (23) Liao, S. Y.; Yang, Y.; Tietze, D.; Hong, M. *J Am Chem Soc* **2015**, *137*, 6067-77.
- (24) Liang, R.; Li, H.; Swanson, J. M. J.; Voth, G. A. *Proc. Natl. Acad. Sci. USA* **2014**, *111*, 9396-9401.
- (25) Liang, R.; Swanson, J. M.; Madsen, J. J.; Hong, M.; DeGrado, W. F.; Voth, G. A. *Proc. Natl. Acad. Sci. USA* **2016**, *113*, E6955-E6964.
- (26) Khurana, E.; Dal Peraro, M.; DeVane, R.; Vemparala, S.; DeGrado, W. F.; Klein, M. L. *Proc. Natl. Acad. Sci. USA* **2009**, *106*, 1069-1074.
- (27) Abbruzzetti, S.; Carcelli, M.; Rogolino, D.; Viappiani, C. *Photochem. Photobio. Sci.* **2003**, *2*, 796-800.
- (28) Abbruzzetti, S.; Sottini, S.; Viappiani, C.; Corrie, J. E. T. *J. Am. Chem. Soc.* **2005**, *127*, 9865-9874.
- (29) Donten, M. L.; Hamm, P. *Journal of Physical Chemistry Letters* **2011**, *2*, 1607-1611.

- (30) Abbruzzetti, S.; Grandi, E.; Viappiani, C.; Bologna, S.; Campanini, B.; Raboni, S.; Bettati, S.; Mozzarelli, A. *J. Am. Chem. Soc.* **2005**, *127*, 626-635.
- (31) Saxena, A. M.; Udgaonkar, J. B.; Krishnamoorthy, G. *Prot. Sci.* **2005**, *14*, 1787-1799.
- (32) Causgrove, T. P.; Dyer, R. B. *Chem. Phys.* **2006**, *323*, 2-10.
- (33) Donten, M. L.; Hamm, P. *Chem. Phys.* **2013**, *422*, 124-130.
- (34) Abbruzzetti, S.; Viappiani, C.; Small, J. R.; Libertini, L. J.; Small, E. W. *J. Am. Chem. Soc.* **2001**, *123*, 6649-6653.
- (35) Abbruzzetti, S.; Sottini, S.; Viappiani, C.; Corrie, J. E. T. *Photochem. Photobio. Sci.* **2006**, *5*, 621-628.
- (36) Hamm, P. *J. Phys. Chem. B* **2014**, *119*, 1425-1432.
- (37) Smart, O. S.; Goodfellow, J. M.; Wallace, B. A. *Biophys J* **1993**, *65*, 2455-60.
- (38) Kochendoerfer, G. G.; Salom, D.; Lear, J. D.; Wilk-Orescan, R.; Kent, S. B. H.; DeGrado, W. F. *Biochemistry-Us* **1999**, *38*, 11905-11913.
- (39) Ma, C. L.; Polishchuk, A. L.; Ohigashi, Y.; Stouffer, A. L.; Schon, A.; Magavern, E.; Jing, X. H.; Lear, J. D.; Freire, E.; Lamb, R. A.; DeGrado, W. F.; Pinto, L. H. *Proc. Natl. Acad. Sci. USA* **2009**, *106*, 12283-12288.
- (40) Georgieva, E. R.; Borbat, P. P.; Norman, H. D.; Freed, J. H. *Sci Rep* **2015**, *5*, 11757.
- (41) Cristian, L.; Lear, J. D.; DeGrado, W. F. *Proc. Natl. Acad. Sci. USA* **2003**, *100*, 14772-14777.
- (42) Barth, A.; Corrie, J. E. T. *Biophys. J.* **2002**, *83*, 2864-2871.
- (43) Salom, D.; Hill, B. R.; Lear, J. D.; DeGrado, W. F. *Biochemistry-Us* **2000**, *39*, 14160-14170.

- (44) Chou, J. J.; Baber, J. L.; Bax, A. J. *Biomol. NMR* **2004**, *29*, 299-308.
- (45) Luchette, P. A.; Vetman, T. N.; Prosser, R. S.; Hancock, R. E. W.; Nieh, M. P.; Glinka, C. J.; Krueger, S.; Katsaras, J. *BBA - Biomembranes* **2001**, *1513*, 83-94.
- (46) Claridge, J. K.; Aittoniemi, J.; Cooper, D. M.; Schnell, J. R. *Biochemistry-Us* **2013**, *52*, 8420-9.
- (47) Czabotar, P. E.; Martin, S. R.; Hay, A. J. *Virus Res.* **2004**, *99*, 57-61.
- (48) Nanda, V.; Cristian, L.; Toptygin, D.; Brand, L.; DeGrado, W. F. *Chem. Phys.* **2013**, *422*, 73-79.
- (49) Callis, P. R.; Liu, T. J. *Phys. Chem. B* **2004**, *108*, 4248-4259.
- (50) Okada, A.; Miura, T.; Takeuchi, H. *Biochemistry-Us* **2001**, *40*, 6053-6060.
- (51) Polishchuk, A. L.; Lear, J. D.; Ma, C. L.; Lamb, R. A.; Pinto, L. H.; DeGrado, W. F. *Biochemistry-Us* **2010**, *49*, 10061-10071.
- (52) DeCoursey, T. E. *Cell Mol Life Sci* **2008**, *65*, 2554-2573.
- (53) Adelroth, P.; Brzezinski, P. *Biochim Biophys Acta* **2004**, *1655*, 102-15.
- (54) Hosler, J. P.; Ferguson-Miller, S.; Mills, D. A. *Annu. Rev. Biochem.* **2006**, *75*, 165-187.
- (55) Namslauer, A.; Aagaard, A.; Katsonouri, A.; Brzezinski, P. *Biochemistry-Us* **2003**, *42*, 1488-98.
- (56) Ojemyr, L. N.; Lee, H. J.; Gennis, R. B.; Brzezinski, P. *Proc. Natl. Acad. Sci. USA* **2010**, *107*, 15763-15767.
- (57) Prod'hom, B.; Pietrobon, D.; Hess, P. *Nature* **1987**, *329*, 243-6.
- (58) Althoff, G.; Lill, H.; Junge, W. *J. Memb. Biol.* **1989**, *108*, 263-271.

- (59) Hatchikian, E. C.; Forget, N.; Fernandez, V. M.; Williams, R.; Cammack, R. *Eur. J. Biochem.* **1992**, *209*, 357-365.
- (60) Gutman, M.; Nachliel, E. *Annu. Rev. Phys. Chem.* **1997**, *48*, 329-56.
- (61) Fetter, J. R.; Qian, J.; Shapleigh, J.; Thomas, J. W.; Garciahorsman, A.; Schmidt, E.; Hosler, J.; Babcock, G. T.; Gennis, R. B.; Fergusonmiller, S. *Proc. Natl. Acad. Sci. USA* **1995**, *92*, 1604-1608.
- (62) Smirnova, I. A.; Adelroth, P.; Gennis, R. B.; Brzezinski, P. *Biochemistry-US* **1999**, *38*, 6826-6833.
- (63) Gorbikova, E. A.; Belevich, N. P.; Wikstrom, M.; Verkhovsky, M. I. *Biochemistry-US* **2007**, *46*, 13141-13148.
- (64) Heberle, J.; Riesle, J.; Thiedemann, G.; Oesterhelt, D.; Dencher, N. A. *Nature* **1994**, *370*, 379-382.
- (65) Prats, M.; Teissie, J.; Tocanne, J. F. *Nature* **1986**, *322*, 756-758.
- (66) Sanden, T.; Salomonsson, L.; Brzezinski, P.; Widengren, J. *Proc. Natl. Acad. Sci. USA* **2010**, *107*, 4129-4134.
- (67) Springer, A.; Hagen, V.; Cherepanov, D. A.; Antonenko, Y. N.; Pohl, P. *Proc. Natl. Acad. Sci. USA* **2011**, *108*, 14461-14466.
- (68) Medvedev, E. S.; Stuchebrukhov, A. A. *FEBS Lett* **2013**, *587*, 345-9.
- (69) Baker, N. A.; Sept, D.; Joseph, S.; Holst, M. J.; McCammon, J. A. *Proc. Natl. Acad. Sci. USA* **2001**, *98*, 10037-41.
- (70) Thomaston, J. L.; Alfonso-Prieto, M.; Woldeyes, R. A.; Fraser, J. S.; Klein, M. L.; Fiorin, G.; DeGrado, W. F. *Proc. Natl. Acad. Sci. USA* **2015**, *112*, 14260-5.
- (71) Yi, M.; Cross, T. A.; Zhou, H. X. *J. Phys. Chem. B* **2008**, *112*, 7977-7979.

- (72) Wei, C.; Pohorille, A. *Biophys. J.* **2013**, *105*, 2036-2045.
- (73) Hu, F. H.; Schmidt-Rohr, K.; Hong, M. *J. Am. Chem. Soc.* **2012**, *134*, 3703-3713.
- (74) Colvin, M. T.; Andreas, L. B.; Chou, J. J.; Griffin, R. G. *Biochemistry-US* **2014**, *53*, 5987-5994.

## **Chapter 3: pH Dependent Conformational Change of Influenza A M2**

### **Proton Channel Revealed by FRET**

#### **3.1 Abstract**

M2 proton channel of Influenza A virus is activated under acidic pH of lysosome, and conducts proton unidirectionally into the viral lumen with high selectivity. The M2 proton channel activation mechanism is of great interest, not only because of drug development, but also biophysical properties. It was proposed that the protonation of the third His of His37 tetrad induces channel conformation change, C-terminal dilation. However, there are contradicting reports about its pH-dependent conformational dynamics. Here, FRET was used to directly measure the distance change among M2TM C-termini in various pH. Channel opening was observed below pH 6.5, with  $pK_a$  of about 5.3. Amantadine (Amt) binding induced a transition toward more closed channel. This result confirms a strong correlation between activation and conformation change of M2 proton channel.

#### **3.2 Introduction**

Influenza A M2 proton channel play important roles in viral replication cycle, acidifying viral lumen to disassemble matrix 1 inner capsid layer, which is prerequisite of the release of viral ribonucleoprotein (RNP) complex. As a once effective drug target, it has been one of the most researched membrane proteins. It forms a homotetrameric channel in the viral membrane, conducting proton unidirectionally with high selectivity. Its proton conductivity is pH-dependent; acidic pH of lysosome activates M2 proton channel to conduct proton, but its detailed mechanism of channel activation remains controversial.

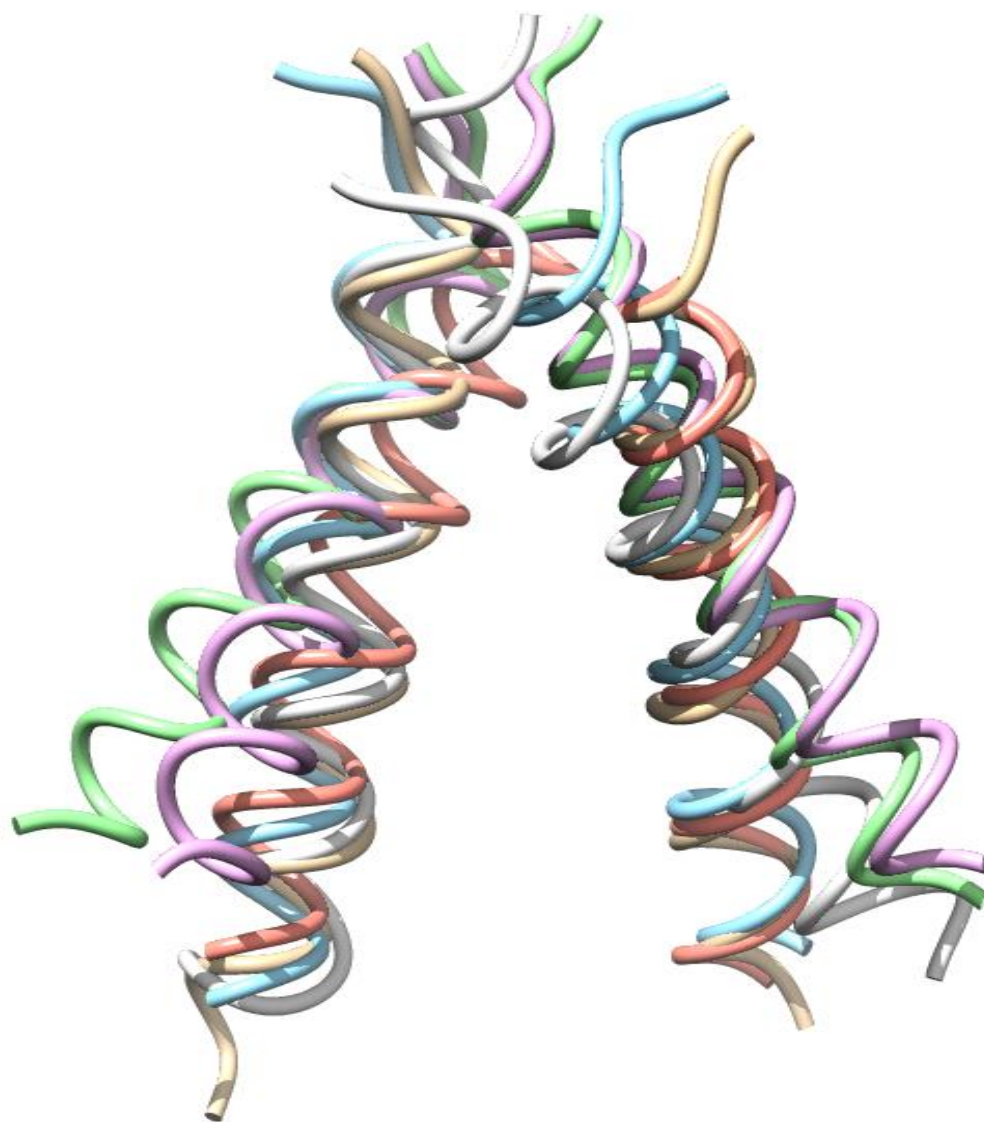


**Figure 3.1** Overlapped M2TM structures (PDB ID: 2L0J, 3LBW, 3C9J, 3BKD, 2KQT, 2RLF).

It was proposed that M2 proton channel activation is via changing its conformation at low pH, being triggered by protonation of His37 tetrad. Positively charged imidazolium cations electrostatically repels each other, resulting in dilated and more hydrated C-termini.<sup>4-5</sup> This can be inferred from a comparison among various protein structures (Figure 3.1), and further supported by computational studies.<sup>6-8</sup> The “activated” or “open” form was



observed in the X-ray crystal structure obtained by the Degradó lab<sup>11</sup>, exhibiting widely opened C-terminus region of M2 transmembrane domain (M2TM). (Figure 3.2a) However, there are still controversies whether it is artifact or not, especially because of the presence of interfacial contact between crystal lattice.<sup>15</sup> (Figure 3.2b) Later, the same group reported similar structure in lipid cubic phase (LCP) by using synchrotron<sup>16</sup> or X-ray free electron laser<sup>17</sup>, proving that the previous structure is not from crystal lattice artifact. Nevertheless, X-ray crystal structure of M2TM in LCP showed all similar backbone angle from basic (pH 8.0), intermediate (pH 6.5) to acidic pH (pH 5.5), contradicting the hypothesis that pH-

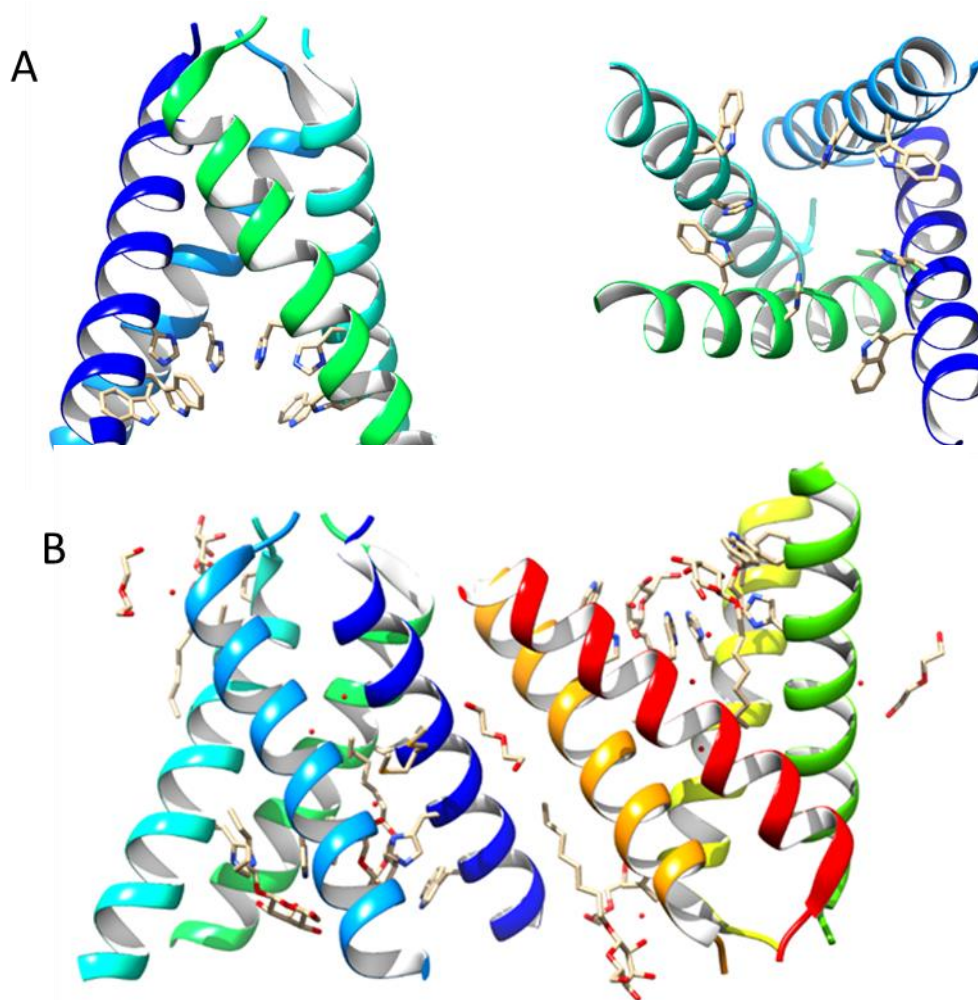


**Figure 3.2** (a) M2TM structure from 3BKD in side and axial view  
(b) Full structure of 3BKD

dependent conformational change causes M2 activation. Therefore, it is likely that the ‘open’ structure of M2TM originates from specific interaction between LCP and M2TM peptide.

On top of that, there is no other structure at acidic pH to reconfirm “activated” conformation. NMR technique experienced difficulty in obtaining M2TM structure at acidic pH because NMR peaks are severely broadened at acidic pH, implying dynamic interconversion among meta-stable conformations. Moreover, most NMR structures are measured in lipid bilayer environment, while X-ray crystal structures are in detergent, which can induce huge differences in membrane protein structure. Some of the structures reported in protein data base (PDB) and their experimental conditions are summarized in table 3.1.

Besides structural studies, various spectroscopic techniques were used to elucidate its pH-dependent conformational change. An EPR study found a more opened structure at pH 5.6 compared to the structure at pH 7.8.<sup>18</sup> Hochstrasser and coworkers used 2D-IR spectroscopy to study water dynamics of Gly34 in M2TM, and observed ice-like water at pH 8.0 and more bulk liquid-like water dynamics at pH 6.2.<sup>19</sup> And similar result was obtained by QM/MM simulation later.<sup>20</sup> Mei Hong and coworkers measured <sup>1</sup>H spin diffusion from water to M2TM, and their result indicated that water and M2TM contact area is decreased ~25% from open structure at pH 7.5 to close structure at pH 4.5.<sup>21</sup> It was reported that M2TM Trp fluorescence decays biexponentially after pH-jump experiment, revealing fast kinetics ascribed to protonation of His37 and about 250 μs of slow kinetics possibly corresponding to the subsequent conformational change.<sup>22</sup> Fluorescence correlation spectroscopy (FCS) was employed to study conformational dynamics of M2

proton channel backbone, demonstrating its dynamics in the time scale of several 100  $\mu$ s in pH-dependent manner.<sup>23</sup> However, the same group reported that hydration level and water dynamics at Trp41 position of 5-cyanoTrp41 M2TM mutant are same at both basic (pH 7.4) and acidic (pH 5.0) conditions by measuring both linear and non-linear IR spectra of cyano group reporter and fluorescence lifetime of 5-cyanoTrp41, although backbone angle change from 24.2° at pH 7.4 to 39.7° at pH 5.0 was observed by means of polarized

<b>PDB ID</b>	<b>pH</b>	<b>D1 (nm)</b>	<b>D2 (nm)</b>	<b>Condition</b>	<b>Peptide</b>	<b>Ref</b>
3C9J	5.3	3.252	3.715	X-ray, octyl- $\beta$ -d-glucopyranoside detergent, amantadine	S22-L46, G34A	1
3BKD	7.3	3.595	3.313	X-ray, octyl- $\beta$ -d-glucopyranoside detergent,	S22-L46, I33-SeMet	1
3LBW	6.5	2.336	2.299	X-ray, n-octylglucoside detergent	P25-L46, G34A	2
1NYJ	7.0	2.842	2.846	SS-NMR, DMPC lipid (C14)	S22-L46	3
2RLF	7.5	2.407	2.396	S-NMR, DHPC detergent (C4), rimantadine	S23-K60, C50S	9
2KAD	7.5	2.97	2.97	SS-NMR, DLPC lipid (C12), amantadine	S22-L46, L40A	10
2KQT	7.5	2.416	2.416	SS-NMR, DMPC lipid, amantadine	S22-L46	12
2L0J	7.5	2.93	2.88	SS-NMR, DOPC/DOPE bilayer	S22-G62, C50S	13
2H95	8.8	2.572	2.572	SS-NMR, DMPC bilayer	L26-L43,	14

**Table 3.1** Comparison of M2 proton channel structure, experimental technique, condition, peptide length, mutation. D1 and D2 are diagonal distances between  $\alpha$ -C of Leu46.

ATR-FTIR.<sup>24</sup> ssNMR study of M2TM W41F mutant observed pH-dependent two-state transition and their interconversion rate was about  $400\text{ s}^{-1}$ , which is somewhat slower than previous studies.<sup>25</sup>

From the past research, it is clear that there are reports that suggest contradicting results. Partially, this can be caused from different experimental conditions: as can be seen in table 1, structural studies from either X-ray crystal or NMR technique were conducted under different conditions such as membrane mimetic system, presence of a drug, mutation, and peptide length, which are known to have a big impact on the structure of M2 proton channel.<sup>26</sup> To clarify pH-dependent conformation change of M2 proton channel, all experimental conditions must be constant while the pH is being varied. Moreover, most structural data was obtained at cryogenic temperature, which doesn't take into account the dynamic nature of M2 proton channel structure, while most spectroscopic studies were conducted at ambient temperature, which is a more biologically relevant condition. The dynamics of M2 proton channel conformation change measured from various spectroscopic techniques also showed wide distribution from  $400\text{ s}^{-1}$  to  $12,500\text{ s}^{-1}$ .<sup>22-23, 25</sup> To some extent, such deviation can be originated from the intrinsic sensitivity of M2 proton channel to the environment. Even in a single report, conformational dynamics of M2 were varied from  $2,000\text{ s}^{-1}$  to  $12,500\text{ s}^{-1}$ , depending on pH, peptide length, and cholesterol content.<sup>23</sup> Such sensitivity may explain the deviation among studies conducted under different conditions of mutation, membrane composition and labeling method. On top of that, beside these factors, the deviation can be also contributed from the diverse spectroscopic approaches either in equilibrium condition or in pre-equilibrium state, in which different types of dynamics might be observed.

In the present work, under well-controlled condition, Förster resonance energy transfer (FRET), a so-called molecular ruler, was employed to confirm pH-dependent conformation change of M2 proton channel by measuring the distance among C-termini of M2TM tetramer in various pH. Moreover, the effect of drug binding, known to drive channel closure, was also studied. The result clearly demonstrates that acidic pH results in opening of channel C-terminus while the N-terminus stay nearly unchanged.

### **3.3 Experimental**

#### **Materials**

5-((2-Aminoethyl)amino)naphthalene-1-sulfonic acid (EDANS) C-2 maleimide, DABCYL plus<sup>TM</sup> C-2 maleimide were purchased from Anaspec, and used without further purification.

#### **Peptide Synthesis and Purification**

Cysteine was added either N- or C- termini of Influenza A Udorn strain M2 proton channel transmembrane domain (M2TM) (Ser22 to Leu46: SSDPLVVAASIIGILHLILWILDRL), to be synthesized via standard 9-fluorenylmethoxycarbonyl (Fmoc)-based solid-phase chemistry in a microwave peptide synthesizer (CEM). Fmoc-PAL-PS resin (Applied Biosystems, Foster City, CA) was used to form a peptide amide. Peptide cleavage was performed using a peptide cleavage solution comprised of 90% trifluoroacetic acid (TFA), 5% thioanisole, 3% ethanedithiol, and 2% anisole for two hours. The resulting mixture was filtered and the filtrate was added to cold ether to precipitate out the peptide. The peptide

was purified by reverse phase-HPLC on a C-3 preparative column with a linear gradient of buffer A (0.1% TFA in H<sub>2</sub>O) and buffer B (60% isopropyl alcohol, 30% acetonitrile, 10% H<sub>2</sub>O, 0.1% TFA).<sup>27</sup> The peptide eluted at 65% of buffer B. The purified peptide was verified by MALDI mass spectroscopy and then lyophilized.

### **Peptide Labeling**

5 mg of M2TM peptide was dissolved in a 2 ml solution of 60% 2,2,2-trifluoroethanol (TFE), 20% DI-water, and 20% 10mM pH 7 phosphate buffer. The pH of the solution was adjusted to be around pH 7 by adding 10mM of NaOH. Two equimolar of either EDANS or Dabcyl Plus<sup>TM</sup> C-2 maleimide was added to the solution, and the reaction was kept under dark for two hours. The labeled peptide was purified by reverse phase- HPLC on a C-3 preparative column with a linear gradient of buffer A (0.1% TFA in H<sub>2</sub>O) and buffer B (60% isopropyl alcohol, 30% acetonitrile, 10% H<sub>2</sub>O, 0.1% TFA). The purified peptide was verified by ESI mass spectroscopy. (Figure S1)

### **Sample Preparation**

All detergents and lipids were purchased from Avanti Polar Lipids. The concentrations of EDAN-M2TM and DABCYL-M2TM in ethanol were calculated from its UV-Vis absorption spectrum using  $\epsilon_{336} = 5,900 \text{ M}^{-1} \cdot \text{cm}^{-1}$  and  $\epsilon_{453} = 32,000 \text{ M}^{-1} \cdot \text{cm}^{-1}$ , respectively. Different ratios of EDANS to DABCYL Plus<sup>TM</sup> labeled M2TM were prepared in ratios of 1:1, 1:2, 1:4, 1:8, 8:1, 4:1, and 2:1. M2TM tetramers were reconstituted in bicelles by co-dissolving 0.2  $\mu\text{mol}$  of dye labeled M2TM peptide in ethanol with 24.1 mg of 1,2-diheptanoyl-sn-glycero-3-phosphocholine (DHPC) (50  $\mu\text{mol}$ ) and 7.3 mg of 1,2-

dipalmitoyl-sn-glycero-3-phosphocholine (DPPC) (10  $\mu\text{mol}$ ) in chloroform. The peptide to lipid ratio (M2TM:DPPC) was 1:50 (mol:mol) to ensure that M2TM tetramer was sufficiently formed in the lipid bilayer.<sup>28-29</sup> After thorough mixing, the lipid cake was prepared by drying under a  $\text{N}_2$  stream and then under high vacuum for 2 hours. The lipid cake was hydrated by adding 1 ml of buffer solution and then repeating multiple freeze/thaw cycles. In every freeze and thaw cycle, the solution was thoroughly sonicated, and the cycle was repeated at least 10 times until the solution became clear.

Each sample consisted of 20  $\mu\text{M}$  M2TM, 5 mM DHPC, 1 mM of DPPC, 100mM NaCl, and 100mM of phosphate, citrate, or tris buffer varying between pH 4 to 9.

### **Florescence Measurement**

For fluorescence spectra, Jobin Yvon dual fluorometer was used. Sample was excited at 336 nm. To measure pH-dependent fluorescence intensity change, fluorescence plate reader (Biotek Synergy HT) was used. The excitation filter was centered at 360 nm with band width 40 nm, and emission filter was centered at 460 nm with band width 40 nm. 100  $\mu\text{L}$  of samples were placed in a 96-well plate.

## **3.4 Results**

### **Selection of FRET Donor-Acceptor Pair**

To choose an optimal FRET pair, appropriate Förster radius ( $R_0$ ) was first considered by comparing M2 proton channel structures. (Table 1) The diagonal distances between Leu46 at the C-terminus end of M2TM tetramer range from 2.4 - 3.6 nm, thus, optimum Förster radius should be about  $3/\sqrt{2} = 2.12$  nm range. Such a short Förster radius is very rare, so

only few candidates were found. On top of that, one spectral characteristic of the dye should be its pH-independence. In other words, it should not have ionizable residue with pK<sub>a</sub> value in the range of pH 4~9. Moreover, a hydrophilic dye should be chosen to avoid interactions with the membrane. After all criteria were considered, EDANS-DABCYL<sup>+</sup> FRET pair ( $R_0 = 3.3$  nm) was chosen. They didn't show any pH-dependence in spectroscopic property. (Figure S2) Since DABCYL<sup>+</sup> is non-fluorescent quencher, FRET efficiency was calculated solely from EDANS fluorescence.

### **Fluorescence Spectra of FRET Labeled M2TM at pH 6.5**

After reconstitution of FRET labeled M2TM of 1:1 donor-acceptor ratio in DPPC bicelle, fluorescence spectrum was measured in pH 6.5 buffer. Compared to the free EDANS fluorescence at the same concentration, fluorescence was highly quenched, indicating donor-acceptor pair is in the range of Förster radius. Also, emission maxima at 495 nm was not shifted in bicelle solution, which means that EDANS dye is in bulk water phase. When amantadine was added, fluorescence intensity was decreased. It was reported that amantadine binds to the M2TM pore and makes M2TM tetramer more tightly closed, thus, the drug binding can quench more fluorescence. However, emission maxima was not changed, indicating that EDANS dye is still in bulk water phase. Such drug binding capability also demonstrates that M2TM forms a functional tetramer in DPPC bicelle. When detergent was added, fluorescence was recovered to some extent. Under high concentration of detergent, some of M2TM tetramer may become dissociated. Fluorescence maxima was blue-shifted because EDANS is an environmentally-sensitive fluorescence dye.



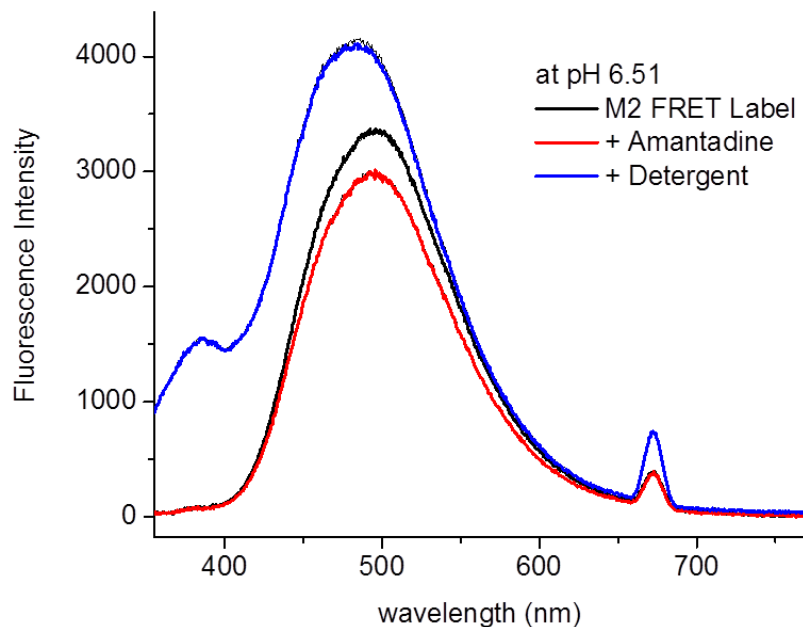


**Figure 3.3.** Fluorescence spectra of FRET labeled M2TM (EDANS : DABCYL<sup>+</sup> = 1 : 1) in DPPC bicelle in pH 6.5 buffer.

### pH-dependent FRET Efficiency Change

Because pH-dependent fluorescence spectrum of FRET labeled M2TM only shows intensity change, not spectral shift, a fluorescence plate reader could be used to compare fluorescence intensity more accurately with higher throughput.

Degrado et al. reported that tetramerization of M2TM in micelle is pH dependent.<sup>30</sup> To rule out a possibility of pH dependent tetramerization, as a control experiment, M2TM N-terminus were labeled with the FRET pair, EDANS and DABCYL<sup>+</sup>. When M2TM was labeled at N-terminus, there was almost negligible pH-dependence (figure 4a), confirming that M2TM forms a stable tetramer in this experimental condition. On the other hand, when

C-terminus of M2TM was labeled, pH-dependence of fluorescence intensity was observed. (figure 4b)

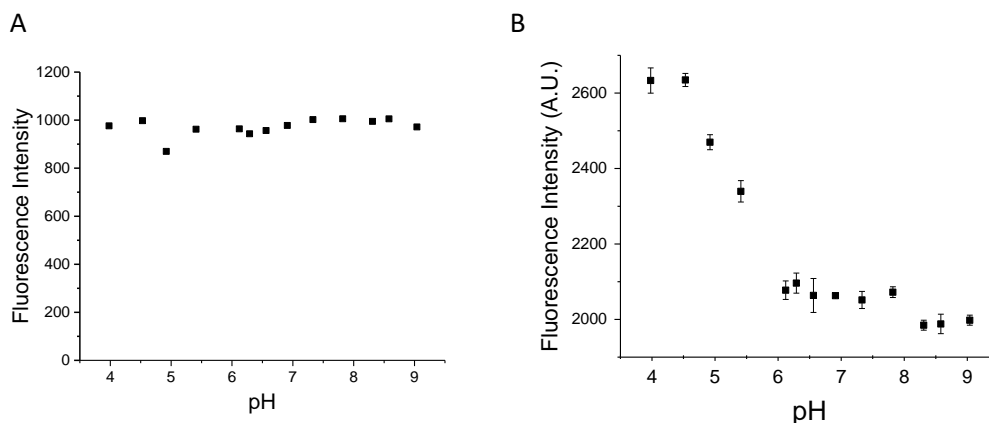


**Figure 3.4** Fluorescence intensity change of (a) N-terminus labeled M2TM, (b) C-terminus labeled M2TM in DPPC bicelle as a function of pH.

The fluorescence intensity of free EDANS was assumed as a non-quenched donor fluorescence intensity, and FRET efficiency was calculated. (Figure 3.5) It is clearly shown that FRET efficiency rapidly drops below pH 6.5, and, for  $r=0.125$  sample,  $pK_a$  5.3 was calculated by fitting with the Henderson-Hasselbalch equation. With amantadine, FRET efficiency was decreased above pH 6, indicating a even more closed structure than “close” structure of apo-M2TM. This agrees with previous reports; drug-binding induces more tightly packed tetramer than apo-M2 proton channel, dehydrating channel, as well as reduced backbone and sidechain dynamics.<sup>31</sup> Below pH 6, it shows similar transition to open structure with the similar  $pK_a$  value of 5.2, and eventually merged to the same level with Apo M2TM. Other sample with different ratio (D/A) showed similar trend, but slightly different  $pK_a$  values within experimental error range. (Figure S3)

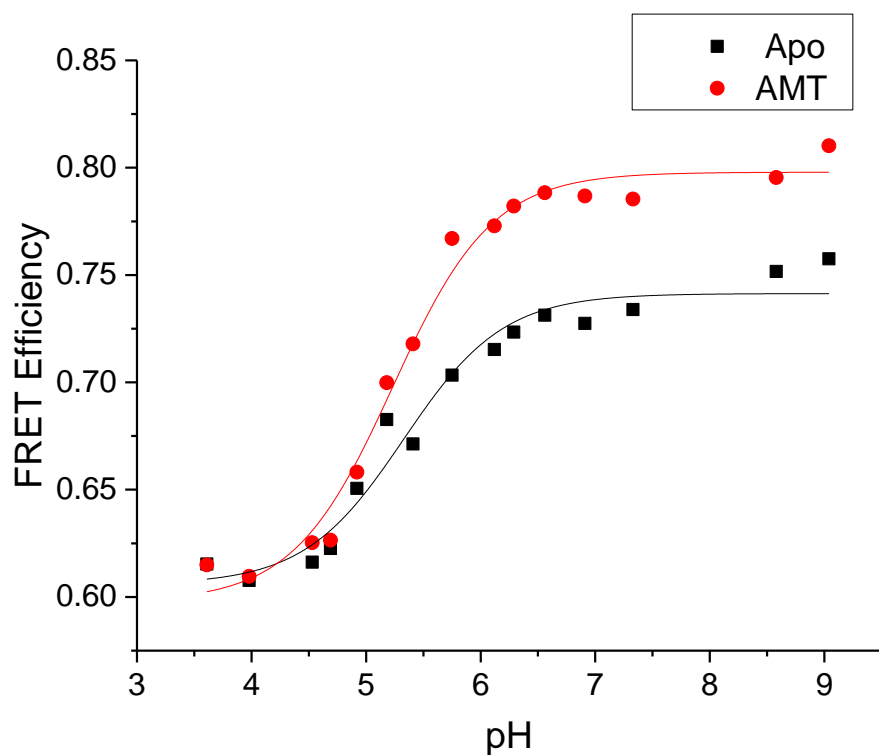


**Figure 3.5** FRET efficiency of M2TM (D/A=0.125) as a function of pH with/without amantadine (Amt).

### 3.5 Discussion

Influenza A M2 proton channel exhibits pH-dependent channel activity: at basic and neutral pH, it is inactive, but at acidic pH, it is activated. This activation mechanism of M2 proton channel, as well as its proton conductance mechanism, have been of great interest to many researchers.

We measured C-terminus conformation change of M2TM directly by FRET experiment. It was clearly shown that M2TM undergo transition to more opened structure as pH becomes

acidic. And the pK<sub>a</sub> value 5.3 of this transition was obtained by fitting. So far, various pK<sub>a</sub> values have been reported. (Table 3.2)

pK <sub>a</sub>	Technique	Condition	Ref
6.4, 5.7	CD	DPC micelle, 5.7 was estimated from electrophysiology data, S22-L46	<sup>32</sup>
8.2, 8.2, 6.3, <5.0	ssNMR	DMPC/DMPG, peptide:lipid = 1:20, S22-L46	<sup>33</sup>
7.6, 6.8, 4.9, 4.2	ssNMR	VM(SM:DPPC:DPPE:Chol=28:21:21:30), peptide:lipid = 1:15, S22-L46	<sup>34</sup>
7.1, 5.2	ssNMR	VM+(POPC:POPE:SM:Chol=25.6:25.6:25.6:23), peptide:lipid = 1:22.5, D21-E97	<sup>35</sup>
7.63, 4.52	sNMR	4-Me16:0PC, peptide:lipid = 1:6, R18-K60	<sup>36</sup>
6.9, 5.6	Fluorescence	POPC:POPG:cholesterol = 4:1:2, Mixture of M2TM(22-46) and Azulene M2TM	<sup>37</sup>
5.7, 4.0	UV-RR	POPE/POPS	<sup>38</sup>

**Table 3.2** Reported pK<sub>a</sub> values of M2 proton channel.

In most cases, pK<sub>a</sub> 5.3 is close to the pK<sub>a</sub> of 3<sup>rd</sup> His37 of tetrad, which agrees with previous notion that 3<sup>rd</sup> histidine protonation triggers channel activation.<sup>39</sup> Moreover, recent NMR study on W41F also reported pK<sub>a</sub> value of 5.8 for conformational transition.<sup>25</sup> Recent FCS study of M2 proton channel dynamics observed transition centered at pK<sub>a</sub> 6.1, which is a higher pK<sub>a</sub> value.<sup>23</sup>

In the case of amantadine bound form, the  $pK_a$  was almost the same. Because amantadine and rimantadine are known to bind to M2 channel pore and inhibit conductance, protonation of His37 tetrad can be expected to be suppressed with those drugs. Indeed, Cross and coworkers observed that its  $pK_a$  value of first His37 protonation was lowered to  $\sim 5.4$  with 10mM amantadine.<sup>40</sup> And similar  $pK_a$  shift to 5.2 was measured from Trp fluorescence with amantadine (Figure 2.S7).<sup>22</sup> From these, it can be pointed out that the drug effectively binds to M2TM at basic and neutral pH, but, at acidic pH (below pH 6), gradually binds less tightly. Such pH-dependent binding affinity of amantadine was previously reported by electrophysiological study of M2 proton channel conductance at various pH with amantadine, showing binding constant of  $9 \pm 2 \mu\text{M}$  at pH 7.5, and  $13 \pm 2 \mu\text{M}$  at pH 6.2.<sup>41</sup>

Lower binding affinity of amantadine at acidic pH could be explained by the changes in conformation and(or) structural dynamics of M2 proton channel. In basic and neutral pH, M2 proton channel exists mostly in “closed” state, in which amantadine binds into its pore. Hydrophobic adamantane ring of amantadine interacts with the hydrophobic pore lining residues such as Val27 and Ala30, blocking channel entrance, while positively charged amino group makes water-bridged hydrogen-bonds with imidazole rings of His37 and backbone carbonyl groups of Ala30 tetrad.<sup>39</sup> Once M2 proton channel is activated, those interactions might be inhibited to some extents by more dynamic backbone fluctuation and dilated structure, in which channel is more hydrated with bulk like water. However, this does not necessarily mean that amantadine does not bind to the activated M2 proton channel at all. For example, 3C9J PDB structure shows “open” structure even with

amantadine bound to the channel pore at pH 5.3. Thus, the conductance inhibition mechanism of drugs at acidic condition needs more investigations.

Careful analysis of FRET data can allow one to back-calculate the distance between donor-acceptor pair. For calculation, specific assumptions must be made: 1) Both the acceptor and the donor labeled peptides assemble randomly into possible tetramer combinations. 2) All tetramers were simplified as being fourfold symmetric, to minimize the number of free parameters. Therefore, the two adjacent monomers will have a distance of R, while the monomer diagonal will have a distance of  $\sqrt{2}R$ .

First, FRET efficiency equation was derived for each possible geometry of donor and acceptor of tetramer. (Table 3.S1). Then, probability of each donor and acceptor combination was calculated, and the fluorescence intensity per different combination of acceptor and donor is  $FI = \#of\ donors \times (1 - FRET\ Efficiency)$ . In addition, the total FRET efficiency is

$$Total\ F.I. = \frac{\sum_{n=0}^4 n P_{D_n A_{n-4}} (1 - E_{D_n A_n}^D)}{\sum_{n=0}^4 (4 - n) P_{D_n A_{n-4}} (1 + E_{D_n A_n}^A \frac{\epsilon D}{\epsilon A})}$$

From this information, one can correlate the FRET efficiency to the mean distance between the donor and acceptors. Expected FRET efficiency was calculated as a function of ratio between donor and acceptor, and then compared with the experimental data (Figure 3.6), which shows good agreement. (Figure 3.7) This supports that M2TM forms a stable tetramer.

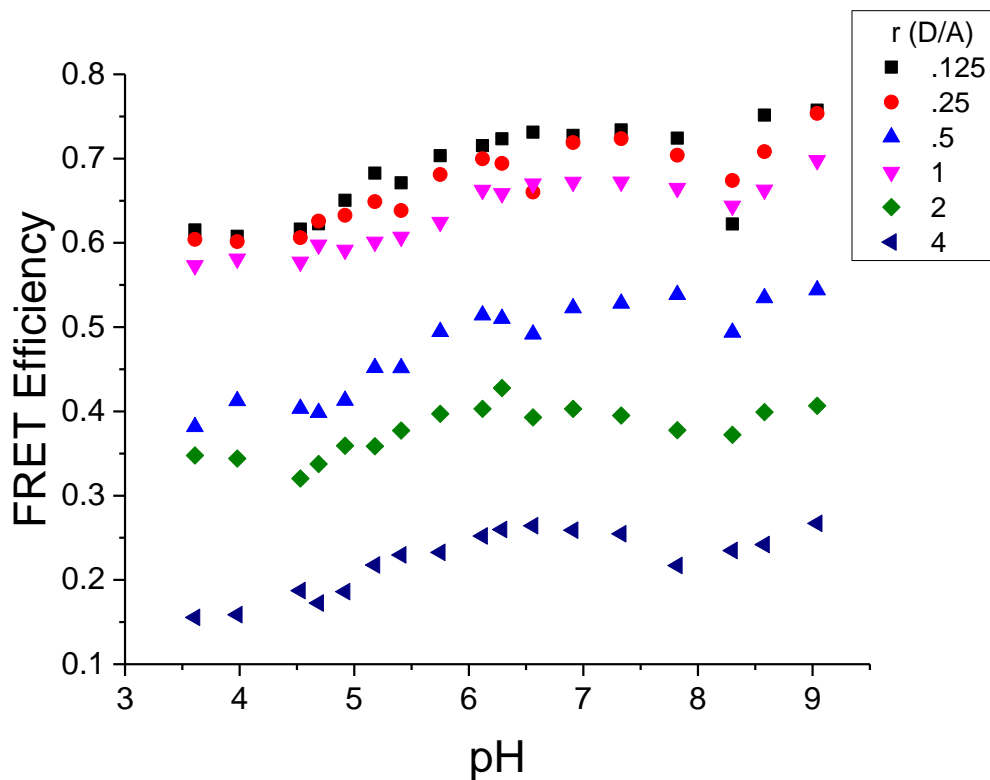


**Figure 3.6** pH-dependent FRET efficiency of samples in various ratio between donor and acceptor.

The distance between the C-terminus of the M2 proton channel was calculated to be about 4.4 nm at basic pH and 4.7 nm at acidic pH. Compared to the distance in table 3.1, which ranges from 2.3 nm to 3.6 nm, this calculated number is much longer. This can be explained by several points: (a) the distance was measured from  $\alpha$ -carbon of protein backbone. Since the dye has a linker and maleimide group, which is linked to the Cysteine. Therefore, the distance of about 1~2 nm can be added for this. (b) M2TM tetramer can form multiple conformations, but what we observe is only an averaged value. (c) If M2TM is in dynamic fluctuation, we can also only measure the averaged value.

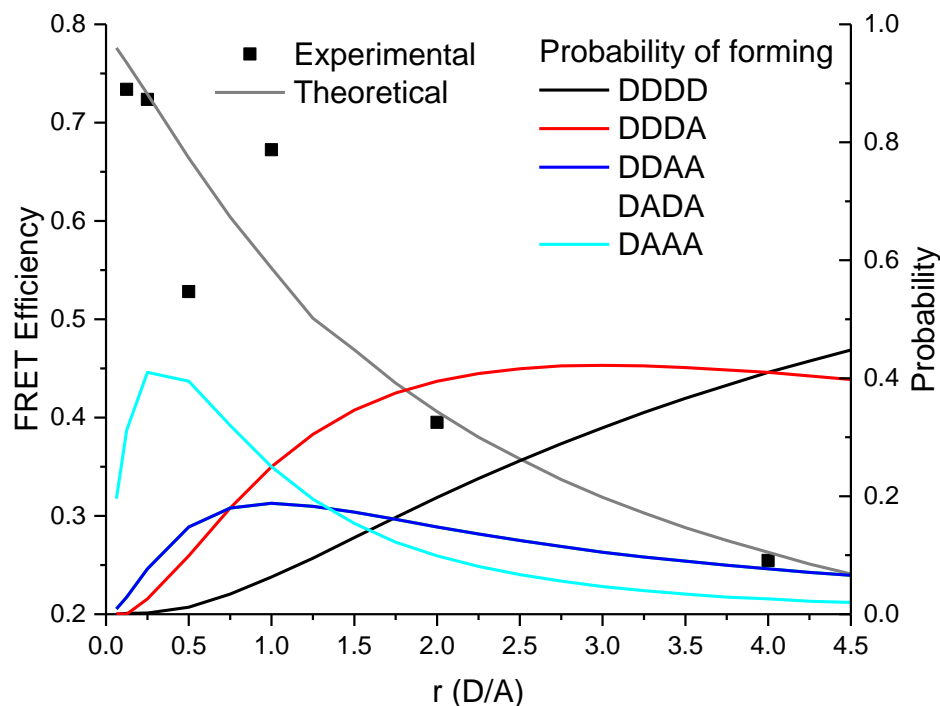


**Figure 3.7** Simulated FRET efficiency, and probability of formation of each tetramer of donor and acceptor combinations. Experimental data was obtained at pH 7.

### 3.6 Conclusion

The FRET experiment revealed that M2TM undergoes conformational transition as a function of pH. This result supports the notion that M2 proton channel conformation change is closely related to its activation, implying its role for proton conductance. However, in this steady state ensemble measurement, one can only observe the averaged value. This can be overcome by single molecule experiments, especially where individual multiple sub-state and their population weight can be resolved. Moreover, pH-jump experiment could elucidate its conformation change kinetics; further confirming previous Trp fluorescence experiment. In order to conduct single molecule experiment, FRET pair



should be improved; EDANS absorbs in the UV region and DABCYL<sup>+</sup> is non-fluorescent quencher. Donor absorbing and fluorescing in visible light region, and fluorescent acceptor with short Förster radius can be an ideal FRET pair.

### 3.7 Appendix

#### (a)ESI Mass Spectra

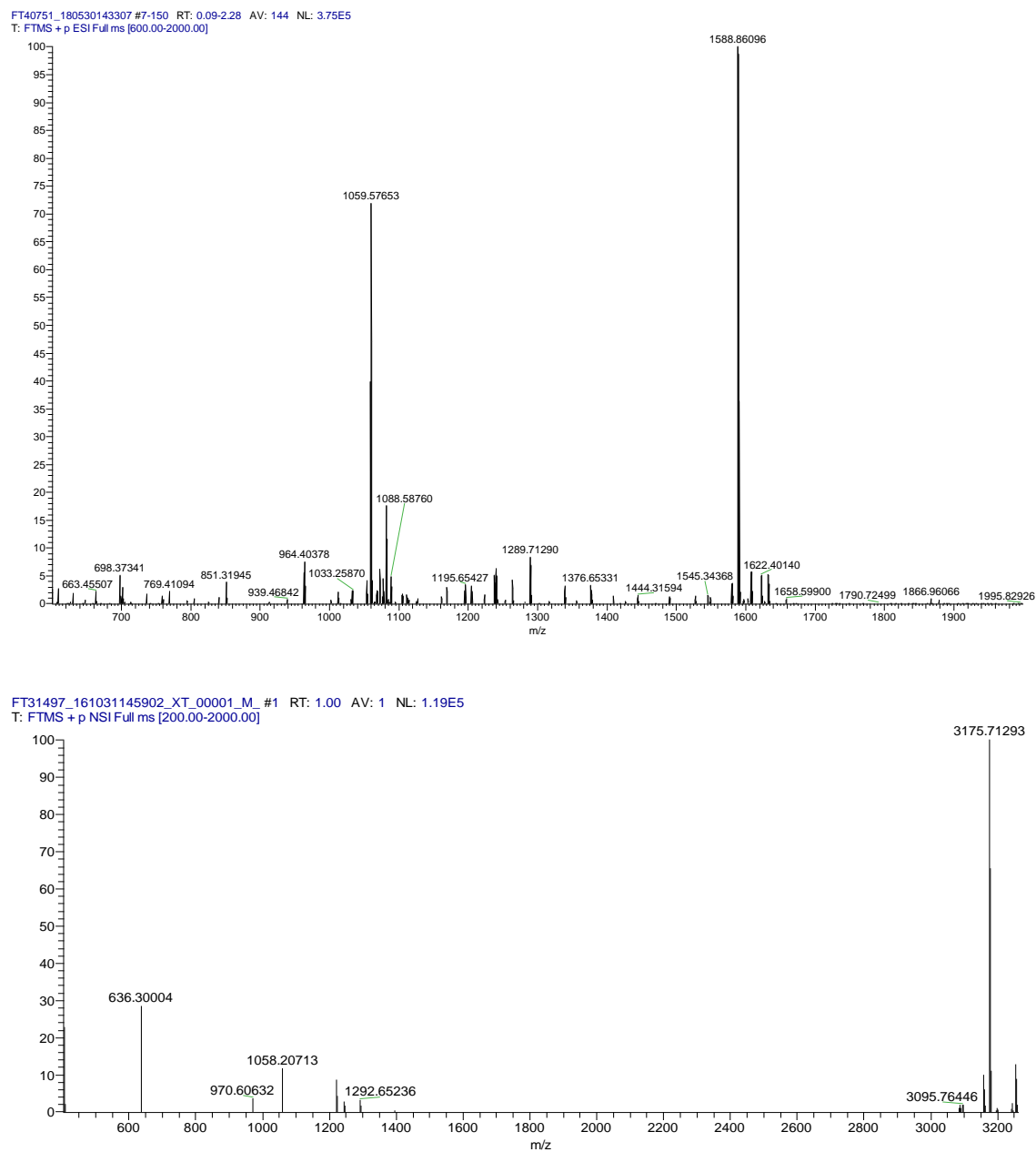
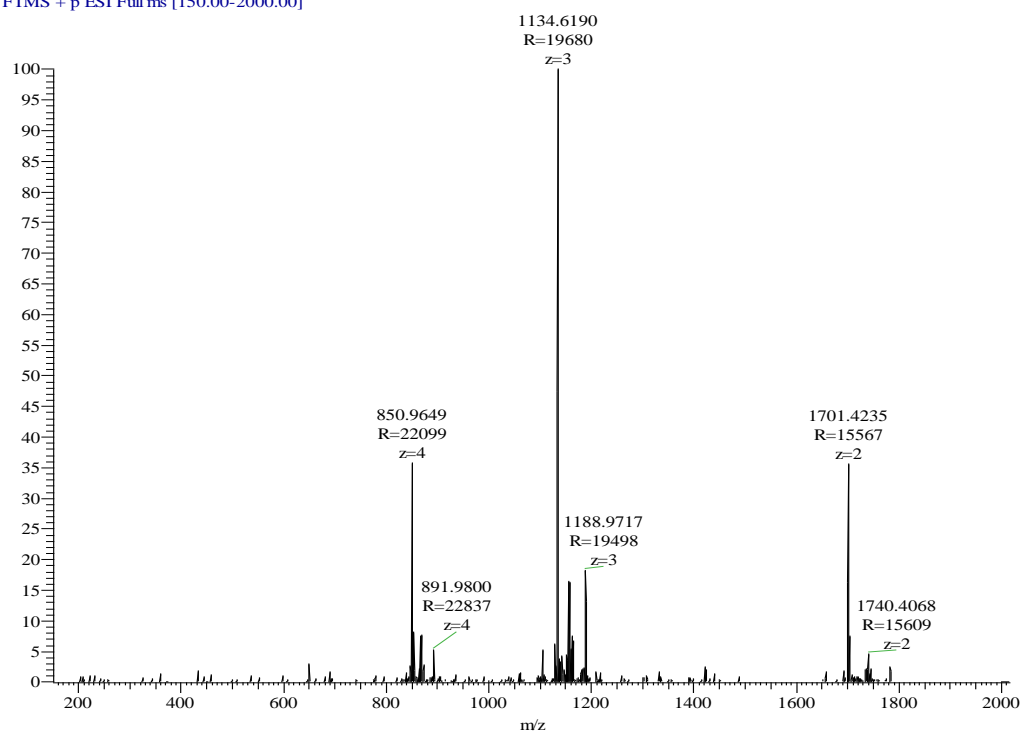
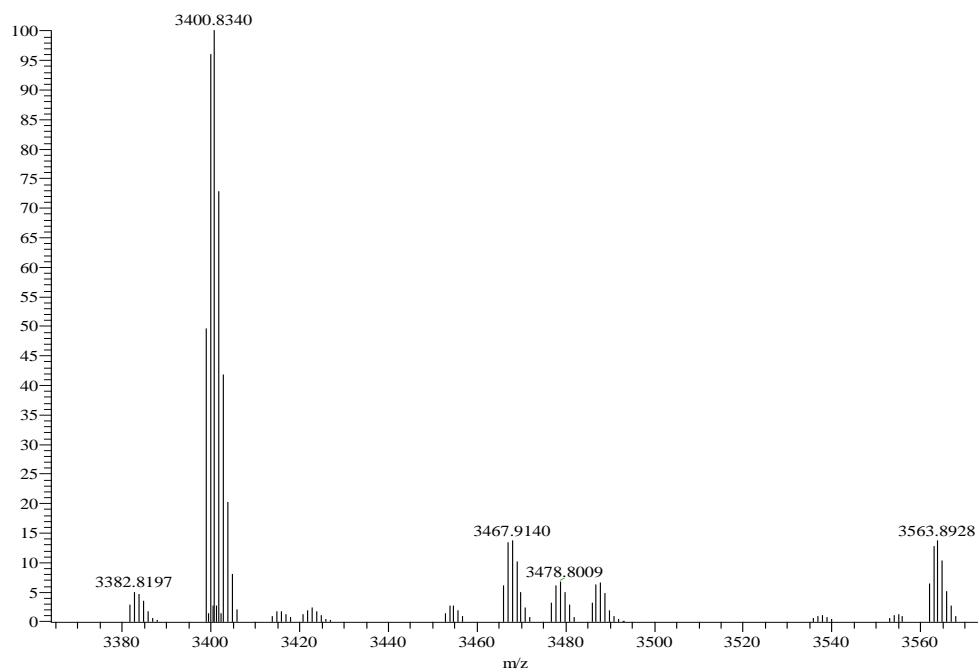


Figure 3.S1. ESI mass spectra of M2TM-EDANS.

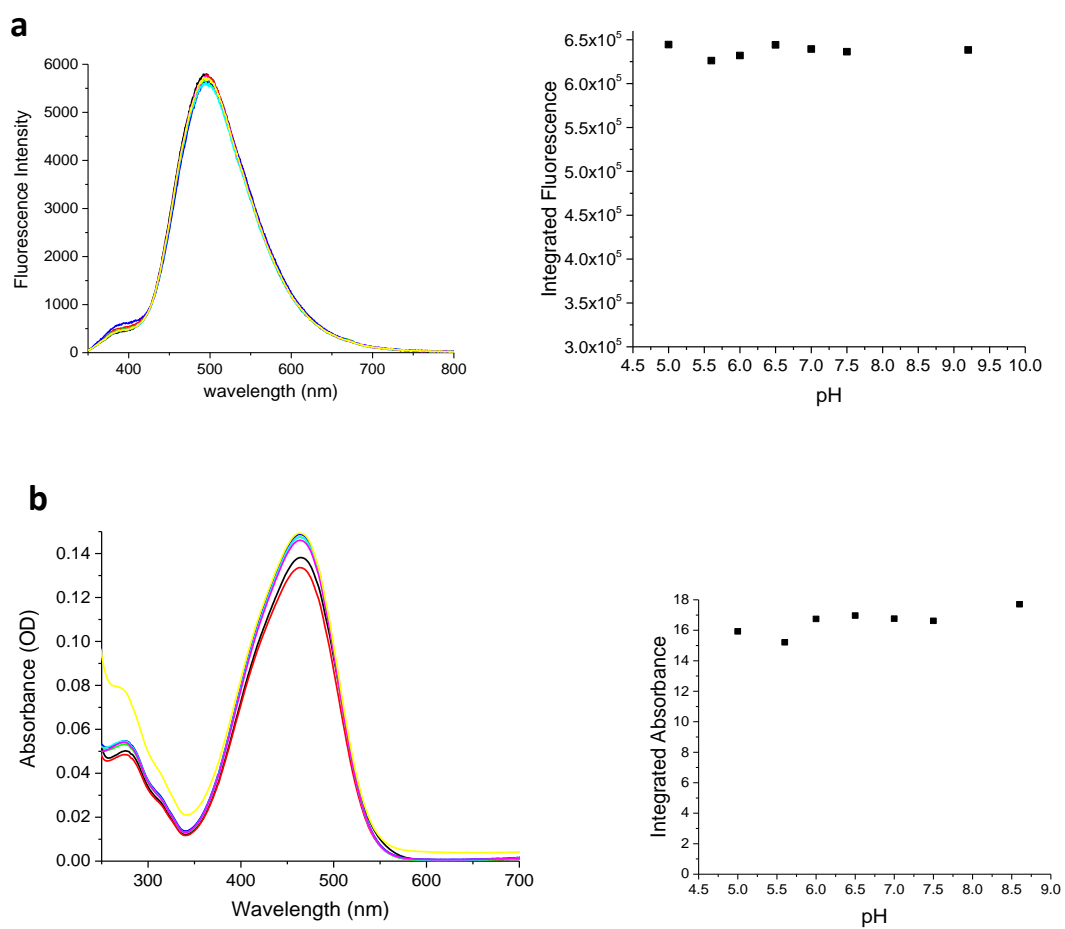
eu180611-03 #103-121 RT: 0.81-0.95 AV: 19 NL: 2.32E7  
T: FTMS + p ESI Full ms [150.00-2000.00]



eu180611-03\_XT\_00001\_M\_#1 RT: 1.00 AV: 1 NL: 1.40E7  
T: FTMS + p ESI Full ms [150.00-2000.00]

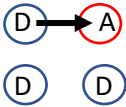
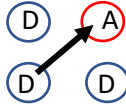
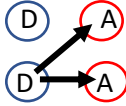
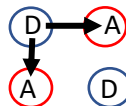
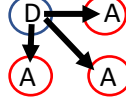


**Figure 3.S2.** ESI mass spectra of M2TM-DABCYL<sup>+</sup>.

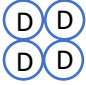
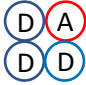
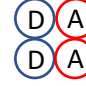


**(b) pH dependence of EDANS and DABCYL<sup>+</sup>.**

**Figure 3.S3.** (a) Fluorescence spectra of EDANS and (b) Absorbance spectra of DABCYL<sup>+</sup> in various pH buffer

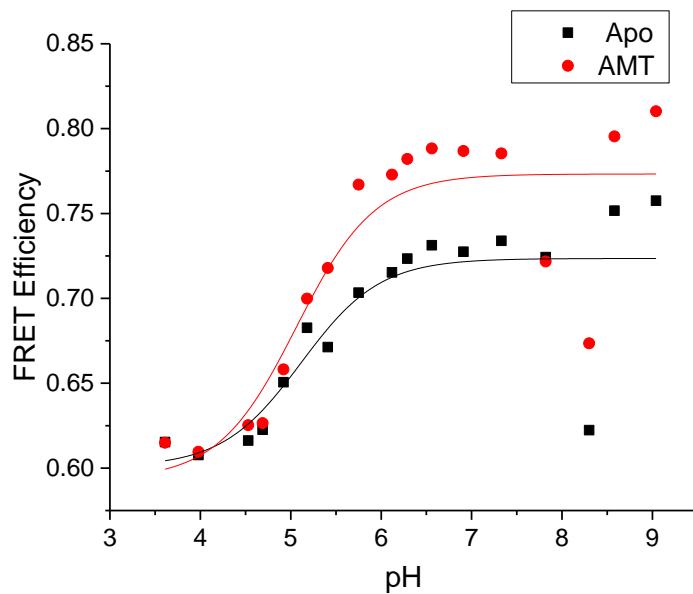
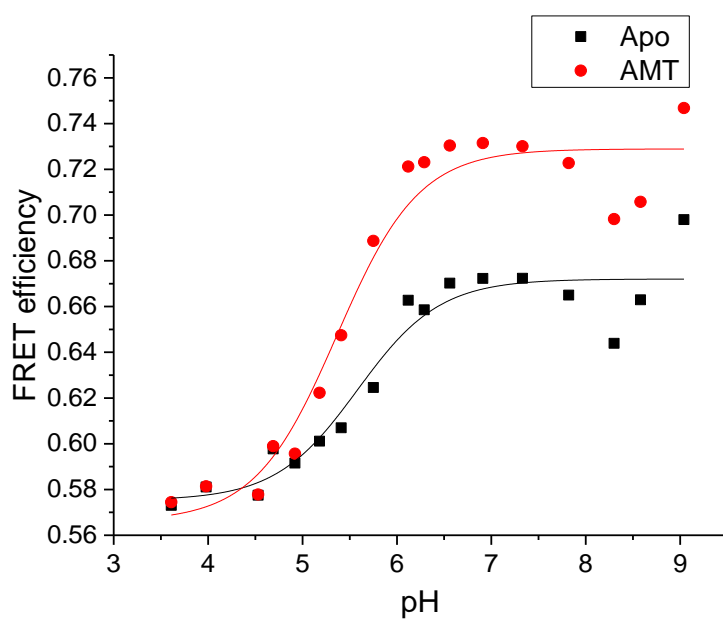
## (c) FRET Efficiency calculation

FRET Geometry	FRET Efficiency
	$E = \frac{1}{1 + \left(\frac{R}{R_0}\right)^6}$
	$E1 = \frac{E}{(8 - 7E)}$
	$E2 = \frac{E + E1 - 2EE1}{1 - EE1}$
	$E3 = \frac{2E}{1 + E}$
	$E4 = \frac{2E + E1 - 3EE1}{1 + E - 2EE1}$

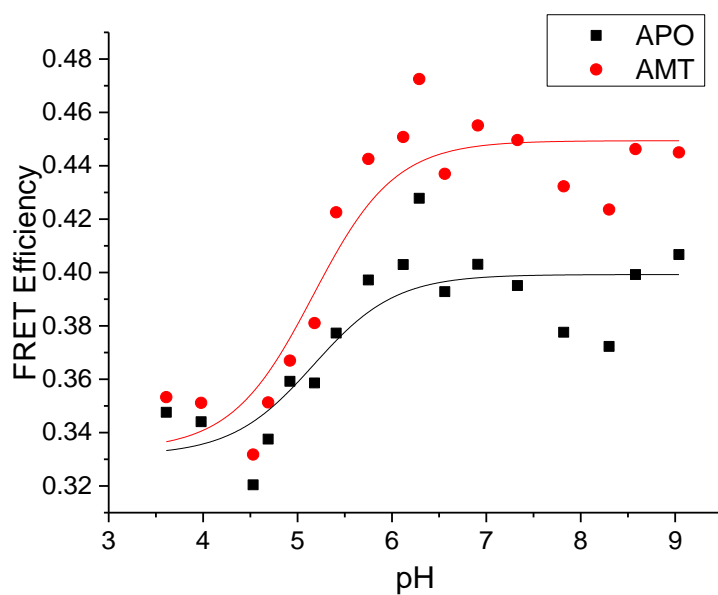
**Table 3.S1** Possible FRET geometry among donor acceptor in tetrameric configuration.

Labeling Combination	Probability	Number of Donors	FRET Efficiency
	$\frac{r^4}{(1 + r^4)}$	4	0
	$\frac{4r^3}{(1 + r^4)}$	3	$\frac{2E + E_1}{3}$
	$\frac{3r^2}{(1 + r^4)}$	2	$E_2$
	$\frac{3r^2}{(1 + r^4)}$	2	$E_3$
	$\frac{4r}{(1 + r^4)}$	1	$E_4$

**Table 3.S2** Probability of each possible combination and tis FRET efficiency

**(d) Individual pH dependent FRET efficiency graph in various ratio (D/A)****A: 0.125, pK<sub>a</sub>: 5.1 (apo) 5.1 (Amt)****B: 1, pK<sub>a</sub>: 5.6 (apo) 5.4 (Amt)**

C: 2,  $pK_a$ : 5.2 (apo) 5.2 (Amt)



D: 4,  $pK_a$ : 5.0 (apo) 5.0 (Amt)

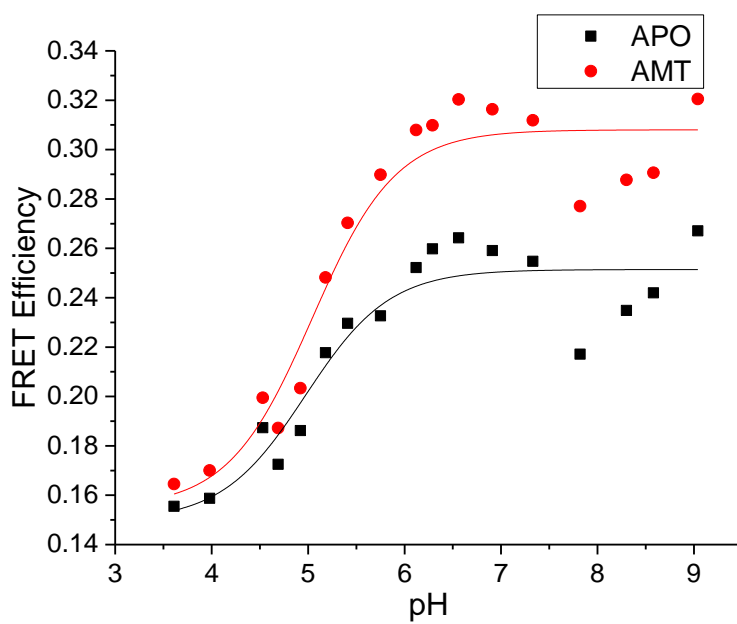


Figure 3.S4 pH-dependent FRET efficiency in ratio (a) 0.125 (b) 0.25 (c) 1 (d) 2 (e) 4.



### 3.8 References

1. Stouffer, A. L.; Acharya, R.; Salom, D.; Levine, A. S.; Di Costanzo, L.; Soto, C. S.; Tereshko, V.; Nanda, V.; Stayrook, S.; DeGrado, W. F., Structural basis for the function and inhibition of an influenza virus proton channel. *Nature* **2008**, *451* (7178), 596-9.
2. Acharya, R.; Carnevale, V.; Fiorin, G.; Levine, B. G.; Polishchuk, A. L.; Balannik, V.; Samish, I.; Lamb, R. A.; Pinto, L. H.; DeGrado, W. F.; Klein, M. L., Structure and mechanism of proton transport through the transmembrane tetrameric M2 protein bundle of the influenza A virus. *Proc. Natl. Acad. Sci. USA* **2010**, *107* (34), 15075-15080.
3. Nishimura, K.; Kim, S. G.; Zhang, L.; Cross, T. A., The closed state of a H<sup>+</sup> channel helical bundle combining precise orientational and distance restraints from solid state NMR-1. *Biochemistry* **2002**, *41* (44), 13170-13177.
4. Hong, M.; DeGrado, W. F., Structural basis for proton conduction and inhibition by the influenza M2 protein. *Protein Sci* **2012**, *21* (11), 1620-33.
5. Jiang, L.; Wang, L.; Guo, M.; Yin, G.; Wang, R. Y., Fluorescence turn-on of easily prepared fluorescein derivatives by zinc cation in water and living cells. *Sensor Actuat B-Chem* **2011**, *156* (2), 825-831.
6. Liang, R. B.; Li, H.; Swanson, J. M. J.; Voth, G. A., Multiscale simulation reveals a multifaceted mechanism of proton permeation through the influenza A M2 proton channel. *Proc. Natl. Acad. Sci. USA* **2014**, *111* (26), 9396-9401.

7. Liang, R.; Swanson, J. M.; Madsen, J. J.; Hong, M.; DeGrado, W. F.; Voth, G. A., Acid activation mechanism of the influenza A M2 proton channel. *Proc Natl Acad Sci U S A* **2016**.
8. Wei, C. Y.; Pohorille, A., Activation and Proton Transport Mechanism in Influenza A M2 Channel. *Biophys. J.* **2013**, *105* (9), 2036-2045.
9. Schnell, J. R.; Chou, J. J., Structure and mechanism of the M2 proton channel of influenza A virus. *Nature* **2008**, *451* (7178), 591-U12.
10. Cady, S. D.; Mishanina, T. V.; Hong, M., Structure of Amantadine-Bound M2 Transmembrane Peptide of Influenza A in Lipid Bilayers from Magic-Angle-Spinning Solid-State NMR: The Role of Ser31 in Amantadine Binding. *J. Mol. Biol.* **2009**, *385* (4), 1127-1141.
11. Stouffer, A. L.; Acharya, R.; Salom, D.; Levine, A. S.; Di Costanzo, L.; Soto, C. S.; Tereshko, V.; Nanda, V.; Stayrook, S.; DeGrado, W. F., Structural basis for the function and inhibition of an influenza virus proton channel. *Nature* **2008**, *451* (7178), 596-U13.
12. Cady, S. D.; Schmidt-Rohr, K.; Wang, J.; Soto, C. S.; DeGrado, W. F.; Hong, M., Structure of the amantadine binding site of influenza M2 proton channels in lipid bilayers. *Nature* **2010**, *463* (7281), 689-U127.
13. Sharma, M.; Yi, M. G.; Dong, H.; Qin, H. J.; Peterson, E.; Busath, D. D.; Zhou, H. X.; Cross, T. A., Insight into the Mechanism of the Influenza A Proton Channel from a Structure in a Lipid Bilayer. *Science* **2010**, *330* (6003), 509-512.

14. Hu, J.; Asbury, T.; Achuthan, S.; Li, C. G.; Bertram, R.; Quine, J. R.; Fu, R. Q.; Cross, T. A., Backbone structure of the amantadine-blocked trans-membrane domain M2 proton channel from influenza A virus. *Biophys. J.* **2007**, *92* (12), 4335-4343.
15. Zhou, H. X.; Cross, T. A., Influences of membrane mimetic environments on membrane protein structures. *Annu Rev Biophys* **2013**, *42*, 361-92.
16. Thomaston, J. L.; Alfonso-Prieto, M.; Woldeyes, R. A.; Fraser, J. S.; Klein, M. L.; Fiorin, G.; DeGrado, W. F., High-resolution structures of the M2 channel from influenza A virus reveal dynamic pathways for proton stabilization and transduction. *Proc Natl Acad Sci U S A* **2015**, *112* (46), 14260-5.
17. Thomaston, J. L.; Woldeyes, R. A.; Nakane, T.; Yamashita, A.; Tanaka, T.; Koiwai, K.; Brewster, A. S.; Barad, B. A.; Chen, Y.; Lemmin, T.; Uervirojnangkoorn, M.; Arima, T.; Kobayashi, J.; Masuda, T.; Suzuki, M.; Sugahara, M.; Sauter, N. K.; Tanaka, R.; Nureki, O.; Tono, K.; Joti, Y.; Nango, E.; Iwata, S.; Yumoto, F.; Fraser, J. S.; DeGrado, W. F., XFEL structures of the influenza M2 proton channel: Room temperature water networks and insights into proton conduction. *Proc Natl Acad Sci U S A* **2017**, *114* (51), 13357-13362.
18. Nguyen, P. A.; Soto, C. S.; Polishchuk, A.; Caputo, G. A.; Tatko, C. D.; Ma, C.; Ohigashi, Y.; Pinto, L. H.; DeGrado, W. F.; Howard, K. P., pH-induced conformational change of the influenza M2 protein C-terminal domain. *Biochemistry* **2008**, *47* (38), 9934-6.
19. Ghosh, A.; Qiu, J.; DeGrado, W. F.; Hochstrasser, R. M., Tidal surge in the M2 proton channel, sensed by 2D IR spectroscopy. *Proc Natl Acad Sci U S A* **2011**, *108* (15), 6115-20.

20. Liang, R.; Li, H.; Swanson, J. M.; Voth, G. A., Multiscale simulation reveals a multifaceted mechanism of proton permeation through the influenza A M2 proton channel. *Proc Natl Acad Sci U S A* **2014**, *111* (26), 9396-401.
21. Luo, W.; Hong, M., Conformational Changes of an Ion Channel Detected Through Water-Protein Interactions Using Solid-State NMR Spectroscopy. *J. Am. Chem. Soc.* **2010**, *132* (7), 2378-2384.
22. Jeong, B. S.; Dyer, R. B., Proton Transport Mechanism of M2 Proton Channel Studied by Laser-Induced pH Jump. *J Am Chem Soc* **2017**, *139* (19), 6621-6628.
23. Lin, C. W.; Mensa, B.; Barniol-Xicota, M.; DeGrado, W. F.; Gai, F., Activation pH and Gating Dynamics of Influenza A M2 Proton Channel Revealed by Single-Molecule Spectroscopy. *Angew Chem Int Ed Engl* **2017**, *56* (19), 5283-5287.
24. Markiewicz, B. N.; Lemmin, T.; Zhang, W.; Ahmed, I. A.; Jo, H.; Fiorin, G.; Troxler, T.; DeGrado, W. F.; Gai, F., Infrared and fluorescence assessment of the hydration status of the tryptophan gate in the influenza A M2 proton channel. *Phys Chem Chem Phys* **2016**, *18* (41), 28939-28950.
25. Mandala, V. S.; Gelenter, M. D.; Hong, M., Transport-Relevant Protein Conformational Dynamics and Water Dynamics on Multiple Time Scales in an Archetypal Proton Channel: Insights from Solid-State NMR. *J Am Chem Soc* **2018**, *140* (4), 1514-1524.
26. Hu, F.; Luo, W.; Cady, S. D.; Hong, M., Conformational plasticity of the influenza A M2 transmembrane helix in lipid bilayers under varying pH, drug binding, and membrane thickness. *Biochim Biophys Acta* **2011**, *1808* (1), 415-23.

27. Kochendoerfer, G. G.; Salom, D.; Lear, J. D.; Wilk-Orescan, R.; Kent, S. B. H.; DeGrado, W. F., Total chemical synthesis of the integral membrane protein influenza A virus M2: Role of its C-terminal domain in tetramer assembly. *Biochemistry* **1999**, *38* (37), 11905-11913.
28. Georgieva, E. R.; Borbat, P. P.; Norman, H. D.; Freed, J. H., Mechanism of influenza A M2 transmembrane domain assembly in lipid membranes. *Sci Rep* **2015**, *5*, 11757.
29. Cristian, L.; Lear, J. D.; DeGrado, W. F., Use of thiol-disulfide equilibria to measure the energetics of assembly of transmembrane helices in phospholipid bilayers. *Proc. Natl. Acad. Sci. USA* **2003**, *100* (25), 14772-14777.
30. Salom, D.; Hill, B. R.; Lear, J. D.; DeGrado, W. F., pH-dependent tetramerization and amantadine binding of the transmembrane helix of M2 from the influenza A virus. *Biochemistry* **2000**, *39* (46), 14160-70.
31. Thomaston, J. L.; Nguyen, P. A.; Brown, E. C.; Upshur, M. A.; Wang, J.; DeGrado, W. F.; Howard, K. P., Detection of drug-induced conformational change of a transmembrane protein in lipid bilayers using site-directed spin labeling. *Protein Sci.* **2013**, *22* (1), 65-73.
32. Salom, D.; Hill, B. R.; Lear, J. D.; DeGrado, W. F., pH-dependent tetramerization and amantadine binding of the transmembrane helix of M2 from the influenza A virus. *Biochemistry* **2000**, *39* (46), 14160-14170.
33. Hu, J.; Fu, R.; Nishimura, K.; Zhang, L.; Zhou, H. X.; Busath, D. D.; Vijayvergiya, V.; Cross, T. A., Histidines, heart of the hydrogen ion channel from

influenza A virus: Toward an understanding of conductance and proton selectivity. *Proc. Natl. Acad. Sci. USA* **2006**, *103* (18), 6865-6870.

34. Hu, F. H.; Schmidt-Rohr, K.; Hong, M., NMR Detection of pH-Dependent Histidine-Water Proton Exchange Reveals the Conduction Mechanism of a Transmembrane Proton Channel. *J. Am. Chem. Soc.* **2012**, *134* (8), 3703-3713.

35. Liao, S. Y.; Yang, Y.; Tietze, D.; Hong, M., The influenza m2 cytoplasmic tail changes the proton-exchange equilibria and the backbone conformation of the transmembrane histidine residue to facilitate proton conduction. *J. Am. Chem. Soc.* **2015**, *137* (18), 6067-77.

36. Colvin, M. T.; Andreas, L. B.; Chou, J. J.; Griffin, R. G., Proton association constants of His 37 in the Influenza-A M218-60 dimer-of-dimers. *Biochemistry* **2014**, *53* (38), 5987-94.

37. Gosavi, P. M.; Moroz, Y. S.; Korendovych, I. V., beta-(1-Azulenyl)-L-alanine--a functional probe for determination of pKa of histidine residues. *Chem Commun (Camb)* **2015**, *51* (25), 5347-50.

38. Okada, A.; Miura, T.; Takeuchi, H., Protonation of histidine and histidine-tryptophan interaction in the activation of the M2 ion channel from influenza A virus. *Biochemistry* **2001**, *40* (20), 6053-6060.

39. Hong, M.; DeGrado, W. F., Structural basis for proton conduction and inhibition by the influenza M2 protein. *Protein Sci.* **2012**, *21* (11), 1620-1633.

40. Hu, J.; Fu, R.; Cross, T. A., The chemical and dynamical influence of the anti-viral drug amantadine on the M2 proton channel transmembrane domain. *Biophys. J.* **2007**, *93* (1), 276-83.

41. Wang, C.; Takeuchi, K.; Pinto, L. H.; Lamb, R. A., Ion channel activity of influenza A virus M2 protein: characterization of the amantadine block. *J Virol* **1993**, *67* (9), 5585-94.

## **Chapter 4: Synthesis and Characterization of Water-soluble Long-lived Reversible Photoacid and Its Application to pH-jump Experiment**

### **4.1 Abstract**

When 1-(2-Nitro-ethyl)-naphthalen-2-ol is excited, proton is released in sub-ns time scale, and then intramolecular proton transfer from  $\alpha$ -carbon of nitro-group to naphtholate stabilizes its anion state. It has the desirable characteristics for the ideal candidate for proton cage of kinetics experiments, but the extremely low water solubility impeded its application. To address this flaw, hydrophilic long-lived reversible photo-acid was designed to add a sulfonate group to position 6 of the 2-naphthol ring. Although synthesis was successful, decreased  $pK_a$  of naphthol prevented intramolecular proton transfer, not allowing it to be long-lived.

### **4.2 Introduction**

Proton plays important roles in various biochemical processes and the proton gradient is the central concept of bioenergetics.<sup>1</sup> The structure and activity of many proteins can be affected by proton concentration. For instance, dramatic conformation changes of viral fusion proteins are triggered by high proton concentrations of lysosomes to fuse the viral membrane with host membrane.<sup>2</sup>

To study mechanisms and kinetics of these processes, pH jump technique could be used, where pH of sample is rapidly changed, and the subsequent processes are observed. Rapid



mixers could initiate the pH jump, but few millisecond of time resolution from mixing dead time limits this approach; proton transfer takes place in sub-millisecond timescale. Proton transfer reaction is considered as diffusion controlled, and its diffusion rate is faster than other cations like  $\text{Na}^+$  due to the Grotthuss mechanism.<sup>3</sup> To observe this rapid process, a sharp trigger is required, and laser pH jump technique could complete the pH change within a few ns.<sup>4</sup>

Reversible photo-acids, naphthol derivatives or 8-hydroxypyrene-1,3,6-trisulfonic acid (HPTS), exhibit excited state proton transfer (ESPT), in which the photo-acid excited by the pump laser pulse releases a proton in few hundreds ps, thus allowing rapid protonation kinetics of various ionizable residues to be investigated. For example, when HPTS is excited, its  $\text{pK}_a^{\text{ground}} = 7.4$  is rapidly shifted to  $\text{pK}_a^{\text{excited}} = 0.4$ , resulting in proton release within a few hundred ps.<sup>5</sup> Gutman et al could measure sub-millisecond timescale proton association and dissociation kinetics of various ionizable residues not only in homogeneous aqueous solution, but also in supramolecular structures such as protein and membrane surface.<sup>6</sup>

However, using reversible photo-acids, pH-jump has a limitation in terms of the time window; excited state of reversible photo-acid only persists for a few ns, and after decaying to the ground state, released protons are recombined very rapidly from few ns to  $\mu\text{s}$ . Therefore, the slow processes which occur after protonation could hardly be observed with such a narrow spectroscopic time window.

To address this issue, irreversible photo-acids, o-nitrobenzaldehyde (o-NBA)<sup>7-8</sup> or 1-(2-nitrophenyl)ethyl sulfate (NPE-sulfate)<sup>9-10</sup>, were developed. pH-jump can last up to few seconds before protons diffuse out to the bulk solution, thus, it allows one to observe  $\mu\text{s}$  or

ms timescale processes after the pH-jump. Indeed, with irreversible photo-acid, one could observe the kinetics of many biological processes such as alpha-helix formation of poly-L-glutamate<sup>11-12</sup>, leucine zipper folding<sup>13</sup>, and acid-induced unfolding of myoglobin<sup>14</sup>.

However, in practice, this irreversibility results in severe constraint to the spectroscopic application, in that the pH-jump experiment with irreversible photo-acid must be a single-shot experiment. Therefore, to improve signal-to-noise ratio (SNR), the experiment should be repeated several times, which increases the amount of sample required for the experiments. Also, the irreversible photo-acid cannot be applied to the spectroscopic techniques which require many repetitions such as 2D-IR and step-scan FT-IR.

To overcome these limitations, the new concept of long-lived reversible photo-acids were proposed. In order to combine the advantages of reversible and irreversible photo-acids, reversibility and longer spectroscopic time window were required. There have been two types of long-lived reversible photo-acids: merocyanine based<sup>15</sup> and naphthol based photo-acid<sup>16</sup>. Merocyanine type photo-acid shows excellent reversibility, but its kinetics is too slow to be a trigger of kinetics experiments.<sup>17</sup> On the other hand, naphthol based photo-acid exhibits very fast kinetics of proton release in sub-ns time scale, relatively good quantum yield of 0.3, and very low excited state pK<sub>a</sub> of 1.5, which makes this photo-acid an extraordinary candidate for kinetics experiments, 2D-IR, and step-scan FTIR.<sup>16</sup> When the photo-acid is excited, a proton is released from the hydroxyl group of naphthol, and in turn, a proton at the  $\alpha$ -carbon of the nitro group undergoes intramolecular proton transfer to protonate naphtholate, stabilizing anion state for few hundreds of ms. (Figure 4.1) However, there hasn't been any application of this long-lived reversible photo-acid to any spectroscopic technique for about 9 years. This can be mainly explained by the fact that

this compound is hydrophobic and its water solubility is quite low. In order to improve solubility, a co-solvent such as methanol or DMF was used, but the presence of small amount of cosolvent can disrupt protein and membrane structure. Also, highly hydrophobic molecules can bind to the hydrophobic patch of protein surface and induce conformational artifacts. More importantly, when a photo-acid is under hydrophobic environment, its anionic state becomes unstable, resulting in faster recombination of the released proton. This can be a severe issue with detergent and/or lipid because hydrophobic molecules partition into them.

To address these problems fundamentally, water-soluble long-lived reversible photo-acid was designed by adding a sulfate group. Also, hydrophilic photo-acid is membrane impermeable, so it can be used to generate proton gradient across membrane.

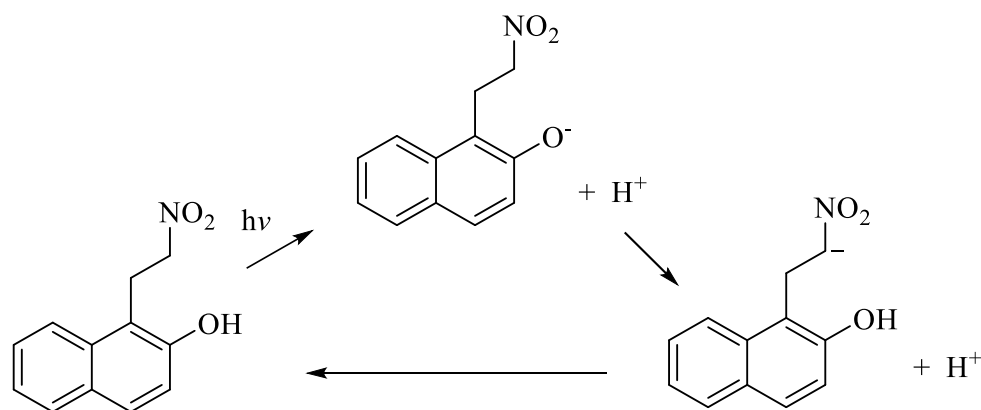


**Figure 4.1** Photo-cycle of naphthol based long-lived reversible photo-acid.

### 4.3 Experimental

**Materials.** 2-hydroxy-1-naphthaldehyde, pyrrolidine, nitromethane, and sodium borohydride were purchased from Aldrich. 5-formyl-6-hydroxynaphthalene-2-sulfonate was synthesized as described.<sup>18</sup> <sup>1</sup>H NMR and <sup>13</sup>C NMR were measured on a Varian INOVA 400 MHz NMR spectrometer. UV-vis and fluorescence spectra were recorded on Jobin Yvon Dual Fluorometer. ESI Mass spectroscopy was recorded on Thermo LTQ-FTMS.

**Sodium 6-hydroxy-5-(2-nitrovinyl)naphthalene-2-sulfonate.** Sodium 5-formyl-6-hydroxynaphthalene-2-sulfonate (546 mg, 1.99 mmol) and methanol (50 ml) were added into a one-neck round bottom flask and stirred at RT. Into the solution, nitromethane (0.256 ml, 292 mg, 4.78 mmol) was added. Then, pyrrolidine (0.278 ml, 240 mg, 3.38 mmol) was slowly added, and the color of reaction mixture was changed to yellow, and subsequently to the dark red. Stirring was maintained for three days, and HCl was added to adjust pH to neutral, resulting in dark yellow solution. The methanol was removed under reduced pressure, and the resulting residue was purified by flash chromatography (SiO<sub>2</sub>) with CH<sub>2</sub>Cl<sub>2</sub>/MeOH (70:30 v/v). Then, counter ion was exchanged from pyrrolidine to sodium by ion-exchange column (Amberlite® IR120 Na<sup>+</sup> form) in MeOH, yielding 132 mg (21%) of yellowish solid. <sup>1</sup>H NMR (D<sub>2</sub>O, 400 MHz):  $\delta$  (ppm) = 6.20(d, 1H,  $J$  = 8.8 Hz), 7.01(d, 1H,  $J$  = 8.8 Hz), 7.16(d, 1H,  $J$  = 8.8 Hz), 7.37 (dd, 1H,  $J$  = 8.8, 1.6 Hz), 7.43(d, 1H,  $J$  = 13.2Hz), 7.58(d, 1H,  $J$  = 13.2 Hz), 7.58(s, 1H). <sup>13</sup>C NMR (D<sub>2</sub>O, 400 MHz):  $\delta$  (ppm) = 107.9, 117.9, 122.0, 123.5, 126.1, 126.5, 131.7, 133.4, 134.8, 137.1, 137.8, 158.8.

**Sodium 6-hydroxy-5-(2-nitroethyl)naphthalene-2-sulfonate (HNNS).** Sodium 6-hydroxy-5-(2-nitrovinyl)naphthalene-2-sulfonate (100 mg, 0.315 mmol) was added to methanol (50 ml), and stirred at 0 °C. Into the solution, sodium borohydride (0.1 g, 2.6 mmol) was added in portions, and the reaction mixture was stirred until the color of reaction mixture becomes transparent. To quench the reaction, pH was adjusted to neutral by adding HCl solution slowly at 0 °C. Solvents are removed under reduced pressure, and the product was purified by flash chromatography with CH<sub>2</sub>Cl<sub>2</sub>/MeOH (70:30 v/v) to obtain 78 mg (78%) of white solid. <sup>1</sup>H NMR (D<sub>2</sub>O, 400 MHz): δ (ppm) = 3.09 (t, 1H, *J* = 7.6 Hz), 4.23(t, 1H, *J* = 7.6 Hz), 6.67(d, 1H, *J* = 8.8 Hz), 7.22(d, 1H, *J* = 8.8 Hz), 7.46(d, 1H, *J* = 8.8 Hz), 7.67(d, 1H, *J* = 8.8 Hz), 7.84(s, 1H). <sup>13</sup>C NMR (D<sub>2</sub>O, 400 MHz): δ (ppm) = 22.7, 73.9, 113.3, 118.2, 122.5, 122.7, 126.2, 126.9, 129.7, 133.3, 136.5, 153.2. ESI-MS (negative ion mode): expected *m/z* = 296.02, observed *m/z* = 296.02

**Laser pH-jump Kinetics Experiment.** The 4<sup>th</sup> harmonics pulse (266 nm, 10 ns) from a Q-switched Nd:YAG laser (Quanta-ray GCR IV, Spectra Physics) was focus to a horizontal line by passing through cylindrical lens. The probe beam was 550 nm diode laser, which passed though a 10 mm path of 2 × 10 mm cuvette, nearby the face of cuvette toward pump beam. The transmitted probe beam intensity was measured by avalanche silicon photodiode, and the signal was digitized by digital oscilloscope. The sample contained 10 μM of bromocresol green (*pK<sub>a</sub>* = 4.9) and its pH-dependent absorbance change was probed to study kinetics of the long-lived reversible photo-acid.

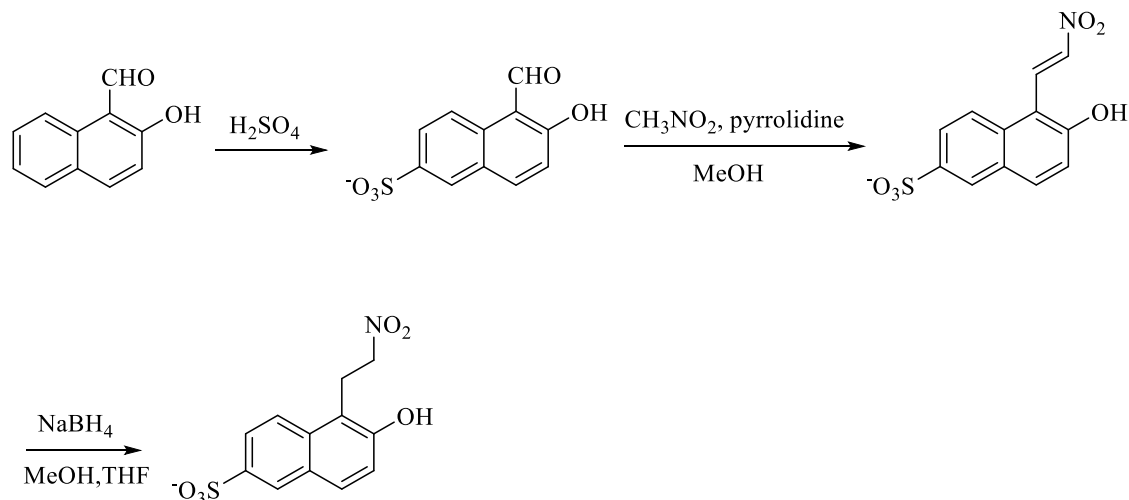


**Figure 4.2** Synthetic scheme of 6-hydroxy-5-(2-nitroethyl)naphthalene-2-sulfonate.

#### 4.4 Result and discussion

##### The Synthesis of 6-hydroxy-5-(2-nitroethyl)naphthalene-2-sulfonate

The synthetic condition was optimized from previous method using L-proline as catalyst.<sup>16</sup> The experimental conditions worked well for benzaldehyde, but not for naphthaldehyde, where almost no product was produced. With a primary amine such as acetic acid/ammonium acetate as a catalyst, too many side products were observed. The reaction yield was improved by replacing ammonium acetate with pyrrolidine.<sup>19</sup> The best yield was obtained by further optimization of the catalyst: no acetic acid, but only pyrrolidine. However, purification of highly polar product was difficult, lowering the final yield of the compound. In the last step, the reduction of vinyl group was relatively straightforward reaction with NaBH<sub>4</sub> in MeOH/THF, but, after quenching reaction with HCl solution, the resulting boric acid was hard to remove because both boric acid and the product are water-soluble. This could be a potential problem because boric acid acts as a buffer, which can

hinder pH-jump experiment at high concentration. Fortunately,  $pK_a$  of boric acid is 9.24, therefore, below pH 7.5, its impact might be negligible.

### Steady-State Spectrum

The UV-Vis spectrum was very similar to that of 6-sulfonate-2-naphthol at neutral pH, confirming the presence of sulfonate functional group.(Figure 4.3) The 1-nitroethyl functional group doesn't have a large effect on the absorbance spectra. Compared to non-sulfonated 2-naphthol, the UV-Vis absorbance is blue-shifted due to electron-withdrawing sulfonate group. Due to blue-shifted absorbance spectra, 3<sup>rd</sup> harmonic of Nd:YAG (355 nm) cannot be used, but 4<sup>th</sup> harmonic (266 nm) was used to excite the photo-acid.

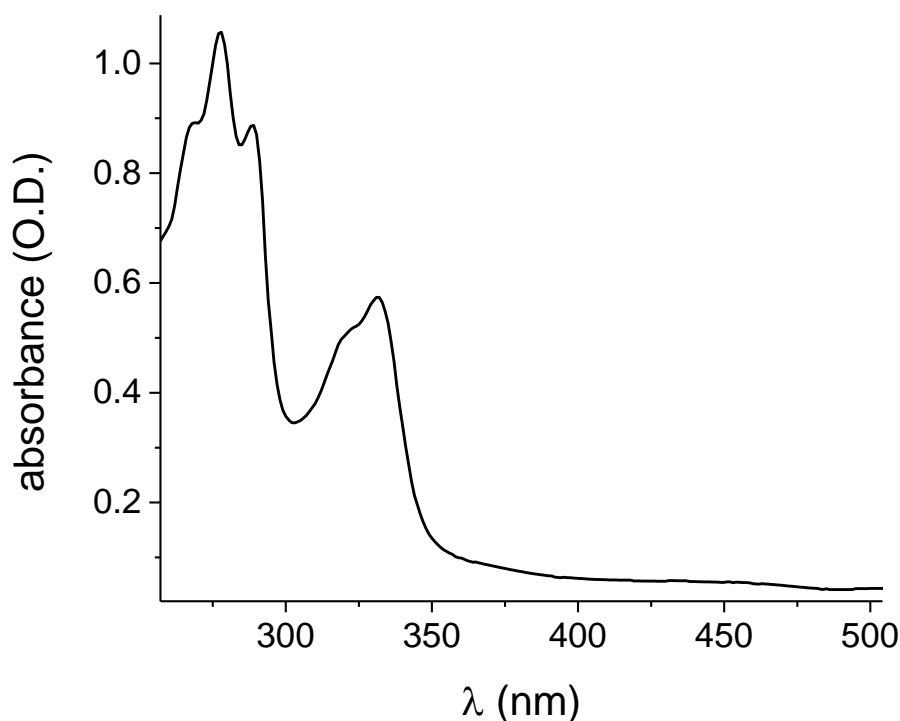


**Figure 4.3** UV-Vis spectrum of 6-hydroxy-5-(2-nitroethyl)naphthalene-2-sulfonate at pH 7.0.

### pH-jump Kinetics Experiment

Compared to 1-(2-Nitro-ethyl)-naphthalen-2-ol, 6-hydroxy-5-(2-nitroethyl)naphthalene-2-sulfonate was readily soluble in water, thus, high concentrations of the solution could be prepared, which allows large pH-jump.

After excitation of photo-acid by 266 nm pulse, the pH of the solution was observed by absorbance change of bromocresol green. It was expected to see rapid acidification of solution, and then, slow proton recombination kinetics in the hundreds of ms time scale. However, its kinetic trace showed fast recombination of the released proton. (Figure 4.4) Its behavior is very similar to the typical reversible photo-acid like 6-sulfonated-2-naphthol.

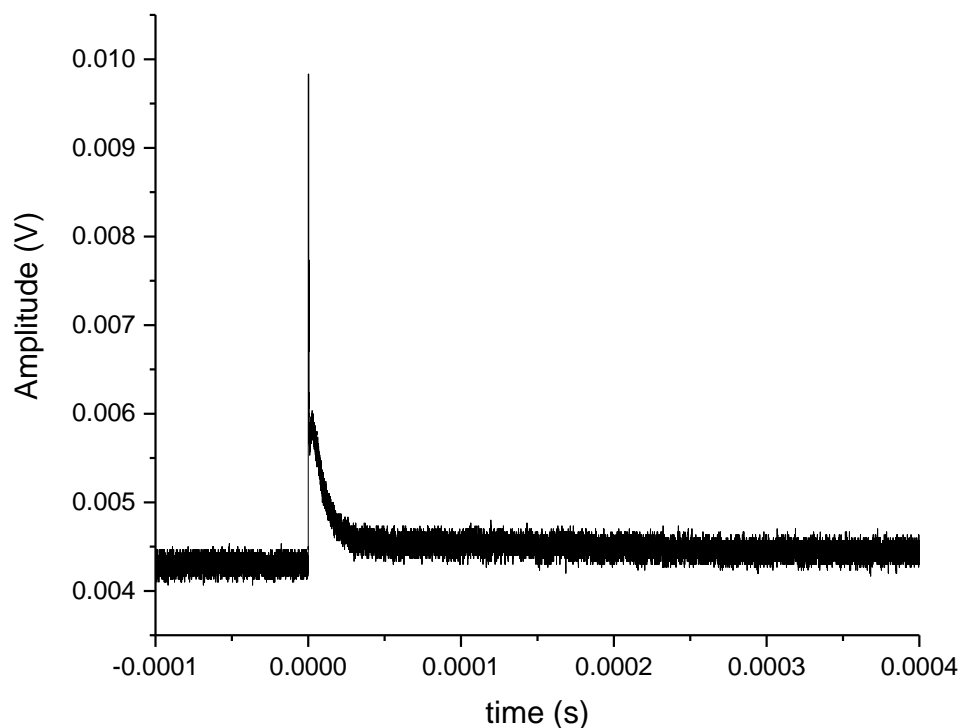


**Figure 4.4** UV-Vis spectra of 6-hydroxy-5-(2-nitroethyl)naphthalene-2-sulfonate at pH 7.0.



The most plausible explanation might be the pK<sub>a</sub> shift of sulfonated naphthol. Ground state pK<sub>a</sub> of 2-naphthol is 9.45 while excited state pK<sub>a</sub> is 2.0. When it is excited, a proton is released, and, in turn, after relaxation to the ground state, pK<sub>a</sub> of hydroxyl group returns to 9.45, which is more basic than pK<sub>a</sub> 8.78 of nearby 2-nitro-ethyl. This pK<sub>a</sub> difference is the driving force of intramolecular proton transfer; proton transfer from acidic to basic functional groups.

On the contrary, after sulfonation, both ground state and excited state pK<sub>a</sub> values are decreased to 9.0 and 1.7, respectively. When naphthol relaxed back to the ground state, pK<sub>a</sub> 9 and 8.78 might be too close to drive proton transfer between them. Smaller  $\Delta pK_a$  might be the culprit of this fast recombination.

#### 4.5 Conclusion

The molecular engineering of 1-(2-Nitro-ethyl)-naphthalen-2-ol, hydrophilic photo-acid was achieved by adding sulfonate group to 6 position of 2-naphthol to confer improved hydrophilicity. However, the designed compound, 6-hydroxy-5-(2-nitroethyl)naphthalene-2-sulfonate, didn't exhibit a characteristics of long-lived reversible photo-acid. An addition of sulfonate functional group changed not only hydrophilicity, but also electron density of naphthol ring, resulting in more acidic pK<sub>a</sub> of hydroxyl group. Negligible pK<sub>a</sub> difference between naphthol hydroxyl group and  $\alpha$ -carbon of nitro group effectively shuts down intramolecular proton transfer. This demonstrated the difficulty in engineering the molecular structure to obtain a desired property because even small adjustments can cause

unexpected changes in different properties. Although this trial was not successful, this can be a valuable lesson for better molecular design in the future.

## 4.6 Appendix

### (a) NMR spectrum

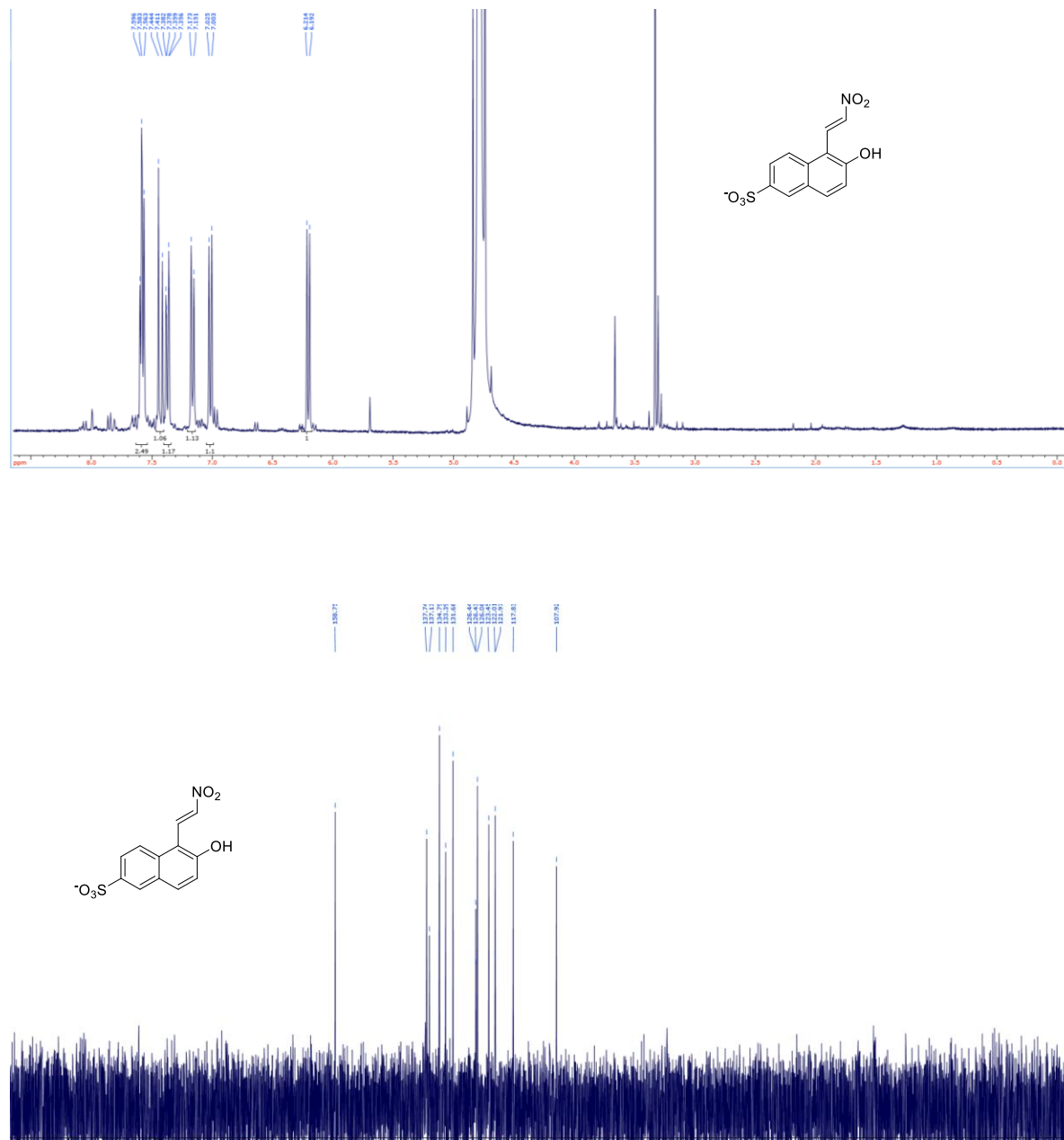


**Figure 4.S1**  $^1\text{H}$  and  $^{13}\text{C}$  NMR spectra of sodium 6-hydroxy-5-(2-nitrovinyl)naphthalene-2-sulfonate.

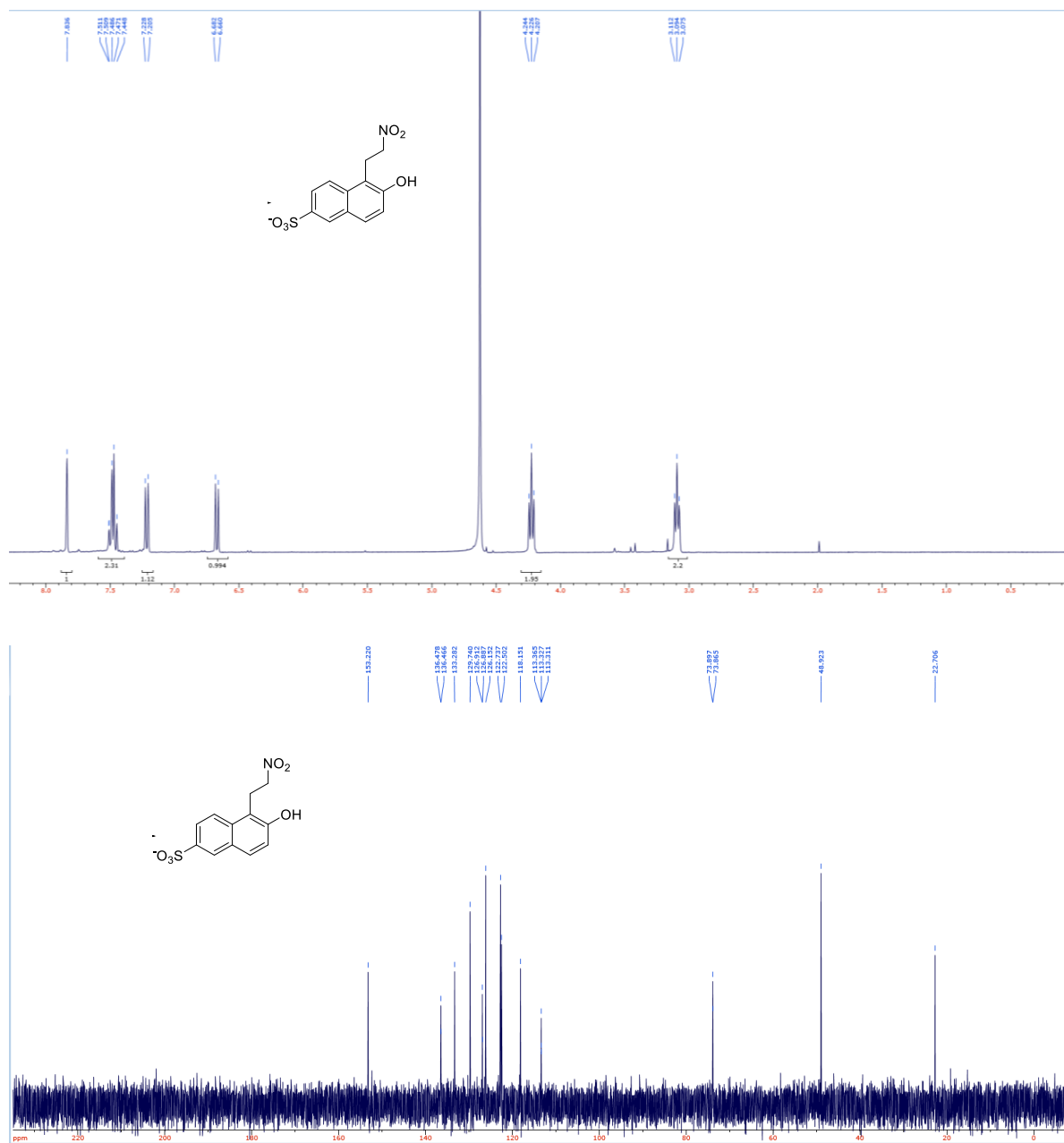


**Figure 4.S2**  $^1\text{H}$  and  $^{13}\text{C}$  NMR spectra of sodium 6-hydroxy-5-(2-nitroethyl)naphthalene-2-sulfonate.

**(b) ESI mass spectra**

FT40102\_180312153206 #184-191 RT: 4.12-4.23 AV: 8 NL: 2.43E7  
T: FTMS - p NSI Full ms [50.00-350.00]

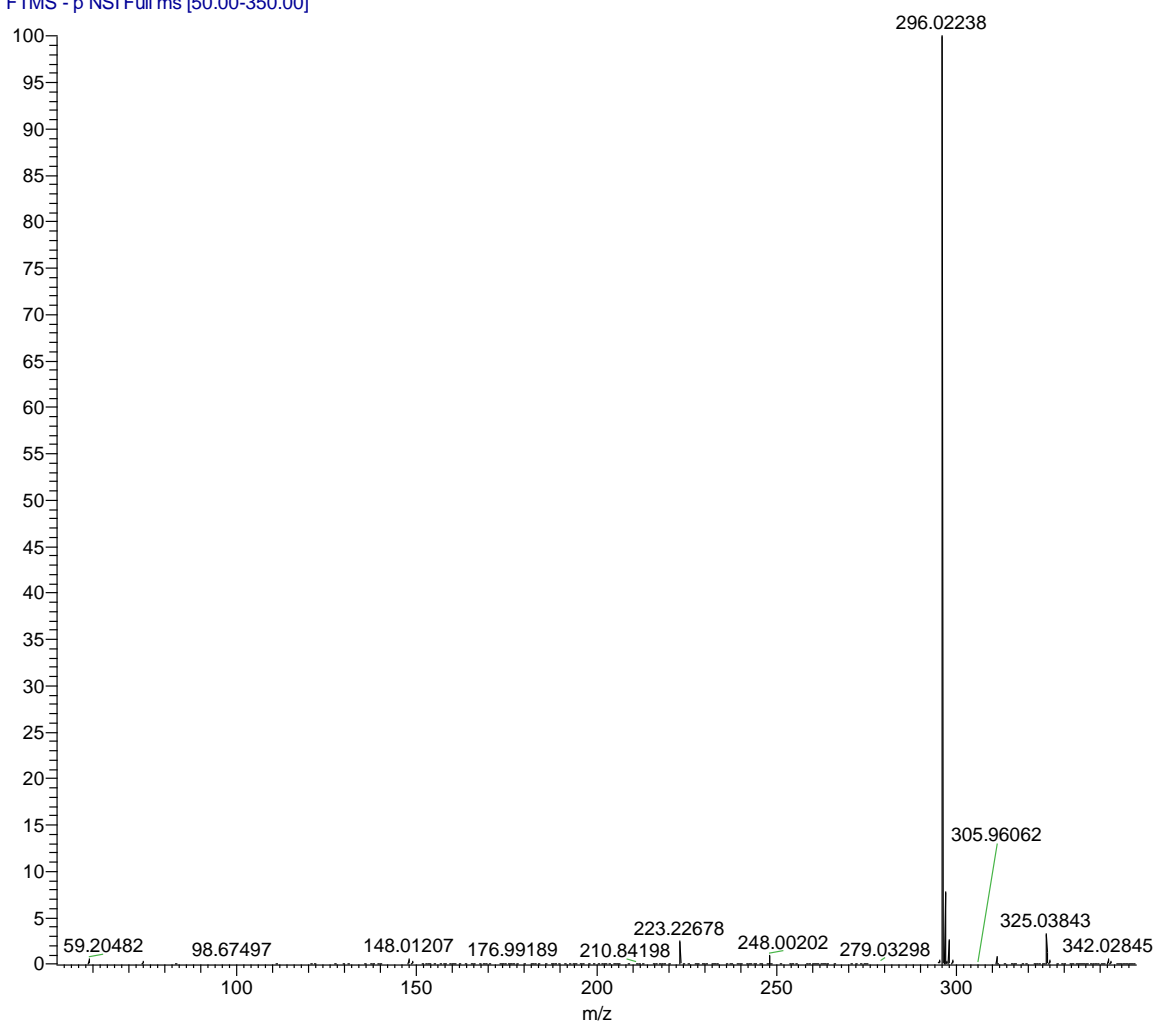


**Figure 4.S3** ESI mass spectrum of sodium 6-hydroxy-5-(2-nitroethyl)naphthalene-2-sulfonate.

#### 4.7 References

1. Mitchell, P., Coupling of Phosphorylation to Electron and Hydrogen Transfer by a Chemi-Osmotic type of Mechanism. *Nature* **1961**, *191* (4784), 144-148.
2. Kielian, M., Mechanisms of Virus Membrane Fusion Proteins. *Ann Rev Virol* **2014**, *1*, 171-189.
3. Wraight, C. A., Chance and design - Proton transfer in water, channels and bioenergetic proteins. *Bba-Bioenergetics* **2006**, *1757* (8), 886-912.
4. Clark, J. H.; Shapiro, S. L.; Campillo, A. J.; Winn, K. R., Picosecond Studies of Excited-State Protonation and Deprotonation Kinetics - Laser Ph Jump. *J Am Chem Soc* **1979**, *101* (3), 746-748.
5. Smith, K. K.; Kaufmann, K. J.; Huppert, D.; Gutman, M., Picosecond proton ejection: an ultrafast pH jump. *Chemical Physics Letters* **1979**, *64* (3), 522-527.
6. Gutman, M.; Nachliel, E., The Dynamic Aspects of Proton-Transfer Processes. *Biochim Biophys Acta* **1990**, *1015* (3), 391-414.
7. Abbruzzetti, S.; Carcelli, M.; Rogolino, D.; Viappiani, C., Deprotonation yields, pK(a), and aci-nitro decay rates in some substituted o-nitrobenzaldehydes. *Photochem. Photobiol. Sci.* **2003**, *2* (7), 796-800.
8. Donten, M. L.; Hamm, P., pH-Jump Overshooting. *J. Phys. Chem. Lett.* **2011**, *2* (13), 1607-1611.
9. Abbruzzetti, S.; Sottini, S.; Viappiani, C.; Corrie, J. E. T., Kinetics of proton release after flash photolysis of 1-(2-nitrophenyl)ethyl sulfate (caged sulfate) in aqueous solution. *J. Am. Chem. Soc.* **2005**, *127* (27), 9865-9874.

10. Barth, A.; Corrie, J. E. T., Characterization of a new caged proton capable of inducing large pH jumps. *Biophys. J.* **2002**, *83* (5), 2864-2871.
11. Causgrove, T. P.; Dyer, R. B., Nonequilibrium protein folding dynamics: laser-induced pH-jump studies of the-helix-coil transition. *Chem. Phys.* **2006**, *323* (1), 2-10.
12. Donten, M. L.; Hamm, P., pH-jump induced alpha-helix folding of poly-L-glutamic acid. *Chem. Phys.* **2013**, *422*, 124-130.
13. Hamm, P., pH-Jump Induced Leucine Zipper Folding Beyond the Diffusion Limit. *J. Phys. Chem. B* **2014**.
14. Abbruzzetti, S.; Sottini, S.; Viappiani, C.; Corrie, J. E. T., Acid-induced unfolding of myoglobin triggered by a laser pH jump method. *Photochem. Photobiol. Sci.* **2006**, *5* (6), 621-628.
15. Shi, Z.; Peng, P.; Strohecker, D.; Liao, Y., Long-Lived Photoacid Based upon a Photochromic Reaction. *J Am Chem Soc* **2011**, *133* (37), 14699-14703.
16. Nunes, R. M. D.; Pineiro, M.; Arnaut, L. G., Photoacid for Extremely Long-Lived and Reversible pH-Jumps. *J Am Chem Soc* **2009**, *131* (26), 9456-9462.
17. Johns, V. K.; Wang, Z. Z.; Li, X. X.; Liao, Y., Physicochemical Study of a Metastable-State Photoacid. *J Phys Chem A* **2013**, *117* (49), 13101-13104.
18. Jiang, L.; Wang, L.; Guo, M.; Yin, G.; Wang, R. Y., Fluorescence turn-on of easily prepared fluorescein derivatives by zinc cation in water and living cells. *Sensor Actuat B-Chem* **2011**, *156* (2), 825-831.
19. Víctor, T. P.; L., F. d. A. Á.; M., M. L.; Luis, S.; H., R. O.; Francisca, S.; R., M. J., A High Yield Procedure for the Preparation of 2-Hydroxynitrostyrenes: Synthesis of

Imines and Tetracyclic 1,3-Benzoxazines. *European Journal of Organic Chemistry* **2014**, 2014 (15), 3242-3248.



## **Chapter 5: Investigation of Interaction between Mastoparan X and Membrane by Using 2,7-DiazaTrp as a Local Hydration Level Sensor**

### **5.1 Abstract**

Water is ubiquitous and essential for all biological systems, and it plays an indispensable role in modulating the structures, dynamics and functions of proteins. Thus, it has been of great interest to study water-protein interactions, and many optical probes of local hydration level studies have been developed. 2,7-diazaTrp is one example and has the unique advantage of a water-sensitive emission at 500 nm. 2,7-diazaTrp was incorporated in mastoparan X (MX), an antimicrobial peptide (AMP) from wasp venom, and its interaction with DPPC membrane was studied. From fluorescence spectra, it was observed that MX is partially dehydrated, indicating it is bound to membrane surface but not fully inserted. Further experiments would give more insights about the mechanism of interaction between AMP and membrane.

### **5.2 Introduction**

All biological processes such as protein folding, ligand binding and enzymatic reaction take place in aqueous environments. Interactions between proteins with water molecules have great influence for their structure, dynamics, and functions.<sup>1-3</sup> Water is an integral component of protein folding in that it drives hydrophobic collapse of protein folding core, participates in hydrogen bonding network among amino acids, and shields electrostatic interactions from charged residues. Especially, buried water molecules inside protein core

plays invaluable role to stabilize protein structure by forming structurally-important hydrogen-bonded linkages with protein backbone and side chains.<sup>4</sup> Water molecules on protein surface, whose properties are different from the bulk water, forms about 1-1.5 nm thickness of the first hydration shell, which contributes to the stability and dynamics of protein structures. Their exchange rate and dynamics have been studied by NMR, and the residence time of water range from tens of ps to several ns.<sup>3</sup> It was reported that the translational diffusion of those surface water molecules is linked to the protein dynamics.<sup>5</sup> On the contrary, proteins in organic solvents exhibited lack of motion and activity.<sup>6</sup> In addition to protein structure and dynamics, water molecules also regulate enzyme catalysis. For example, in the active site of the membrane type I matrix metalloproteinase, there are two auxiliary water molecules; one stabilizes the key intermediate by hydrogen-bonding to the substrate, and another facilitates the product release.<sup>7</sup> Moreover, water is involved in protein-protein or protein-DNA interaction as an essential part.<sup>8</sup>

Therefore, there have been extensive efforts to study local hydration level of proteins. One of the strategies is to take an advantage of environmentally-sensitive dyes. The stretching vibration of cyano ( $C\equiv N$ ) group is known to be sensitive to the microscopic environment, and *p*-cyanoPhe<sup>9-10</sup>, cyanoCys<sup>11</sup>, 5-cyanoTrp<sup>12-13</sup> and cyanate have been used to probe local hydration levels of proteins. In the same way, the azide ( $N_3$ ) group has been also utilized.<sup>14-15</sup> On the other hand, excited-state intramolecular proton transfer (ESIPT) dyes were employed as a local hydration level sensor. While ESIPT dye is in excited-state, its proton is transported not only to water, but also to another ionizable residue in the same molecule, resulting in a phototautomer ( $T^*$ ) that has distinct spectral properties. Under steady-state excitation of ESIPT dye, there can be two species; normal excited state ( $N^*$ )

and ESIPT phototautomer (T\*) product, showing dual emission. Such dual emission is highly sensitive to its microenvironment because a decrease in polarity and hydrogen bond donor ability of microenvironment can preferentially inhibit ESIPT process, which suppresses T\* species generation. From the ratio between N\* and T\* species, one can probe a polarity and hydration level of the microenvironment. Owing to these unique characteristics of ESIPT dye, protein local hydration level<sup>16</sup>, protein-protein<sup>17</sup>, and protein-DNA interactions<sup>18</sup> were studied with ESIPT dyes as a sensor.

However, sensors mentioned above are sensitive to, in general, the local dielectric constant or hydrogen bond donors, not specifically to the water molecules. This is the same issue with conventional fluorescent probe such as tryptophan and pyrene. From their quantum yield and spectral shift, one can only indirectly infer local hydration level although there is a possibility that other factors such as different hydrogen bonding or protonation state of protein side chain can induce the spectral change.

Therefore, 2,7-DiazaTrp, which is exclusively sensitive to the water molecule, was introduced as hydration level sensor.<sup>19</sup> 2,7-DiazaTryptophan is an unnatural amino acid, which undergoes ESIPT from N1 proton to N7 position only when an aprotic solvent such as water or methanol catalyzes it. (Figure 5.1) The N7 protonated species shows emission centered at 500 nm, thereby making it a unique local hydration sensor, 2,7-DiazaTrp was incorporated into many proteins such as thromboxane A<sub>2</sub> synthase<sup>19</sup>, ribonuclease T<sup>20</sup>, ascorbate peroxidase<sup>21</sup>, and asparaginase isozymes<sup>22</sup>. Moreover, protein-protein interaction between calmodulin and Baa peptide was investigated by probing interfacial microenvironment change with 2,7-DiazaTrp.<sup>23</sup>

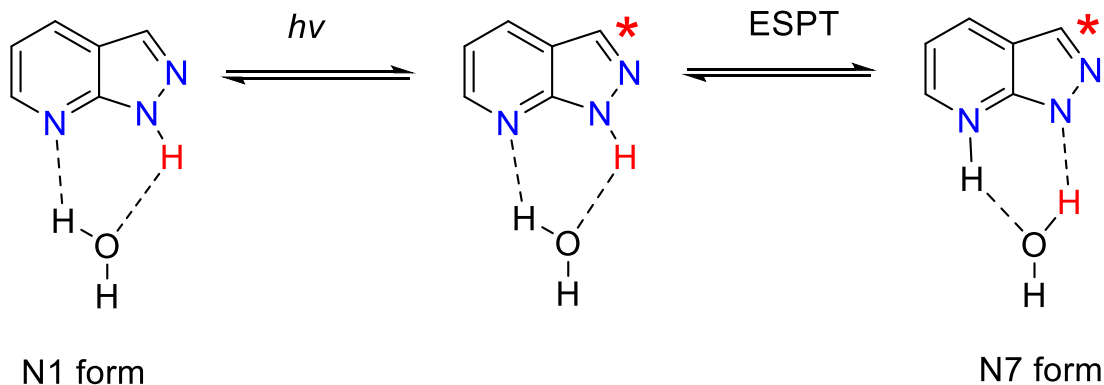


**Figure 5.1** ESPT of 2,7-Diazaindole in the presence of water.

In this report, 2,7-diazaTrp was incorporated into mastoparan X (MX), which is an antimicrobial peptide (AMP) from wasp venom. Its interaction with membrane and the specific membrane disruption mechanism were also elucidated. AMP has been widely used as food preservative<sup>24</sup> and treatments<sup>25</sup> for pneumonia, bacterial infections, hepatitis C, and HIV. As the drug resistance of bacteria becomes more severe problems, the importance of AMPs are growing.

In general, AMP is unstructured in an aqueous environment, but, after binding to the bacterial membrane surface, it folds and disrupts bacterial membrane through mechanisms that are still unclear. There are several models proposed from experimental results; (a) barrel-stave, (b) toroidal, and (c) carpet-like model.<sup>26</sup> In the barrel-stave model, peptides form transmembrane pores like other membrane channel proteins. However, for short peptides which are not long enough to form a single span membrane channel, they tend to follow the toroidal model where they make pores by interacting with lipid headgroups, inducing and stabilizing highly curved lipid structures so that the outer leaflet and inner

leaflet are connected. In the carpet-like model, peptides accumulate on the surface of membrane and disrupt interactions among lipids, loosening the lipid packing which disrupts membrane integrity. All of these cases were experimentally observed, but, it is difficult to allocate the appropriate model to each AMPs.

Here, we employed 2,7-(diaz)Trp as a local hydration level sensor to discriminate each model of AMP-membrane interaction. In the case of barrel-stave model, it might be expected to see the most dehydrated state because the peptide makes direct contact with hydrophobic core of lipid bilayer. On the other hand, for toroidal model, peptides only interact with lipid head group, thus, the most hydrated condition might be observed. For carpet-like model, AMPs are located nearby the interface between lipid and bulk water, therefore, intermediate level of hydration might be measured.

### 5.3 Experimental

**Materials.** Fmoc-osu, acetic anhydride, acetic acid and Acylase I from *Aspergillus melleus* were purchased from Aldrich and used without further purification. D,L-2,7-diazaTryptophan was synthesized as described.<sup>19</sup> <sup>1</sup>H NMR and <sup>13</sup>C NMR were measured on a Varian INOVA 400 MHz NMR spectrometer. UV-vis and fluorescence spectra were recorded on Jobin Yvon Dual Fluorometer. MALDI Mass spectroscopy was recorded on Applied Biosystem 4700.

**L-(2,7-diaza)Trp.** Racemic mixture, D,L-(2,7-diaza)Trp (1 g, 4.9 mmol) was dissolved in water (100 ml), and acetic anhydride (0.75 g, 7.4 mmol) was slowly added into a one-neck round bottom flask and stirred at RT for overnight. The solution was neutralized by adding

1M NaOH, and 100mM pH 7.5 phosphate buffer (100 ml) was added. Then, acylase I from *Aspergillus melleus* (20 mg) was added and pH was kept adjusted to pH 7.5. The reaction mixture was stirred at 40 °C for 48h. The solvent was removed under reduced pressure, and the resulting residue was purified by semipreparative RP-HPLC on C-18 column, eluted with a linear gradient from 100% water:0.1% TFA to 20% acetonitrile:80% water:0.1% TFA at a flow rate of 10 ml/min. After purification, solvent was dried under reduced pressure, yielding the product as a white powder in 40% yield. The optical purity of L-(2,7-diaza)Trp was further verified by chiral column (Crownpak-Cr(+)). L-(2,7-diaza)Trp was eluted with 97% pH 1.5 perchloric acid buffer : 3% methanol. <sup>1</sup>H NMR (D<sub>2</sub>O, 400 MHz):  $\delta$  (ppm) = 3.56(t, 2H,  $J$  = 6.0 Hz), 4.39(t, 1H,  $J$  = 6.0 Hz), 7.41(dt, 1H,  $J$  = 1.6, 7.2 Hz), 8.47 (d, 1H,  $J$  = 7.2 Hz), 8.66 (d, 1H,  $J$  = 7.2 Hz).

**Fmoc-L-(2,7-diaza)Trp.** L-(2,7-diaza)Trp (0.48 g, 2.31 mmol) was added to water (50 ml), and stirred at 0 °C. Into the solution, sodium bicarbonate (0.388 g, 4.61 mmol) was added in portions. Then, solution of Fmoc-osu (3.47 mmol, 1.17 g) in acetone was slowly added. The resulting mixture was allowed to warm back to room temperature and stirred overnight. Then, water was added and the aqueous layer was extracted with hexane three times. Aqueous layer was acidified to pH ~2, and extracted with ethyl acetate (EA) three times. The combined EA layer was dried with sodium sulfate and concentrated under reduced pressure. The product was purified by flash column with EA/MeOH (50:50 v/v) to obtain the product as white solid with 91% of yield.

**Peptide synthesis.** Mastoparan X (INWKGIAAMAKLL) was synthesized via standard 9-fluorenylmethoxycarbonyl (Fmoc)-based solid-phase chemistry in a microwave peptide synthesizer (CEM). Fmoc-PAL-PS resin (Applied Biosystems, Foster City, CA) was used

to form a peptide amide. Peptide cleavage was performed using a cocktail of 90% trifluoroacetic acid (TFA), 5% thioanisole, 3% ethanedithiol, and 2% anisole for 180 min. The resulting mixture was filtered and precipitated in ice-cold ether. The peptide was purified by reverse phase-HPLC on a C-18 preparative column with a linear gradient of buffer A (0.1% TFA in H<sub>2</sub>O) and buffer B (0.1% TFA in acetonitrile). The purified peptide was verified by MALDI mass spectroscopy and then lyophilized.

#### 5.4 Results and Discussions

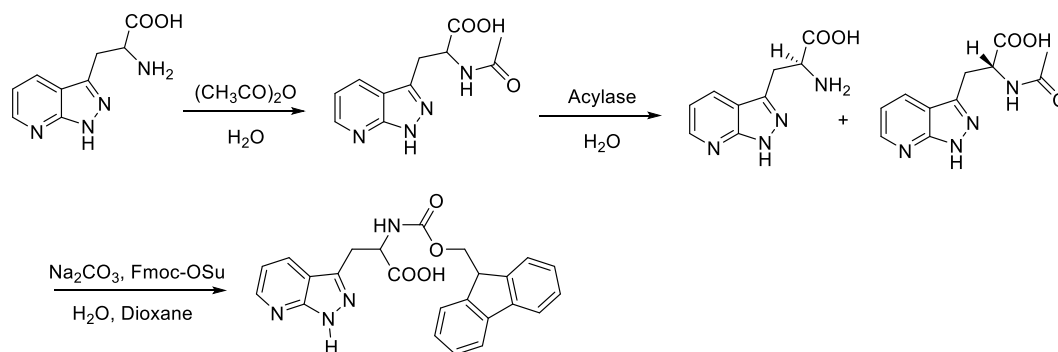


**Figure 5.2** Synthetic Scheme of Fmoc-L-(2,7-diaza)Trp.

#### Synthesis and Spectral Characterization of L-(2,7-diaza)Trp

For the first time, racemic resolution of (2,7-diaza)Trp was achieved by using Acylase enzyme. (Figure 5.2) A large scale (> 5 g) reaction was also carried out by this enzymatic resolution method. *Aspergillus melleus* acylase I could enantioselectively hydrolyze L-acetyl-(2,7-diaza)Trp. The optical purity of L-(2,7-diaza)Trp was further confirmed by chiral column. (Figure 5.3)

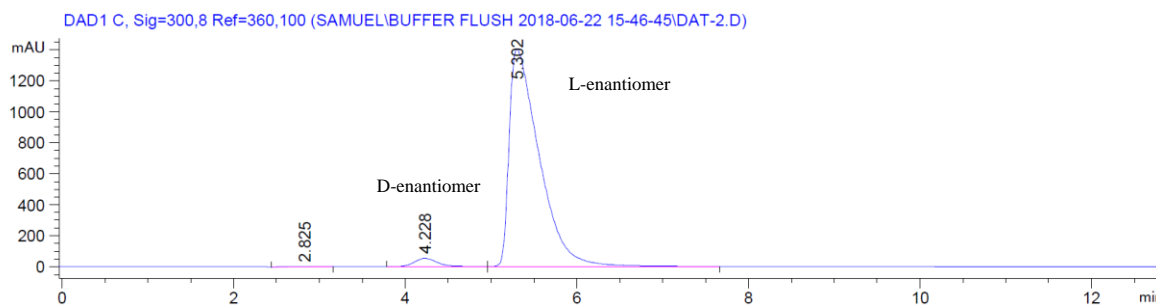


**Figure 5.3** Enantioselective separation of 2,7-diazaTrp on the chiral column.

The absorbance and fluorescence spectra of 2,7-diazaTrp were measured, and were consistent with previously reported spectra.<sup>19</sup> (Figure 5.4) Its fluorescence spectrum was deconvoluted into three gaussian peaks, which correspond to N1 position, N2 position, or N7 position protonated diazaTrp fluorescence. (Figure 5.5, Table 5.1) For deconvolution, center wavelength of N7 species is fixed at 500 nm because it was too broad to be accurately fitted. In MeOH, the ratio between N1 and N2 species fluorescence intensity is increased as reported previously. (Figure 5.5, Table 5.2)



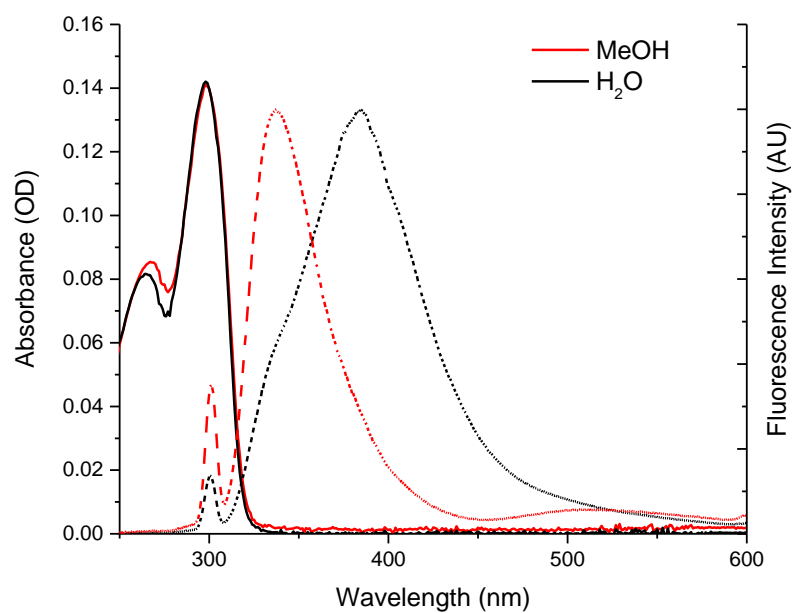


**Figure 5.4** Absorbance (solid line) and Emission (dotted line) Spectrum of diAzaTrp in MeOH (red) or pH 7 phosphate buffer (black).

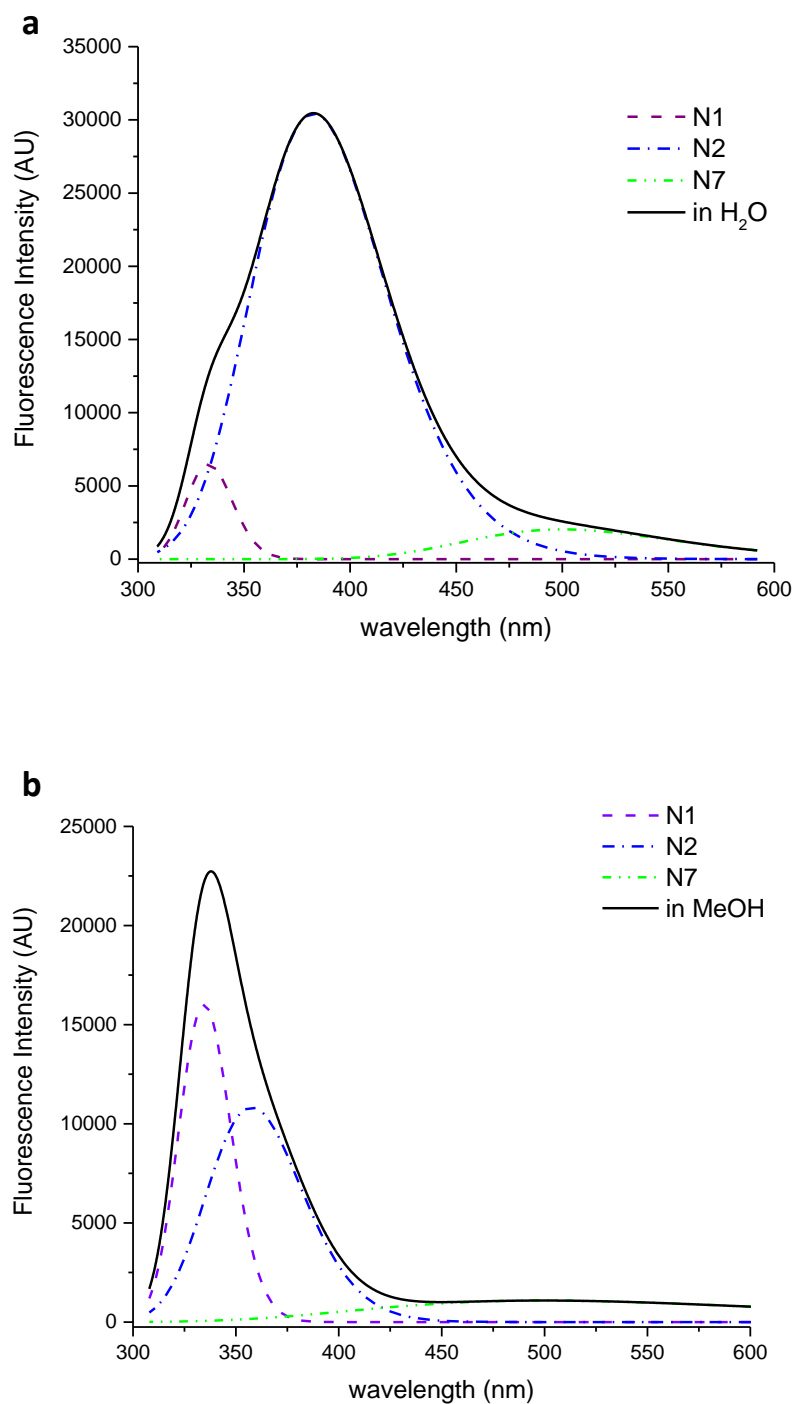
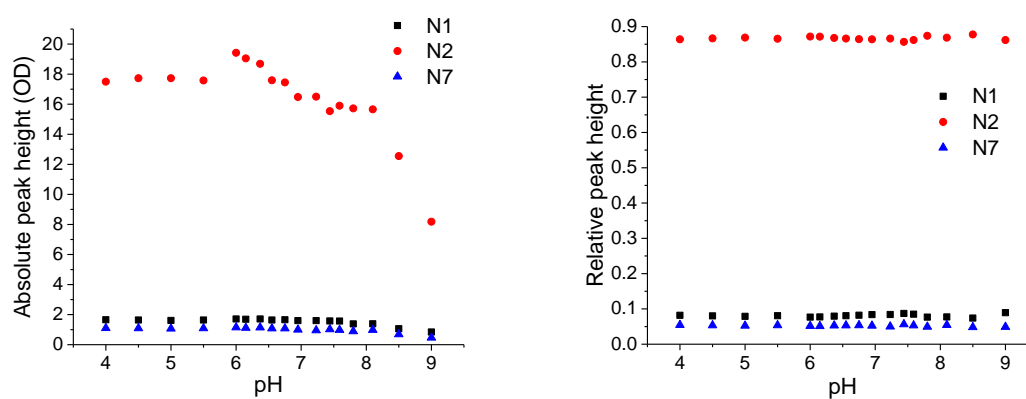


**Figure 5.5** Fluorescence spectrum of DiazaTrp in (a) pH 7 buffer or (b) MeOH, and deconvoluted fluorescence spectra of N1, N2, and N7 position protonated species.

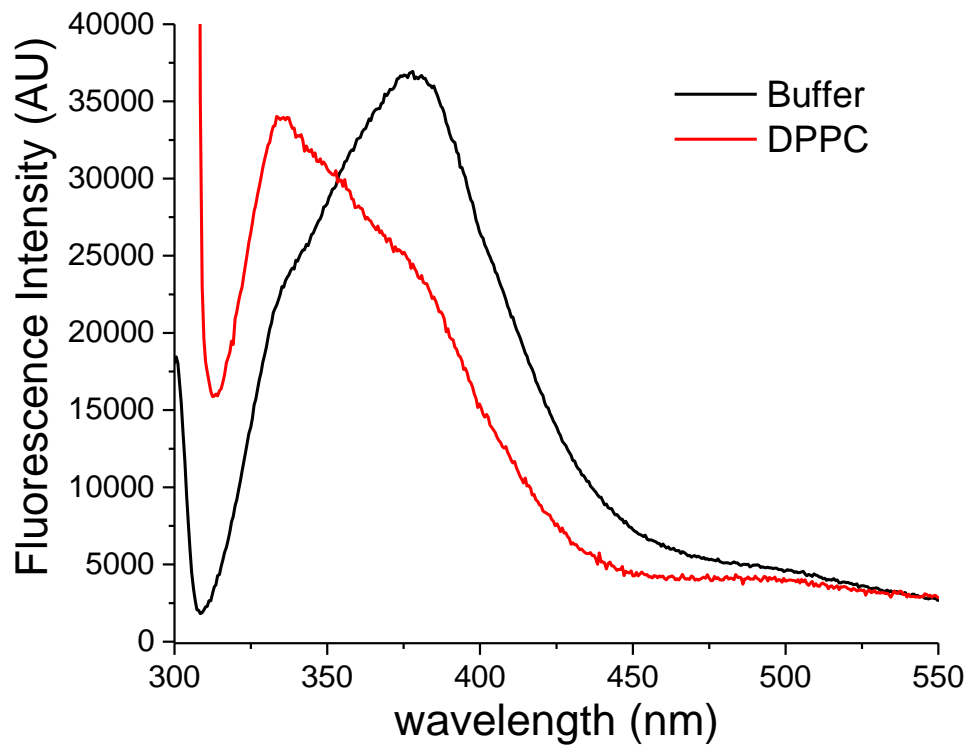
	$\lambda_{em}$ (nm)	Emission intensity (AU)	Relative emission intensity	FWHM ( $10^{-4}$ nm)
<b>2,7-diazaTrp in pH 7 buffer</b>	333.3	177553	0.062	2.33
	383.1	2462800	0.856	5.09
	500	236742	0.082	4.66
<b>2,7-diazaTrp in MeOH</b>	334.5	506289	0.373	2.67
	357.1	633520	0.467	4.26
	500	216129	0.159	9.62
<b>diazaTrpMX in pH 7 buffer</b>	332.2	267517	0.074	2.26
	374.5	2871210	0.791	5.18
	500	492385	0.136	4.80
<b>diazaTrpMX with DPPC vesicle in pH 7 buffer</b>	330.0	397376	0.24	3.13
	367.7	966973	0.585	5.24
	500	287972	0.174	5.45

**Table 5.1** Photophysical properties of deconvoluted fluorescence spectrum.

The pH dependence was investigated to measure  $pK_a$  values of N1, N2, and N7 amines on 2,7-diazaIndole sidechain. (Figure 5.7) Its absorbance and fluorescence were measured in various pH buffers, and, strikingly, its absorbance didn't show any change. Below pH 8, there is some change for N2 fluorescence, but overall, relative intensity ratio among N1, N2, and N3 species stays constant. Additional experiments need to be done to explain this result, because it is known that  $pK_a$  of N7 position of 7-azaIndole is about 4.6, and  $pK_a$  of 7-methyl-2,7,-diazatrp was 5.8.



**Figure 5.6** pH-dependent intensity change of N1, N2, and N7 position protonated species.

**Mastoparan X–Membrane Interaction Probed by Fluorescence Spectroscopy**

**Figure 5.7** Fluorescence spectra of Trp3diazatrp mutant of Mastoparan X in pH 7 buffer (black) or in 1mM DPPC SUV solution with pH 7 buffer (red).

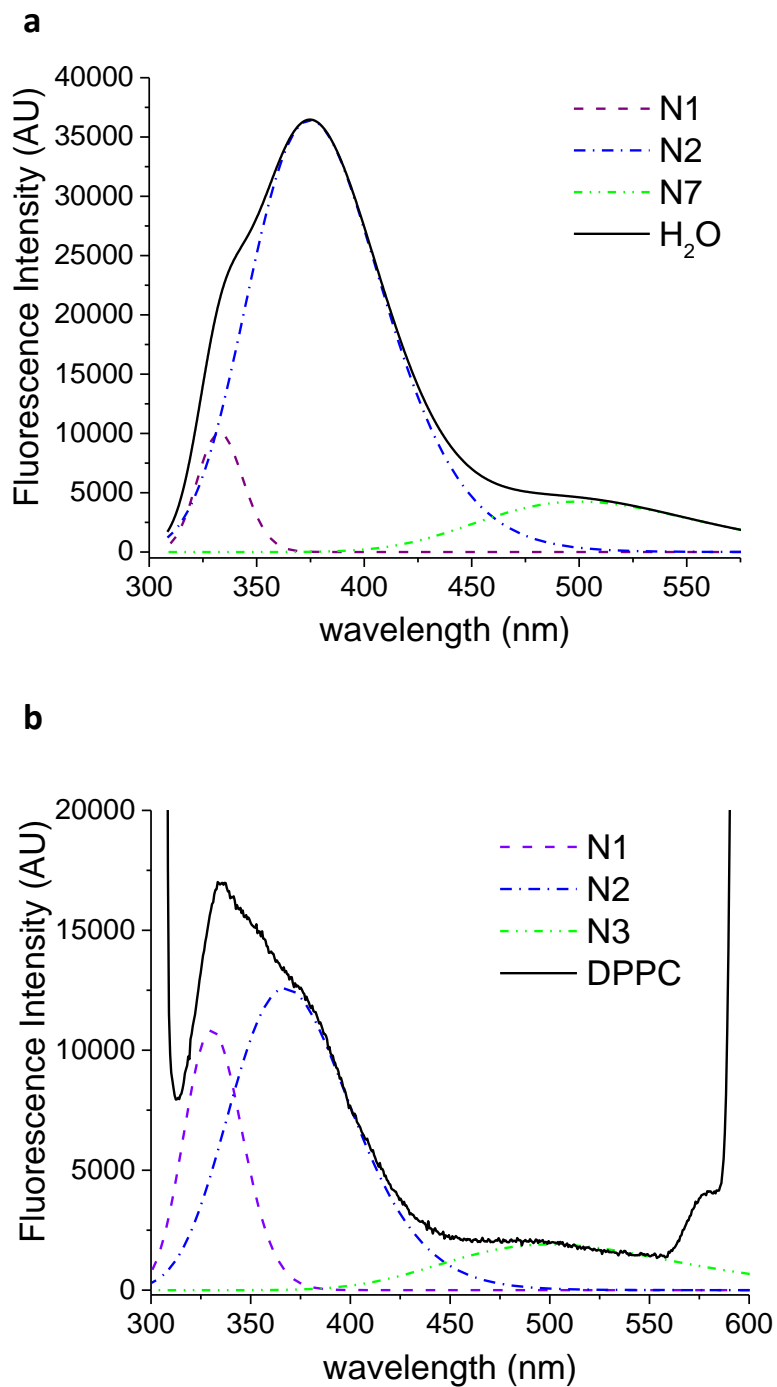


**Figure 5.8** Fluorescence spectrum of Trp3diazatrp mutant of Mastoparan X in (a) pH 7 buffer or (b) 1mM DPPC SUV solution at pH 7, and deconvoluted fluorescence spectra of N1, N2, and N7 position protonated species.

The fluorescence spectrum of Trp3diazaTrp mutant of Mastoparan X in pH 7 buffer showed several differences from that of diazaTrp amino acid in pH 7 buffer (Figure 5.8); (a) fluorescence was blue-shifted and (b) more N1 and N2 species are populated. (Table 5.1) When it is added to 1mM DPPC SUV solution, its fluorescence exhibited drastic changes: (a) fluorescence was further blue-shifted: N1: 2 nm, N2: 7 nm and (b) relative fluorescence of each species were significantly changed: N1(0.074 to 0.24), N2(0.791 to 0.585), and N7(0.136 to 0.176). The same kind of trend was reported from calmodulin-Baa peptide binding titration experiment<sup>23</sup>: The N2 species only exist in bulk water and gradually disappeared in dehydrated environments. However, in this result, only partial reduction of N2 species was observed, indicating MX peptide is partially dehydrated. The presence of N7 state further support that MX still experiences somewhat hydrated microenvironment. This is in line with a previous study: MX binds on the surface of DPPC membrane under  $T_m$  of DPPC lipid<sup>27</sup> or on DMPC membrane<sup>28</sup>. Moreover, NMR study showed that MX is parallelly bound to the zwitterionic phosphatidyl choline (PC) membrane surface, while, in anionic lipid, is perpendicularly bound to the membrane surface.<sup>29</sup> Therefore, MX can be considered to be located at the interfacial space between bulk water and head group of zwitterionic lipids. This demonstrates the utility of the unique water sensor, 2,7-DiazaTrp, to study the protein-membrane interactions.

## 5.5 Conclusion

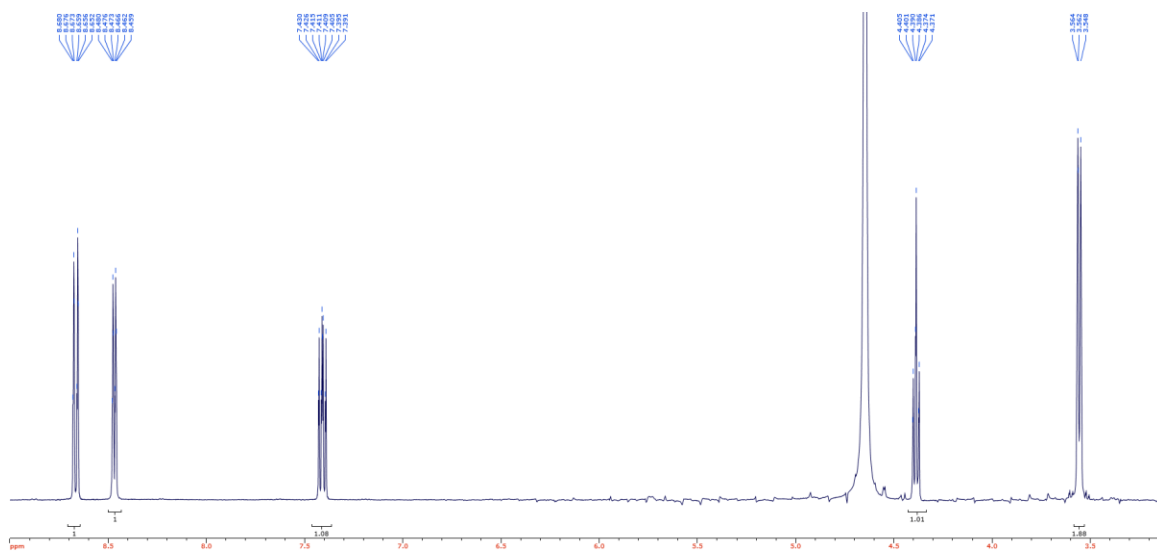
For the first time, racemic mixture of 2,7-diazaTrp was resolved to L-enantiomer by relatively facile and inexpensive method, enzymatic resolution. Trp3 of MX was replaced by diazaTrp and it was used to study the interaction of MX with DPPC vesicle,

demonstrating that valuable information about its local hydration level can be easily obtained. Further experiments can be designed to gain more information: (a) Temperature melting experiment with DPPC can allow complete insertion of MX into membrane, thus, the transition of hydration level can be followed. (b) Different membrane composition such as negatively charged lipid to study its insertion angle. (c) Other AMPs such as Magainin or Melittin would be used to study their own membrane disruption mechanism.

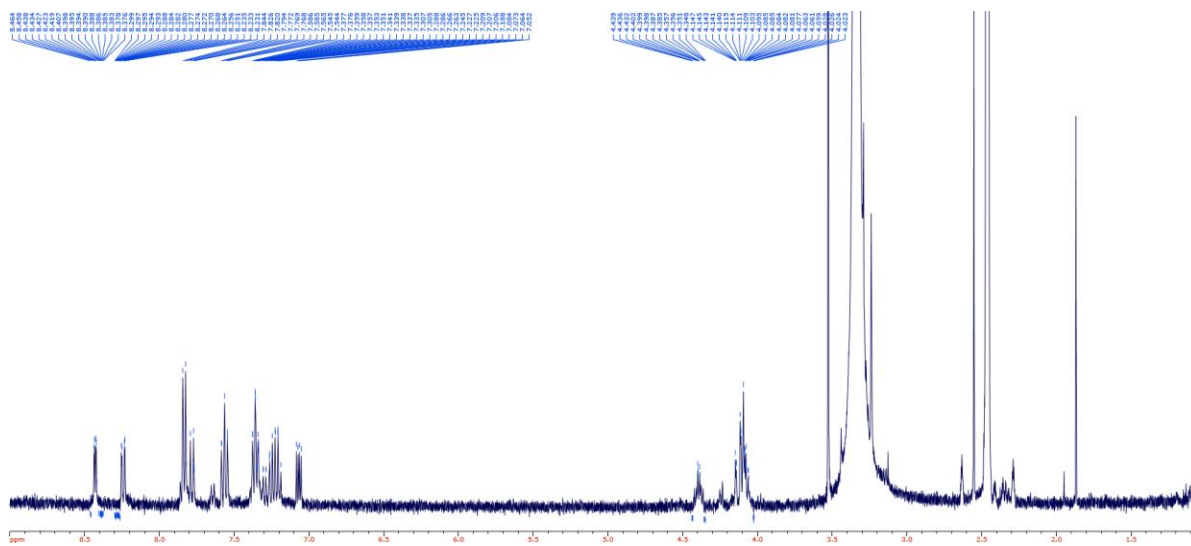


## 5.6 Appendix

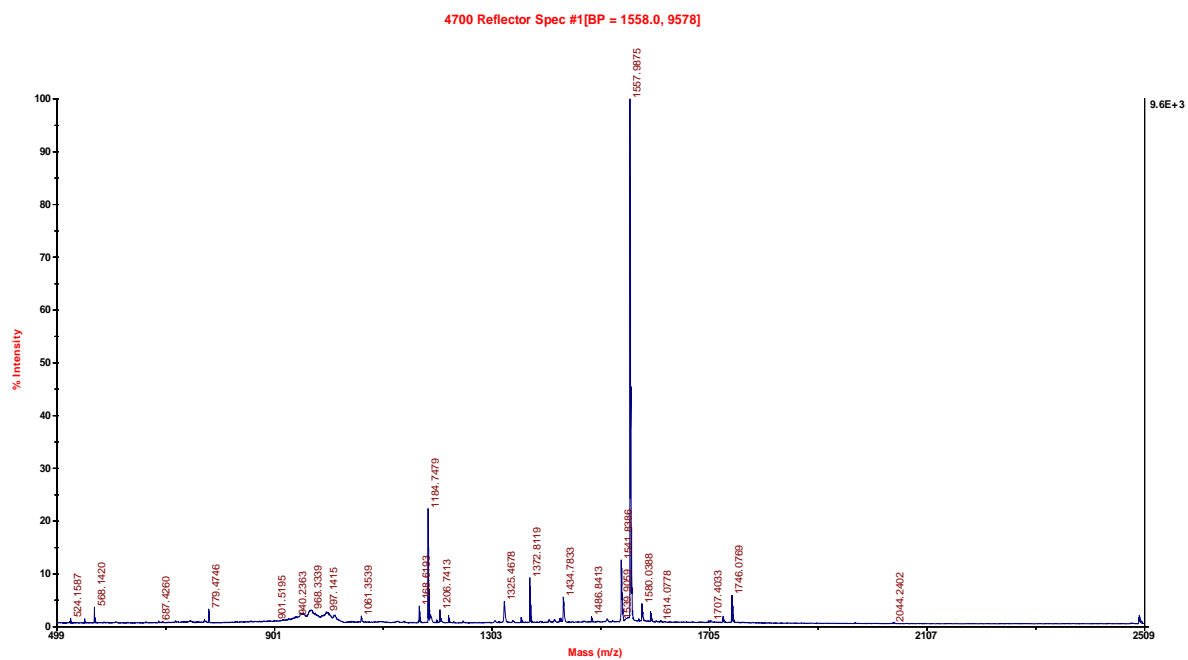
### (a) NMR spectra



**Figure 5.S1**  $^1\text{H}$  NMR spectrum of L-(2,7-diaza)Trp in  $\text{D}_2\text{O}$ .



**Figure 5.S2**  $^1\text{H}$  NMR spectrum of Fmoc-L-(2,7-diaza)Trp in DMSO.

**(b) MALDI Mass Spectrum**

**Figure 5.S3** MALDI mass spectrum of Trp3DiazaTrp mutant of Mastoparan X peptide.

## 5.7 References

1. Levy, Y.; Onuchic, J. N., Water and proteins: a love-hate relationship. *Proc Natl Acad Sci U S A* **2004**, *101* (10), 3325-6.
2. Privalov, P. L.; Crane-Robinson, C., Role of water in the formation of macromolecular structures. *Eur Biophys J* **2017**, *46* (3), 203-224.
3. Mattos, C., Protein-water interactions in a dynamic world. *Trends Biochem Sci* **2002**, *27* (4), 203-8.
4. Ernst, J. A.; Clubb, R. T.; Zhou, H. X.; Gronenborn, A. M.; Clore, G. M., Demonstration of Positionally Disordered Water within a Protein Hydrophobic Cavity by Nmr. *Science* **1995**, *267* (5205), 1813-1817.
5. Schiro, G.; Fichou, Y.; Gallat, F. X.; Wood, K.; Gabel, F.; Moulin, M.; Hartlein, M.; Heyden, M.; Colletier, J. P.; Orecchini, A.; Paciaroni, A.; Wuttke, J.; Tobias, D. J.; Weik, M., Translational diffusion of hydration water correlates with functional motions in folded and intrinsically disordered proteins. *Nat Commun* **2015**, *6*, 6490.
6. Mattos, C.; Ringe, D., Proteins in organic solvents. *Curr Opin Struct Biol* **2001**, *11* (6), 761-4.
7. Decaneto, E.; Vasilevskaya, T.; Kutin, Y.; Ogata, H.; Grossman, M.; Sagi, I.; Havenith, M.; Lubitz, W.; Thiel, W.; Cox, N., Solvent water interactions within the active site of the membrane type I matrix metalloproteinase. *Phys Chem Chem Phys* **2017**, *19* (45), 30316-30331.
8. Ladbury, J. E., Just add water! The effect of water on the specificity of protein-ligand binding sites and its potential application to drug design. *Chem Biol* **1996**, *3* (12), 973-980.

9. Zimmermann, J.; Thielges, M. C.; Seo, Y. J.; Dawson, P. E.; Romesberg, F. E., Cyano Groups as Probes of Protein Microenvironments and Dynamics. *Angewandte Chemie International Edition* **2011**, *50* (36), 8333-8337.
10. Shrestha, R.; Cardenas, A. E.; Elber, R.; Webb, L. J., Measurement of the Membrane Dipole Electric Field in DMPC Vesicles Using Vibrational Shifts of p-Cyanophenylalanine and Molecular Dynamics Simulations. *The Journal of Physical Chemistry B* **2015**, *119* (7), 2869-2876.
11. Fafarman, A. T.; Webb, L. J.; Chuang, J. I.; Boxer, S. G., Site-Specific Conversion of Cysteine Thiols into Thiocyanate Creates an IR Probe for Electric Fields in Proteins. *Journal of the American Chemical Society* **2006**, *128* (41), 13356-13357.
12. Waegele, M. M.; Tucker, M. J.; Gai, F., 5-Cyanotryptophan as an infrared probe of local hydration status of proteins. *Chemical Physics Letters* **2009**, *478* (4-6), 249-253.
13. Markiewicz, B. N.; Mukherjee, D.; Troxler, T.; Gai, F., Utility of 5-Cyanotryptophan Fluorescence as a Sensitive Probe of Protein Hydration. *J Phys Chem B* **2016**, *120* (5), 936-944.
14. Choi, J.-H.; Raleigh, D.; Cho, M., Azido Homocysteine is a Useful Infrared Probe for Monitoring Local Electrostatics and Side-Chain Solvation in Proteins. *The Journal of Physical Chemistry Letters* **2011**, *2* (17), 2158-2162.
15. Wolfshorndl, M. P.; Baskin, R.; Dhawan, I.; Londergan, C. H., Covalently Bound Azido Groups Are Very Specific Water Sensors, Even in Hydrogen-Bonding Environments. *The Journal of Physical Chemistry B* **2012**, *116* (3), 1172-1179.
16. Amaro, M.; Brezovsky, J.; Kovacova, S.; Sykora, J.; Bednar, D.; Nemecek, V.; Liskova, V.; Kurumbang, N. P.; Beerens, K.; Chaloupkova, R.; Paruch, K.; Hof, M.;

- Damborsky, J., Site-Specific Analysis of Protein Hydration Based on Unnatural Amino Acid Fluorescence. *Journal of the American Chemical Society* **2015**, *137* (15), 4988-4992.
17. Yushchenko, D. A.; Fauerbach, J. A.; Thirunavukkuarasu, S.; Jares-Erijman, E. A.; Jovin, T. M., Fluorescent ratiometric MFC probe sensitive to early stages of alpha-synuclein aggregation. *J Am Chem Soc* **2010**, *132* (23), 7860-1.
18. Kuznetsova, A. A.; Kuznetsov, N. A.; Vorobjev, Y. N.; Barthes, N. P. F.; Michel, B. Y.; Burger, A.; Fedorova, O. S., New Environment-Sensitive Multichannel DNA Fluorescent Label for Investigation of the Protein-DNA Interactions. *Plos One* **2014**, *9* (6).
19. Shen, J.-Y.; Chao, W.-C.; Liu, C.; Pan, H.-A.; Yang, H.-C.; Chen, C.-L.; Lan, Y.-K.; Lin, L.-J.; Wang, J.-S.; Lu, J.-F.; Chun-Wei Chou, S.; Tang, K.-C.; Chou, P.-T., Probing water micro-solvation in proteins by water catalysed proton-transfer tautomerism. *Nature Communications* **2013**, *4* (1).
20. Chao, W.-C.; Shen, J.-Y.; Lu, J.-F.; Wang, J.-S.; Yang, H.-C.; Wee, K.; Lin, L.-J.; Kuo, Y.-C.; Yang, C.-H.; Weng, S.-H.; Huang, H.-C.; Chen, Y.-H.; Chou, P.-T., Probing Water Environment of Trp59 in Ribonuclease T1: Insight of the Structure–Water Network Relationship. *The Journal of Physical Chemistry B* **2014**, *119* (6), 2157-2167.
21. Chao, W.-C.; Lin, L.-J.; Lu, J.-F.; Wang, J.-S.; Lin, T.-C.; Chen, Y.-H.; Chen, Y.-T.; Yang, H.-C.; Chou, P.-T., Unveiling the water-associated conformational mobility in the active site of ascorbate peroxidase. *Biochimica et Biophysica Acta (BBA) - General Subjects* **2018**, *1862* (3), 451-459.

22. Chao, W.-C.; Shen, J.-Y.; Yang, C.-H.; Lan, Y.-K.; Yuan, J.-H.; Lin, L.-J.; Yang, H.-C.; Lu, J.-F.; Wang, J.-S.; Wee, K.; Chen, Y.-H.; Chou, P.-T., The In Situ Tryptophan Analogue Probes the Conformational Dynamics in Asparaginase Isozymes. *Biophysical Journal* **2016**, *110* (8), 1732-1743.
23. Chen, Y.-T.; Chao, W.-C.; Kuo, H.-T.; Shen, J.-Y.; Chen, I. H.; Yang, H.-C.; Wang, J.-S.; Lu, J.-F.; Cheng, R. P.; Chou, P.-T., Probing the polarity and water environment at the protein-peptide binding interface using tryptophan analogues. *Biochemistry and Biophysics Reports* **2016**, *7*, 113-118.
24. Hansen, J. N., Nisin as a Model Food Preservative. *Crit Rev Food Sci* **1994**, *34* (1), 69-93.
25. Gomes, B.; Augusto, M. T.; Felicio, M. R.; Hollmann, A.; Franco, O. L.; Goncalves, S.; Santos, N. C., Designing improved active peptides for therapeutic approaches against infectious diseases. *Biotechnol Adv* **2018**, *36* (2), 415-429.
26. Sato, H.; Felix, J. B., Peptide-membrane interactions and mechanisms of membrane destruction by amphipathic alpha-helical antimicrobial peptides. *Bba-Biomembranes* **2006**, *1758* (9), 1245-1256.
27. Schuler, E. E.; Nagarajan, S.; Dyer, R. B., Submillisecond Dynamics of Mastoparan X Insertion into Lipid Membranes. *The Journal of Physical Chemistry Letters* **2016**, *7* (17), 3365-3370.
28. Fujita, K.; Kimura, S.; Imanishi, Y., Self-Assembly of Mastoparan-X Derivative Having Fluorescence Probe in Lipid Bilayer-Membrane. *Bba-Biomembranes* **1994**, *1195* (1), 157-163.

29. Whiles, J. A.; Brasseur, R.; Glover, K. J.; Melacini, G.; Komives, E. A.; Vold, R. R., Orientation and effects of mastoparan X on phospholipid bicelles. *Biophys J* **2001**, *80* (1), 280-93.

## Chapter 6: Conclusion

### 6.1 Summary

Proton can serve a wide variety of crucial features in the protein structures, protein-protein interactions, and catalytic activity of enzymes owing to its special characters. The importance of proton in biological system can be manifested by the proton gradient which plays central role in bioenergetics.

In this dissertation, in order to study the kinetics and mechanism of proton related processes in biochemical system, it was aimed to develop a laser pH-jump experimental technique. The novelty of the technique in this dissertation with respect to previous work is to probe Trp fluorescence during kinetics experiment. Even though there were several technical challenges, the fact that Trp is natural amino acid, therefore, in many cases, further labeling is not required, and Trp fluorescence is sensitive to its surrounding micro-environment makes it uniquely well-suited as a probing method. As an example, in chapter 2, the kinetics and mechanism of the proton conductance and the activation of Influenza A M2 proton channel was investigated, and it clearly showed double exponential decay of Trp fluorescence: the fast phase was ascribed to be protonation kinetics ( $\sim 2 \times 10^{10} \text{ M}^{-1}\text{s}^{-1}$ ), while the slow phase was attributed to the subsequent structural change ( $\sim 4 \times 10^3 \text{ M}^{-1}\text{s}^{-1}$ ). Next, in chapter 3, the conformation change of M2 proton channel during activation was probed by FRET experiment at various pH, where it showed a more “open” structure at lower pH, confirming its activation mechanism.

In chapter 4, an attempt to synthesize the water-soluble version of long-lived reversible photo-acid by adding sulfonate functional group was made. Due to the experimental restriction came from the



irreversible photo-acid, pH-jump experiment needed to repeat single-shot experiments. Not only waste of large quantity of samples, time and efforts, but also limited applications to step-scan FT-IR or 2D-IR called for the improvement of pH-jump technique by introducing long-lived reversible photo-acid, which release proton fast in sub-nanosecond time scale and recombine it slowly in several milliseconds time regime. Previously reported long-lived reversible photo-acid, 1-(2-Nitro-ethyl)-naphthalen-2-ol, was extremely hydrophobic, thus, not readily soluble to water, making its application for pH-jump almost impossible. To improve its hydrophilicity, it was designed to add a sulfate group on 7 position of 1-(2-Nitro-ethyl)-naphthalen-2-ol. The synthesis was successful, but, decreased  $pK_a$  of hydroxyl group of the product, 6-hydroxy-5-(2-nitroethyl)naphthalene-2-sulfonate, prevented intramolecular proton transfer, not allowing it to be long-lived.

In chapter 5, 2,7-diazaTrp was introduced to study local hydration level of proteins. 2,7-diazaTrp undergoes ES IPT from N1 proton to N7 position when water molecule catalyzes it, emitting around 500 nm to specifically report the presence of water molecule in surrounded micro-environment. This unique water sensor was replaced Trp3 of mastoparan X (MX), an antimicrobial peptide, to investigate the interaction between MX and membrane, exhibiting differences in its local environment after membrane binding of MX.

## 6.2 Perspective

There have been many endeavors to elucidate proton transfer mechanisms in various environments including aqueous solution, proteins, and interfaces.<sup>1-3</sup> However, they are not fully understood yet, not only for pure aqueous solution, but also, particularly, for complicated biological environments

such as protein interiors and water-membrane interfaces. There are several limitations to study proton related processes, and many technical trials are made to overcome such issues.

In most atomic resolution protein structures, protons are barely observed; for X-ray crystal structures, it is mainly because a proton has small size and very low electron density which is unfavorable to X-ray diffraction. Although the position of protons was resolved in several X-ray crystal structures<sup>4</sup>, it requires sub-Å of high resolution which limits its wide applications. To resolve the position of protons in a crystal structure of a protein, neutron diffraction was utilized since neutrons are scattered by atomic nuclei, not by low electron density of protons. And this method was further improved by isotope exchange of deuterium<sup>5-6</sup> although only few structures were resolved by neutron diffraction, due to the limited accessibility of neutron source, compared to the X-ray synchrotron. Cryo-electron microscopy (cryo-EM) showed rapid progress in terms of its resolution, but, so far, the resolution is not high enough to resolve the position of protons yet. Whereas, NMR has been a powerful tool to study protonation status and its dynamics because it can directly measure the nuclear spin of a proton. However, although continuous improvement is ongoing, it is difficult to study large proteins with this technique.

It is very challenging to predict precise pK<sub>a</sub> values of titratable residues located in protein interiors because the pK<sub>a</sub> of ionizable residue inside proteins often shows large perturbation from the pK<sub>a</sub> in aqueous environment.<sup>7</sup> pK<sub>a</sub> of titratable residue is very sensitive to its micro-environment in the sense that ionizable residue, either in protonated or deprotonated state, is stabilized by interactions with the local environment. There have been several computational approaches to predict pK<sub>a</sub> value of ionizable residues inside proteins, but it is not unusual for them to show huge deviation of predicted pK<sub>a</sub> values from the experimental value.<sup>8</sup> It is simply because there are too many factors to be considered: local dielectric, solvent accessibility, H-bond network, neighboring

dipole, charge, sidechain flexibility, protein backbone dynamics, possible multiple conformers and so on. Often, the protein structure responds to the protonation of its titratable residue, resulting in its conformational relaxation. This, in turn, shifts the  $pK_a$  again, leading to even more complicated calculations. Measuring  $pK_a$  of ionizable residues in a protein is also challenging; There are typically multiple titratable residues in one protein. Optically probing those ionizable sidechains almost always requires labeling of a protein either by fluorescent dye or isotope labeled amino acid. Recent progress in NMR technique opens new venue to measure  $pK_a$  of ionizable residues in protein readily and precisely. NMR became a routine technique for determining  $pK_a$  values in various proteins including M2 proton channel. (Table 3.2) Even many titratable residues in a single protein such as eight Lys in *apo* calmodulin could be resolved separately to determine each  $pK_a$  values.<sup>9</sup> Along with rapidly growing number of reported  $pK_a$  values of proteins, improvement of  $pK_a$  prediction method could be expedited.

The proton transfer shows fast dynamics in sub-ms time scale, thus, experimental implementations to observe such fast kinetics is challenging. A conventional rapid-mixer has fundamental limitation of mixing dead-time in several milliseconds. Sub-millisecond kinetics and mechanism study of proton transfer and related processes has been available by advancement of diverse spectroscopic techniques. 2D-IR could measure ultrafast kinetics in femtosecond time scale such as hydrogen bonding network dynamics in aqueous environment. However, the study has been limited to the steady-state dynamics and kinetics in equilibrium condition due to lack of proper triggering method. With step-scan FT-IR, sub-ms timescale kinetics of bacteriorhodopsin and photosynthetic reaction center were investigated, observing proton transfer through internal proton transfer network as well as conformation change of protein. So far, step-scan FT-IR experiments are restricted to small number of proteins which have intrinsic chromophore such as heme, porphyrin,

or retinal to trigger the processes with sharp laser pulse, although it has great potential to observe vibrational signature of a protein and its side-chains with high time resolution up to nanosecond time scale.

There are two types of kinetics measurement; One measures exchange kinetics in equilibrium state, and another measures kinetics under pre-equilibrium conditions. The later method, in other words, the relaxation method, perturbs equilibrium and then observes the system relaxing back to the equilibrium in time resolved manner. This relaxation method requires sharp triggering to synchronize the response from an ensemble of molecules, and short laser pulse has been the best triggering method for fast time resolution under microsecond regime. In order to apply relaxation method to study proton related processes, photo-acid photolysis by short laser pulse can be a sharp trigger to induce rapid change of pH in the sample. With reversible and irreversible photo-acid, proton transfer kinetics or/and subsequent biological processes could be successfully measured. (Chapter 2 & 3)

However, pH-jump technique has not been widely used to study many important proton channels and pumps such as ATP synthase, thermogenin (uncoupling protein, UCP), and bacterial flagella motor protein. Moreover, pH-jump has not been coupled to advanced spectroscopic techniques such as 2D-IR and step-scan FT-IR, and, in order to access such spectroscopic technique requiring large number of repetition, a long-lived reversible photo-acid could be a key. (Chapter 3) Combing pH-jump to diverse probing methods can vastly expand its applicability toward more diverse research subjects, providing more detailed information about sidechain-specific proton transfer kinetics and mechanism of proton channel and pumps and conformational dynamics as well.

For example, ATP synthase has been thoroughly studied due to its absolute importance in bioenergetics, and its working principle has been postulated from its atomic resolution structures.

However, so far, sub-millisecond time scale kinetics of proton transfer and protein structure rearrangement have not been investigated to confirm the proposed mechanism. pH-jump experiment coupled with 2D-IR or step-scan FT-IR allows one to observe the specific step and route for proton transfer and subsequent conformational change such as stalk rotation, as well as ATP synthesis processes, including active site rearrangement and subsequent bond formation between ADP and  $P_i$ .

Another instance could be thermogenin, or uncoupling protein (UCP), which located in mitochondria of brown adipose cells and generates heat by uncoupling the proton gradient. It is known that its non-shivering thermogenesis is activated by fatty acids. There are multiple proposed mechanisms, but details are still unknown.<sup>10</sup> The intermediate states which cannot be observed in steady-state can be discovered by time-resolved kinetics measurement, and it could shed light on its working principle.

In conclusion, our understanding on the proton-related biological processes can be deepened by observing the entire process step by step in real time. Eventually, based on the information obtained from it, molecular movie of the process can be constructed. Better understanding about “Protonics” as well as “Electronics” of biological system can lead us into comprehensive pictures of many proton related processes, and ends up in improvements in our applications such as proton-exchange membrane of fuel cells or photo-acid of photo-nanolithography, which could address some of serious problems for humanity.

### 6.3 References

1. Gutman, M.; Nachliel, E., The Dynamic Aspects of Proton-Transfer Processes. *Biochim. Biophys. Acta* **1990**, *1015* (3), 391-414.
2. Wraight, C. A., Chance and design - Proton transfer in water, channels and bioenergetic proteins. *Biochimica Et Biophysica Acta-Bioenergetics* **2006**, *1757* (8), 886-912.
3. Agmon, N.; Bakker, H. J.; Campen, R. K.; Henschman, R. H.; Pohl, P.; Roke, S.; Thamer, M.; Hassanali, A., Protons and Hydroxide Ions in Aqueous Systems. *Chem. Rev.* **2016**, *116* (13), 7642-72.
4. Shinobu, A.; Palm, G. J.; Schierbeek, A. J.; Agmon, N., Visualizing Proton Antenna in a High-Resolution Green Fluorescent Protein Structure. *J. Am. Chem. Soc.* **2010**, *132* (32), 11093-11102.
5. Unno, M.; Ishikawa-Suto, K.; Kusaka, K.; Tamada, T.; Hagiwara, Y.; Sugishima, M.; Wada, K.; Yamada, T.; Tomoyori, K.; Hosoya, T.; Tanaka, I.; Niimura, N.; Kuroki, R.; Inaka, K.; Ishihara, M.; Fukuyama, K., Insights into the Proton Transfer Mechanism of a Bilin Reductase PcyA Following Neutron Crystallography. *J. Am. Chem. Soc.* **2015**, *137* (16), 5452-5460.
6. Kovalevsky, A. Y.; Hanson, B. L.; Mason, S. A.; Yoshida, T.; Fisher, S. Z.; Mustyakimov, M.; Forsyth, V. T.; Blakeley, M. P.; Keen, D. A.; Langan, P., Identification of the Elusive Hydronium Ion Exchanging Roles with a Proton in an Enzyme at Lower pH Values. *Angew Chem Int Edit* **2011**, *50* (33), 7520-7523.
7. Grimsley, G. R.; Scholtz, J. M.; Pace, C. N., A summary of the measured pK values of the ionizable groups in folded proteins. *Protein Sci.* **2009**, *18* (1), 247-51.

8. Alexov, E.; Mehler, E. L.; Baker, N.; Baptista, A. M.; Huang, Y.; Milletti, F.; Nielsen, J. E.; Farrell, D.; Carstensen, T.; Olsson, M. H.; Shen, J. K.; Warwicker, J.; Williams, S.; Word, J. M., Progress in the prediction of pKa values in proteins. *Proteins* **2011**, *79* (12), 3260-75.
9. Andre, I.; Linse, S.; Mulder, F. A., Residue-specific pKa determination of lysine and arginine side chains by indirect <sup>15</sup>N and <sup>13</sup>C NMR spectroscopy: application to apo calmodulin. *J. Am. Chem. Soc.* **2007**, *129* (51), 15805-13.
10. Crichton, P. G.; Lee, Y.; Kunji, E. R., The molecular features of uncoupling protein 1 support a conventional mitochondrial carrier-like mechanism. *Biochimie* **2017**, *134*, 35-50.